TRANSPORT PROPERTIES OF DNA NANOSTRUCTURES

BY

CHEN-YU LI

DISSERTATION

Submitted in partial fulfillment of the requirements
for the degree of Doctor of Philosophy in Biophysics and Computational Biology
in the Graduate College of the
University of Illinois at Urbana-Champaign, 2017

Urbana, Illinois

Doctoral Committee:

Professor Aleksei Aksimentiev, Chair
Professor Yi Lu
Assistant Professor André Schleife
Assistant Professor Diwakar Shukla

Abstract

Besides the role of genetic information storage, DNA has been proposed as a new material in nanotechnology. The idea came from the nature-occurring Holliday junction (HJ) which allows more than 2 DNA strands to be assembled. Multiple HJs can be combined with desired orientation to form complex 2- or 3-dimensional objects. One of the most popular methods that realize this concept is the DNA origami. The basic principle of DNA origami is the programmed folding of a long (tens of thousands of nucleotides) DNA strand into a custom shape, guided by multiple specially designed short DNA strands which connect different parts of the long DNA strand through HJs. Since its first demonstration in 2006, not only large (up to hundreds of nanometers) and complex 3D objects with sub-nanometer precision have been produced, but some of them were able to perform active functions.

Experimental techniques, including atomic force spectroscopy, small-angle X-ray scattering, transmission electron microscopy (TEM), super-resolution optical imaging, FRET and magnetic tweezers, have been applied to study the global structure and dynamics of the DNA nanostructures. Recently, an atomic-level model of DNA origami *in situ* has also been obtained, which showed considerable deviation from the idealized structure. A few experimental studies reported the ionic permeability of DNA origami constructs placed on top of a solid-state support or embedded in a lipid bilayer membrane. However, the transport properties of DNA nanostructures and the underlying mechanism have remained relatively unexplored.

Here, several simulation studies focusing on the transport properties of DNA nanostructures are presented. Specifically, a comprehensive study on the ionic conductivity and mechanical properties of DNA plates of different lattice type, the number of layers, nucleotide content and cross-over pattern in the electric field were performed. The ionic conductances of a range of DNA channels embedded in lipid membrane were obtained. Several factors were found to affect the ionic conductances of DNA channels, including channel aggregation, channel unfolding and blocking by lipid molecules. The smallest and the largest DNA channels so far were developed. The first DNA scramblase which facilitates the translocation of lipid molecules across the membrane was developed. These works represent potential applications of DNA nanostructures in biosensing, nanofluidics, drug delivery and biomedical engineering.

Acknowledgments

This project would not have been possible without the support of many people. Many thanks to my adviser, Aleksei Aksimentiev, who has guided me through the years. Thanks to my committee members, Prof. Yi Lu, Prof. André Schleife and Prof Diwakar Shukla for their guidance and support. Thanks for the guidance and help of all other members in Aksimentiev's group, especially Jejoong Yoo and Christopher Maffeo. Thanks to my collaborators in the group of Prof. Ulrich F. Keyser, especially Elisa Hemmig, Jinglin Kong, Kerstin Göpfrich and Alexander Ohmann.

To my girlfriend Meng-Fan, thank you for your love, patience, understanding and encouragement. And finally, to my family and friends, thank you all for your kindness, love and support.

This work was supported by the National Science Foundation (DMR-1507985, PHY-1430124, and EEC-1227034), and the TeraGrid (MCA05S028).

Table of Contents

Chapter 1

Background

1.1 The molecular structure of DNA

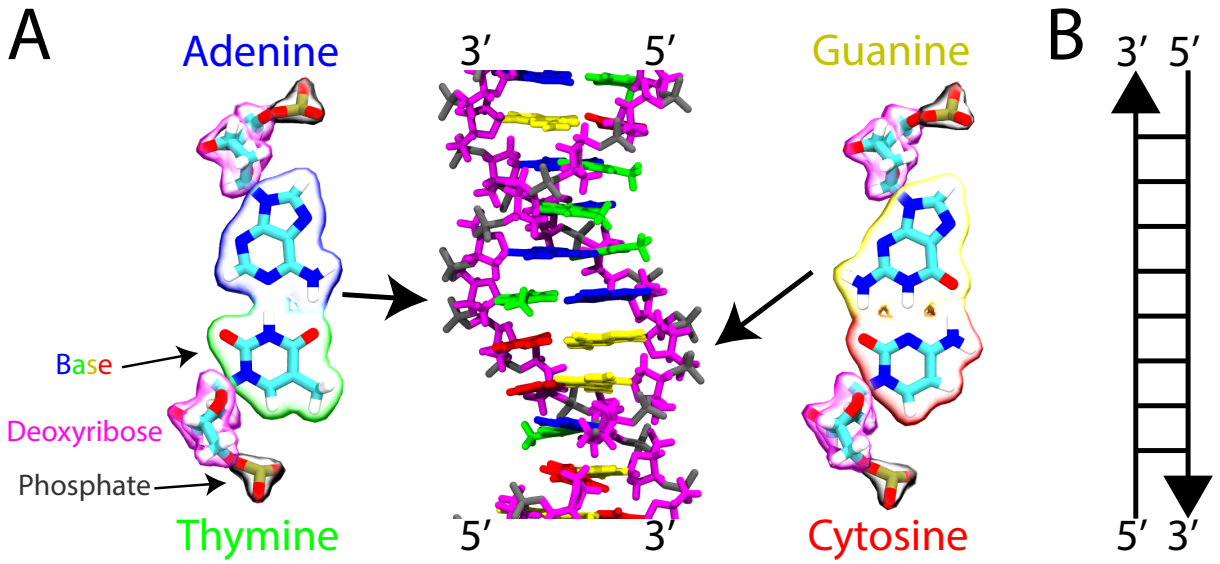

Figure 1.1: The molecular structure of DNA. (A) The structures of the Adenine (A)–Thymine (T) (left) and Guanine (G)–Cytosine (C) (right) base-pair and the DNA double helix (center). In the ball-and-stick representation of the base-pairs, each atom is colored differently (C: cyan; O: red; N: blue; H: white; P: ochre). The molecular surfaces of the base-pairs highlight different components of each nucleotide; the bases of A, T, G and C are colored by blue, green, yellow and red, and the deoxyribose and phosphate of each nucleotide are colored in magenta and gray. The DNA double helix (center) was colored using the same scheme as the molecular surface. The 5' and 3' indicate the corresponding 5' and 3' ends. (B) A reduced representation of the DNA double helix shown in panel (A).

As the macromolecule that stores the genetic information, DNA's structure is a long polymer. Each monomer is a nucleotide. There are three major components in a nucleotide, including the base, deoxyribose and the phosphate, Fig. 1.1A. Based on different bases the nucleotide has, there are 4 types of nucleotides in nature, adenine (A), thymine (T), cytosine (C) and guanine (G). A DNA strand (single-stranded DNA, or ssDNA) is a polymer chain of different nucleotides. The order of the nucleotides is called the DNA sequence. The DNA strand has a polarity (asymmetry), which is defined by the orientation of the 5' and 3' carbon

of the deoxyribose on the nucleotide. Thus, a DNA strand has a unique defined DNA sequence, which is read from the 5' end to the 3' end. Most of the organisms in nature use double-stranded DNA (dsDNA) to store the genetic information. In a dsDNA, two DNA strands are held together by non-covalent interactions including the hydrogen bonds. To form the hydrogen bonds, nucleotides on one strand have to correctly pair with nucleotides on the other strand to form base-pairs following the rule: A pairs with T and G pairs with C. Due to the 3-dimensional structure of the nucleotides, when two DNA strands formed base-pairs with each other, the structure will twist and form the famous double-helix structure of dsDNA. In many molecular biology textbooks or the design of the DNA nanostructures, to reduce the complexity of the DNA structure, A dsDNA would be represented as two parallel lines, Fig. 1.1B. The two parallel lines represent the two DNA strands. The short lines connecting the two DNA strands represent the base-pairs. The arrows indicate the polarity of each DNA strand, from 5' to 3'.

In the rest of this chapter, current advancement of self-assembled DNA structures and current computational model of DNA structure will be reviewed.

1.2 Self-assembled DNA structures

To build custom self-assembled structures out of DNA, a four-way DNA junction, known as a Holliday junction (HJ) [1] made of four separate DNA strands, was used as the fundamental structural unit. HJs naturally occur in cells during homology recombination for repair of breaks in double-stranded (ds) DNA or chromosomal crossover in meiosis [2]. The angles between the 4 DNA strands (4 arms) can be tuned as desired, Fig. 1.2A,B [3]. The number of the arms in a DNA junction can also vary from 3 to 12 to create other types of building blocks to make complex 3D DNA objects [3]. By connecting multiple junctions, several complex geometrical objects have been demonstrated before. Some of the early designs reproduced basic geometric forms such as cubes [4], tetrahedrons [5], octahedrons [6], or cylinders [7]. Fig. 1.2C illustrates a DNA cube formed by six 80-nucleotide-long synthetic DNA strands [4]. Each edge of the cube is two turns of dsDNA ($\sim$7 nm); the corners of the cube contain three-way junctions.

1.2.1 DNA origami

Although the principles of structural DNA nanotechnology based on short synthetic oligomers were established in the early 1990s [3,4], the techniques were not widely used because synthetic oligomers were expensive and limited to $<$ 100 nucleotides (nts). Besides, since large objects made of short oligomers were fragile with low yield, most of the self-assembled DNA objects were only tens of nanometer size. In 2006, with the

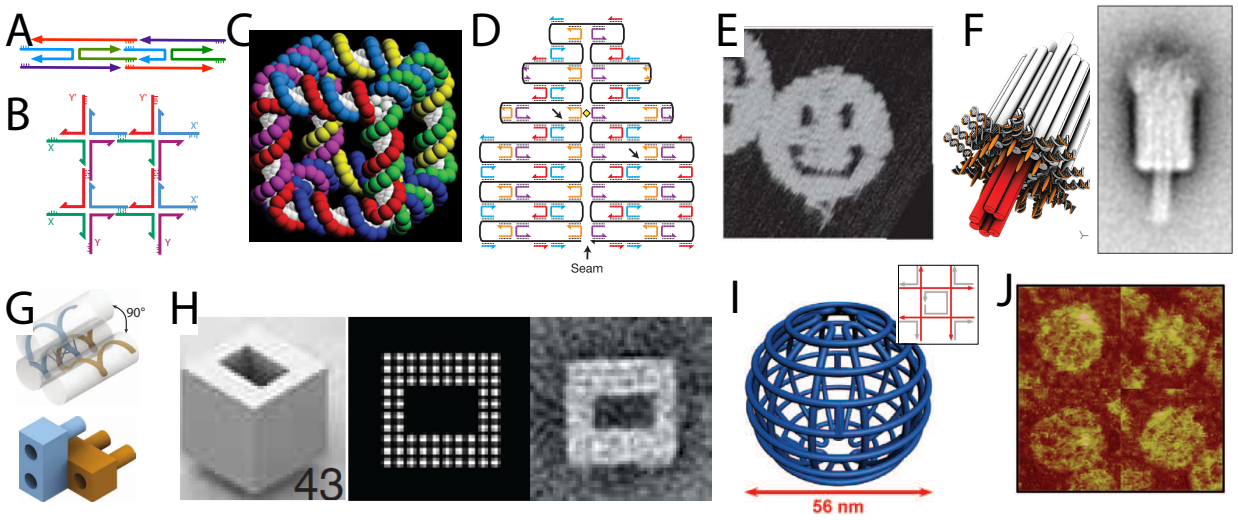

Figure 1.2: Self-assembled DNA systems. (A, B) Schematics of four-way DNA junctions forming a complex DNA structure, using similar representation as in Fig. 1.1B [3]. (C) One of the first self-assembled DNA structures, a DNA cube [4]. Colors indicate different DNA oligomers. (D) Schematic illustrating design principles of 2D DNA origami. A long viral DNA (black) is folded into a 2D object guided by short oligomers (multiple colors). (E) An example of a folded 2D origami object [8]. (F) A design of a membrane-spanning 3D origami channel (left) and the TEM image of the folded object (right) [9]. (G, H) Structures created from DNA bricks [10]. Two connected DNA bricks, shown in the strand model and the LEGO model (G). 3D design, top-view of the design, and the TEM image of a folded DNA brick structure (H). (I, J) Design (I) and AFM image (J) of DNA nanospheres made using 3D gridirons [11]. The inset in (I) illustrates a gridiron unit formed by 4 four-arm junctions. The size of the image in panel (J) is 200 nm $\times$ 200 nm.

advances in molecular biology technique, a new method called DNA origami was developed by Rothemund to overcome those issues [8]. Instead of making the DNA object purely from many short oligomers, the basic principles of DNA origami is the programed folding of a long (1,000+ nts) single-stranded (ss) "scaffold" segment of viral DNA into custom shape, guided by many short ssDNA "staple" Fig. 1.2D. The first DNA origami objects were two-dimensional structures with 100 nm wide that demonstrated the power of the approach, Fig. 1.2E. This approach was soon adopted and generalized to created 3-dimensional objects. Presently, a variety of three-dimensional DNA origami objects can be experimentally assembled with high yield [12], including various polyhedra [5,13], curved objects [14], a hand-like construct [15], a nanorobot [16], and even a DNA version of a transmembrane channel [9], Fig. 1.2F. Computer-aided design software such as caDNAno [17] also facilitated the adoption of the DNA origami method [18, 19]. Ease of use, low cost and high yield have made the origami technique a dominant method for creating self-assembled DNA structures.

1.2.2 DNA bricks

In 2012, another new approach to building self-assembled 3D DNA structures, using so-called DNA bricks or DNA LEGO, was developed by Ke *et al.* [10]. In contrast to DNA origami, DNA bricks do not require a long continuous scaffold strand. The basic design unit—a DNA brick—is a 32-nt ssDNA strand folded 180° in the middle that ultimately hybridizes with neighboring bricks. In the LEGO analogy, the DNA brick corresponds to a two-by-one LEGO brick, Fig. 1.2G. There are four 8-nt binding domains in a DNA brick. The two binding domains adjacent to the fold in the strand are called the "heads" (analogous to the bumps of a LEGO brick), and the remaining two binding domains at the ends of the ssDNA strand are called "tails" (analogous to the holes of a LEGO brick). The nucleotide sequences of the heads and tails of each brick prescribe the order the bricks assemble into a larger structure. Although this method has potentially lower yield and less rigidity comparing to the DNA origami method, DNA brick crystals longer than 500 nm with a depth of 80 nm has been reported [20]. Another advantage of DNA brick is that once a collection of strands is designed to completely fill a rectangular volume, they can be used to form any shape that fits within the volume simply by omitting select strands from the final mixture, Fig. 1.2H. In contrast, each new DNA origami design requires a custom collection of staple strands. The ability to reuse previous design and the ease of shape customization makes the DNA bricks approach attractive for future developments in practical DNA nanotechnology.

1.2.3 Gridirons

The relaxed structure of a four-way HJ is characterized by a right-handed twist with a 60° angle. The HJs in a typical DNA origami design are constrained by neighboring junctions to a $\sim 0°$ angle, restricting the scaffold to lie along a discrete set of parallel lines, Fig. 1.2A. Han *et al*. proposed a different arrangement of HJs that can create a new type of 3D DNA structure known as the gridiron [11], Fig. 1.2I and J. The inset of Fig. 1.2I illustrates how the basic unit of a gridiron is designed from 4 HJs so that each HJ is constrained by the others to have a $\sim 90°$ angle, forming the planar gridiron structure. 3D structures can be assembled from 2D gridiron units by either stacking the units into multiple layers, intertwining units of orthogonal orientations, or adjusting the distance between the four-arm junctions to introduce curvature. A range of spectacular structures has been assembled with high yields using the gridiron approach [11], such as the large hollow spheres that are illustrated in Fig. 1.2I and J. Such structures are impossible to manufacture using conventional DNA origami designs based on 0° HJs.

1.3 Theoretical and computational models of DNA origami

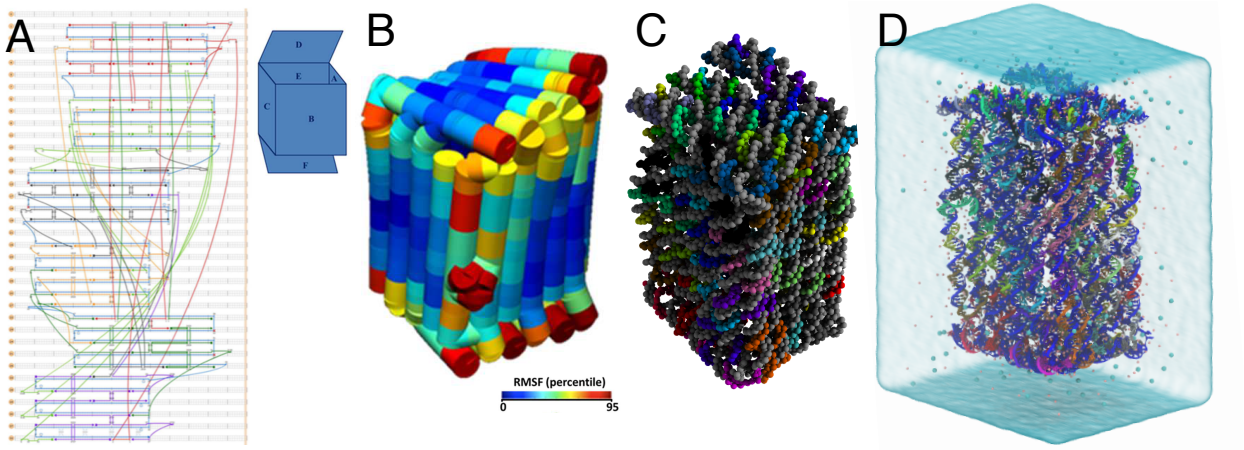

Figure 1.3: Computer models of DNA origami. (A) CaDNAno design of a DNA origami box developed by Zadegan et al [21]. The scaffold (blue) and staple strands (other colors) are drawn as lines. The inset schematically shows the assembled box. (B) Continuum mechanics model (CanDo [22]) of the DNA box [21]. The color scale indicates the predicted root-mean-square fluctuations of the eigenmodes. (C) Coarse-grained model of the DNA origami box. In this particular model, each nucleotide is represented by two beads [23]. (D) All-atom model of the DNA origami box. Mg^{2+} and Cl^{-} ions are shown as pink and cyan spheres, respectively; a blue semi-transparent surface depicts the water box.

To design a 3D DNA origami structure, the most popular computer software is caDNAno [17], which is both available as a plug-in for the Autodesk Maya software and a standalone program. A user first selects the lattice type to use, which is either a square- or a honeycomb-lattice. Then, the user can specify a path which the scaffold will traverse. Next, the user can let the software automatically generate the corresponding staples which will help the scaffold to fold into the desired shape, or design custom staples. Finally, the nucleotide sequence can be chosen from the library of commonly used sequences or imported by the user. Fig. 1.3A shows an example of a DNA origami design created using caDNAno [21]. Other software for designing DNA nanostructures include NanoEngineer-1, vHelix and Tiamat. The NanoEngineer-1 has a 3D workspace, allows users to create DNA nanostructures that feature non-parallel DNA helices, and does not have the strict definition of "scaffold" or "staple". Those features made NanoEngineer-1 a better tool for creating nanostructures with DNA bricks and gridirons. I built an on-line server for users to convert the NanoEngineer-1 design to all-atom structure (http://bionano.physics.illinois.edu/nanoengineer2pdb). The vHelix features automated DNA nanostructure design from polyhedral meshes [24]. The Tiamat program [25] enables semi-automatic generation of the strand sequences. Those programs greatly simplify the design of a DNA origami object, yet they do not provide direct information about the object's physical properties.

1.3.1 Continuum description

Continuum models, which are widely used in all branches of engineering, have been applied to describe the mechanical and structural properties of DNA origami objects [22, 26]. An online tool called **C**omputer-**a**ided e**n**gineering for **D**NA **o**rigami (CanDo; http://cando-dna-origami.org) can take a caDNAno design and predict its relaxed structure and the degree of local structural fluctuations. Fig. 1.3B shows an example of the CanDo prediction for a DNA origami box. In CanDo, each dsDNA segment is represented by a homogeneous, isotropic elastic cylinder that can be bent, twisted and stretched [27]. Single-stranded DNA segments are described using a modified version of a freely jointed chain model [28]. An HJ is modeled as a rigid connection between points along neighboring cylinders. Finally, nicks are represented by locally reducing the elastic bending and torsional stiffness parameters while retaining the stretch stiffness of the double-helix. Given the length, diameter, stretch modulus, bending modulus and twist modulus of the elastic cylinder, the energy-minimized conformation of the structure is obtained by iteratively solving equations using a non-linear finite element approximation with single-base pair resolution [22, 29, 30]. Because of its computational efficiency, ease of use, and straightforward quantitative predictions, the CanDo program is being widely used to optimize the design of DNA origami structures prior to experimentally attempting their assembly. Although the parameters describing dsDNA in the CanDo model can be customized, the CanDo model does not explicitly account for the effect of DNA sequence, inter-helical electrostatic repulsion, the presence of major and minor grooves or solvent conditions.

1.3.2 Coarse-grained simulations

With moderate computational cost and resolution between all-atom and continuum models, coarse-grained (CG) approaches rely on a less detailed description of a system than all-atom MD to allow longer simulations of larger systems [31–33]. Most CG models of dsDNA [34–44] typically describe each nucleotide using two-to-six interaction sites or beads, each of which represents a group of several atoms. The solvent is usually incorporated implicitly through non-bonded interaction potentials between the beads. Fig. 1.3C illustrates a CG model of a DNA origami box. Due to the reduced number of degrees of freedom, the CG simulation also allows a larger integration time step, which significantly increases the timescale of the MD simulation. The CG MD simulations of larger 2D origami structures have been reported using the oxDNA model [45], revealing "woven" patterns (where the double-stranded segments were spread between Holliday junctions) similar to those observed experimentally [8]. The large-amplitude, global fluctuations in the CG MD suggesting that their structure in solution deviates considerably from their idealized design. Unfortunately, most CG models are still unable to capture some essential features of the DNA systems. Very few CG models distinguish

between major and minor grooves of dsDNA or provide a realistic description of solvent conditions. The latter is essential for computational characterization of transport properties, which is the main objective of this project.

1.3.3 All-atom method

All-atom (AA) MD simulations allow the microscopic dynamics of a molecular system to be described with atomic resolution. Fig. 1.3D illustrates an all-atom model of a DNA origami box. In the AA MD method, each atom in the system is explicitly present and interacts with each other according to the molecular force field [46], which was first obtained from the quantum mechanical calculation and calibrated to quantitatively reproduce the experimental measured physical properties of a simulated system. The trajectory of each atom i is obtained by integrating Newton's equation $\vec{a}_i(t) = -\nabla U(\vec{r}_1(t), \ldots, \vec{r}_N(t))/m_i$ using the Verlet algorithm [47], where $\vec{a}_i(t)$, $\vec{r}_i(t)$, m_i and $U(\vec{r}(t))$ are the acceleration, coordinates, mass of atom i and the potential energy (molecular force field), respectively, and N is the total number of atoms in the system.

Due to the large size of the self-assembled DNA object (usually $>$ 10 nm in each direction) and the inaccurate parameterization of charge-charge interaction which is dominant in DNA object simulation, AA MD method was not a good choice before. However, with the recent advancement of the massively parallel supercomputer, GPU-accelerated MD package, and improved charge-charge interaction [48–51], AA MD simulation of DNA nanostructures is now feasible [52]. The main advantage of the all-atom MD method is its intrinsic sensitivity to molecular details, natural incorporation of DNA sequence effects and sequence-dependent conformations, which we will see examples in Chapter 3. Also, since solvent molecules are modeled explicitly, AA MD simulation is capable of reproducing the experimental behavior [53] and allows one-to-one comparison between theory and experiment (Chapter 3 and 4) [54]. The main disadvantage of the method is its timescale within the limited computational resources, which is currently limited to several microseconds.

Chapter 2

General methodology

2.1 All-atom molecular dynamics simulation

All molecular dynamics simulations were performed using the program NAMD2 [56], periodic boundary conditions, the CHARMM36 parameter set for water, ions and nucleic acids [57], CHARMM parameters for the DPhPC lipid bilayer [58], CHARMM General Force Field parameters for the cholesterol and porphyrin [59], CHARMM-compatible parameters for amorphous silicon dioxide [60], and custom parameterization of ion-DNA ion-ion, ion-lipid, and DNA-lipid interactions [48–51]. All simulations employed a 2–2–6-fs multiple timestepping, SETTLE algorithm to keep water molecules rigid [61], RATTLE algorithm to keep all other covalent bonds involving hydrogen atoms rigid [62], a 8–10–12 Å cutoff for van der Waals and short-range electrostatic forces. Long-range electrostatic interactions were computed using the particle mesh Ewald (PME) method [63] over a 1.2 Å resolution grid [64].

2.1.1 Assembly of the simulation systems

The DNA nanostructures were either designed with caDNAno [17] or NanoEngineer-1. The caDNAno designs were converted to idealized all-atom structures using a previously described method [52]. The NanoEngineer-1 designs were converted to all-atom structures by a python script written by me [65]. For DNA channel systems, porphyrins or cholesterols would be covalently added to the channel structure after conversion (Chapter 4). Next, some of the DNA nanostructures (Chapter 4 and 5) would be relaxed in vacuum using the ENRG MD method [66] before combining with other components. Then, some of the DNA nanostructures would be combined with SiO_2 (Chapter 3) or pre-equilibrated lipid patch (Chapter 4 and 5). Mg^{2+}-hexahydrates [48] were randomly placed near the channels in the desired amount. Following

that, water and 1 M KCl were added using the Solvate and Autoionize plugins of VMD.

2.1.2 Equilibration of the all-atom models

Although the equilibration protocols varied chapter by chapter, they followed similar principles. The first step was usually the equilibration of water, ions and lipid membrane. In this step, all non-hydrogen atoms of the DNA nanostructure were harmonically restrained (with the spring constant $k_{\text{spring}} = 1$ kcal/(mol Å^2)) to its initial coordinates, allowing the water, ions and lipid to equilibrate. Equilibration of water and ions usually completed in a couple nanoseconds. But, the lipid molecules were larger and diffused slower. Equilibrating the toroidal pore would take ∼50 ns (Chapter 4 and 5). The second step would be the stepwise equilibration of the DNA nanostructures. In this step, the spatial restraints on the DNA atoms were replaced by a network of harmonic restraints that maintained distances between atomic pairs at their initial values; such elastic restraints excluded hydrogen atoms, phosphate groups, atoms in the same nucleotide and pairs separated by more than 8 Å. The spring constant would be decreased step-by-step to gradually relax the structure. In the final step, the entire system will be simulated without any restraints to fully equilibrate the system.

2.1.3 MD simulation of ionic current

All simulations of the ionic current were performed in the constant number of atoms, volume and temperature ensemble. A voltage drop (V) across the system was produced by applying an external electric field E such that $V = -EL$, where L was the length of the simulation system in the direction of the applied field [54].

In Chapter 3, to determine the dimensions of the system for the constant volume simulations, we first obtained the average X-Y cross section area of the system of interest using the last 400 ns of the NPT equilibration. Among the total number of frames of the equilibration trajectory, we chose the one having its X-Y cross section area closest to the 400 ns average and started our ionic current simulation using the coordinates of that frame. To prevent the DNA origami from drifting in the electric field, we applied a harmonic constraint to its center of mass using the spring constant of 1 kcal/(mol Å^2). As the X-Y cross section area of the SQ2/SiO_2 hybrid system was fixed during the equilibration, the ionic current simulations were performed starting from the last frame of the NPT equilibration; no restraints were applied to the DNA origami plate.

In Chapter 4, the X-Y cross section area was found to be less fluctuating at the presence of the lipid membrane. So, the ionic current simulation was started from the last frame of the NPT equilibration.

2.2 Ionic current calculations

Prior to calculations of the ionic current, frames of the MD trajectory were aligned to have the center of mass of the DNA nanostructure stationary. Doing so eliminated the noise associated with the system's drift. The instantaneous current was computed as

$$I(t+\frac{\Delta t}{2}) = \frac{1}{\Delta t L_{\mathrm{Z}}} \sum_{i}^{N} q_i \Delta Z_i \tag{2.1}$$

where the sum over i indicates a sum over all ions, Δt is the time interval between the two consecutive frames of the trajectory, L_{Z} is the length of the system along the Z axis, q_i is the charge of ion i and $\Delta Z_i = Z_i(t+\Delta t) - Z_i(t)$ is the displacement of ion i along the Z direction between the two frames [67]. To properly account for the wrapping of the MD trajectory according to the periodic boundary conditions,

$$\Delta Z_i = \begin{cases} Z_i(t+\Delta t) - Z_i(t) - L_{\mathrm{Z}}, & Z_i(t+\Delta t) - Z_i(t) > L_{\mathrm{Z}}/2 \\ Z_i(t+\Delta t) - Z_i(t) + L_{\mathrm{Z}}, & Z_i(t+\Delta t) - Z_i(t) < -L_{\mathrm{Z}}/2. \end{cases} \tag{2.2}$$

The average current of a trajectory was computed by summing up all instantaneous currents and dividing by the number of coordinate frames of the trajectory. Typically, the frames were collected every 2.4 ps. To estimate the error, the ionic current trace was first block averaged with the indicated block size. The reported standard errors of the mean were calculated from the block-averaged current traces.

2.3 Calculations of the local density and flux

We divided the simulation system into 5 Å × 5 Å × 5 Å grids and calculated the average density of the selected atom groups in each grid using a sampling frequency of 240 ps. The local three-dimensional (3D) flux of ions and water was computed by extending the method described in the previous section to 3D. The change in the coordinates of particle i between consecutive frames is

$$\Delta\vec{r}_i(t+\Delta t/2) = (\Delta X_i(t+\Delta t/2), \Delta Y_i(t+\Delta t/2), \Delta Z_i(t+\Delta t/2)), \tag{2.3}$$

where $\Delta X_i(t+\Delta t/2)$ and $\Delta Y_i(t+\Delta t/2)$ are computed similarly to $\Delta Z_i(t+\Delta t/2)$, Equation 2.2. To compute local fluxes, we used a regular orthogonal $N_{\mathrm{X}} \times N_{\mathrm{Y}} \times N_{\mathrm{Z}}$ grid dividing the simulation box into $N_{\mathrm{X}} \times N_{\mathrm{Y}} \times N_{\mathrm{Z}}$ rectangular blocks of identical dimensions $l_{\mathrm{X}} = L_{\mathrm{X}}/N_{\mathrm{X}}$, $l_{\mathrm{Y}} = L_{\mathrm{Y}}/N_{\mathrm{Y}}$ and $l_{\mathrm{Z}} = L_{\mathrm{Z}}/N_{\mathrm{Z}}$. A set of indices (l, m, n) indicates the position of each block in X, Y, and Z directions. To compute the contribution of the

displacement vector of particle i, $\Delta\vec{r}_i(t+\Delta t/2)$, to the local flux through each block, we assumed that the particle migrates from $\vec{r}_i(t)$ to $\vec{r}_i(t+\Delta t)$ along a straight line. Then, we determined the fraction of the displacement vector in each of the $N_{\mathrm{X}}N_{\mathrm{Y}}N_{\mathrm{Z}}$ blocks, $f_{i,(l,m,n)}(t+\Delta t/2)$ such that $\sum_l \sum_m \sum_n f_{i,(l,m,n)}(t+\Delta t/2) = 1$. Finally, we defined the components of the instantaneous local flux per unit area of a chosen species in block (l,m,n) as

$$\begin{aligned}
J_{\mathrm{X},(l,m,n)}(t+\Delta t/2) &= \tfrac{1}{\Delta t l_{\mathrm{X}} l_{\mathrm{Y}} l_{\mathrm{Z}}} \textstyle\sum_i^M \Delta X_i(t+\Delta t/2) f_{i,(l,m,n)}(t+\Delta t/2) \\
J_{\mathrm{Y},(l,m,n)}(t+\Delta t/2) &= \tfrac{1}{\Delta t l_{\mathrm{X}} l_{\mathrm{Y}} l_{\mathrm{Z}}} \textstyle\sum_i^M \Delta Y_i(t+\Delta t/2) f_{i,(l,m,n)}(t+\Delta t/2) \\
J_{\mathrm{Z},(l,m,n)}(t+\Delta t/2) &= \tfrac{1}{\Delta t l_{\mathrm{X}} l_{\mathrm{Y}} l_{\mathrm{Z}}} \textstyle\sum_i^M \Delta Z_i(t+\Delta t/2) f_{i,(l,m,n)}(t+\Delta t/2)
\end{aligned} \tag{2.4}$$

where M is the total number of particles of a given species. The mean local flux vector field was computed by averaging Equation 2.4 over the production MD trajectories.

To visualize the mean 3D flux field using a 2D plot, we averaged the 3D vector field over the given axes. The resulting 2D vector field was converted to streamline plots using the streamplot function of the matplotlib library [68].

Chapter 3

Ionic conductivity and mechanical properties of self-assembled DNA plates

3.1 Introduction

Nanopores have emerged as versatile tools for single-molecule manipulation and analysis [69–72]. In a typical measurement, a charged biomolecule—DNA or a protein—is transported through a narrow pore in an insulating membrane by external electric field. The presence and, in some cases, the chemical structure of a biomolecule can be detected by measuring the change in the ionic current that flows through the nanopore [73–81].

An accurate and reproducible process of nanopore fabrication is a necessary prerequisite for practical applications of the nanopore method. Differentiation between similar biomolecules may also require incorporation of specific ligands within the nanopores [82, 83]. While more straightforward in the case of biological nanopores [84], the attachment of specific binding sites with control over their position by chemical modification of nanopores in solid-state membranes continues to present considerable challenges [85, 86].

Combining biological materials with inorganic nanopores can give the resulting hybrid structure a more predictable shape and offer a route to biofunctionalization [83, 87–90]. One such material is DNA origami—an object obtained by folding a long strand of DNA into a predefined pattern [8]. Since the DNA origami technique was first demonstrated in 2006, it has been used to assemble a variety of complex three-dimensional objects [3, 17–19, 91, 92]. A number of auxiliary components, such as fluorescent labels, nanoparticles or enzymes, can be incorporated into the origami objects with base-pair accuracy [93–102]. The nanometer precision of the DNA self-assembly process and compatibility with typical conditions of nanopore experiments make DNA origami an attractive candidate for the construction of hybrid nanopores [103–105].

Hybrid nanopore systems based on DNA origami have already been characterized experimentally [9,106–113]. A cone-like DNA origami funnel was inserted into a silicon nitride nanopore and used for the detection of λ-DNA [106]. Plate-like DNA origami objects were placed on top of nanopores in solid-state membranes and used for the detection of proteins and double-stranded DNA (dsDNA) [107]. Adding single-stranded DNA (ssDNA) overhangs to the DNA origami structure was shown to facilitate the detection of ssDNA translocation [9, 107, 108]. DNA origami plates were also combined with glass nanocapillaries and used for single-molecule detection [108, 112]. In general, the conductance of the hybrid pores was found to depend on the structure of the DNA origami component [113], the ionic concentration of the solution [113] and the magnitude of the electric field [112,113]. The latter effect was presumably caused by the deformation of the DNA origami structure. DNA origami has also been combined with lipid bilayer membranes [9, 109, 110]. Functionalized with cholesterol, a DNA origami channel was inserted into a lipid bilayer and used to detect and distinguish ssDNA [9]. Simpler designs employed partial neutralization of the DNA backbone [109] or attachment of two porphyrin moieties [110].

In this chapter, I present my all-atom molecular dynamics (MD) simulations to characterize the ionic conductivity and deformability of DNA plates, in collaboration with Keyser group from University of Cambridge. Complementing previous experimental work, we investigate the effects of the DNA origami structure, electrolyte conditions and the strength and direction of the electric field. My simulations provide a complete atomic-level account of the ion transport process, detailing previously unknown effects of the DNA origami sequence, magnesium ion concentration and the electro-osmotic flow. Experiments based on electric current recordings and Förster resonance energy transfer (FRET) confirm the predictions of the MD simulations. We demonstrate the feasibility of controlling the electrical conductivity of a DNA self-assembled object by its nucleotide sequence, an ability that may find applications in nanofluidic electronics.

3.2 MD simulations of ionic conductivity of a DNA origami plate

Fig. 3.1A schematically illustrates a system for the experimental characterization of the ionic conductivity of DNA origami plates [112]. This particular image features a two-layer square-lattice DNA origami that measures approximately 57.8 nm (170 bp) $\times$ 52.8 nm (24 helices) $\times$ 4.4 nm (2 helices). Although it is technically possible to simulate this entire DNA origami object using a fully atomistic model, such simulations are computationally expensive and are not even necessary because the full-length plate is a repetition of a unit cell pattern.

Thus, the majority of my MD simulations were performed on all-atom models of the unit cell, such as

the one shown in Fig. 3.1B. The initial coordinates of the models were obtained by converting the caDNAno designs [114] to the atomistic representation following a previously described protocol [52]. By introducing covalent bonds across the periodic boundaries, the DNA origami plates were made effectively infinite in the X-Y plane. The plates were immersed in ionic solution, minimized and equilibrated as described in Section 3.9.

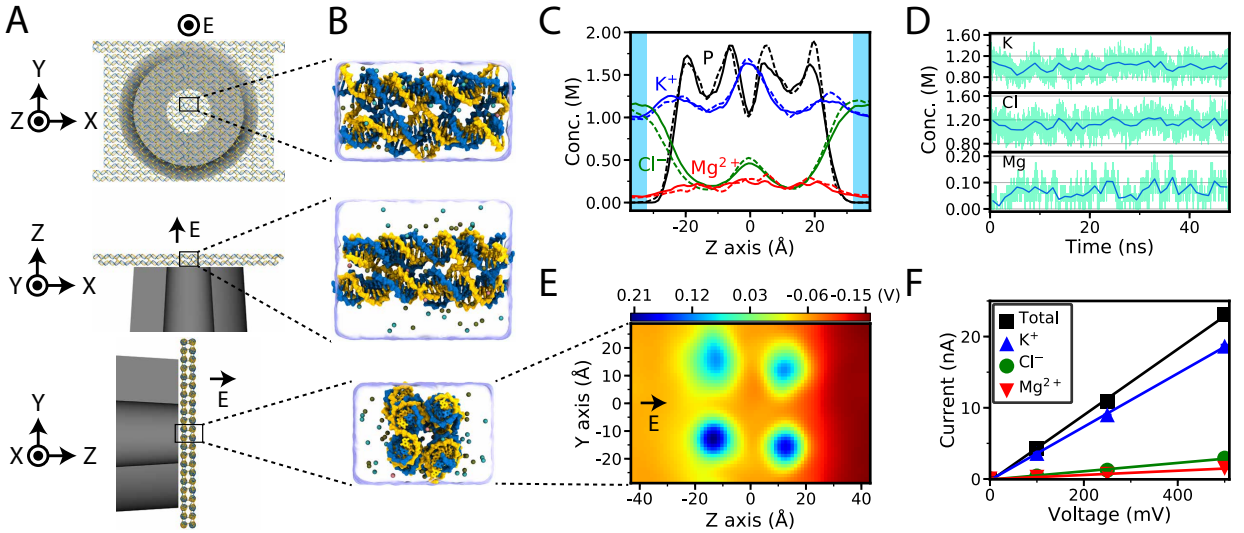

Figure 3.1: MD simulations of DNA origami conductivity. (A) Schematic of experimental setup. A DNA origami plate (yellow and blue) is placed on top of a nanocapillary (gray). (B) All-atom model of the experimental system. The scaffold and staple strands are shown in blue and yellow, respectively. Water is shown as a semitransparent molecular surface, Mg^{2+}, K^+ and Cl^- ions are shown as pink, ochre and cyan spheres, respectively. For clarity, only 10% of the ions are explicitly shown. Under periodic boundary conditions, the DNA origami plate is effectively infinite in the X-Y plane. (B) Distribution of ions across a DNA origami plate as a function of the distance from the plate's center. The distributions obtained from a 48 ns unrestrained equilibration simulation (solid lines) and a 48 ns simulation under a 100 mV applied potential (dashed lines) are plotted. Black lines indicate the distribution of DNA phosphorous atoms. The concentration profiles were computed by averaging over the X-Y plane and the simulation trajectories using 1 Å bins. Blue areas indicate the parts of the system where the bulk ion concentration was computed. (D) Bulk concentration of K^+, Cl^- and Mg^{2+} ions versus simulation time under a 100 mV applied potential. (E) Simulated distribution of the electrostatic potential at a 100 mV applied potential. The map was obtained by averaging the instantaneous distributions of the electrostatic potential over the 48 ns MD trajectory and the X-axis. (F) Ionic current versus applied potential. Each data point was obtained from a 48 ns trajectory. All data presented in this figure are for a two-layer square-lattice DNA origami plate at 50 mM Mg^{2+}/1 M KCl bulk ion concentration.

Fig. 3.1C illustrates a typical distribution of ions in a fully equilibrated system. At the scale of the simulation system, the distribution is non-uniform. Within the volume occupied by DNA origami, the concentration of cations is enhanced and the concentration of anions is reduced, in accordance with the results of previous studies [48, 49]. In a distance of approximately 20 Å from the DNA origami plate, ion concentration profiles flatten out. A rectangular volume away from the DNA (blue area in Fig. 3.1C)

was used to determine the "bulk" concentrations of ions. As the equilibrium distribution of ions is highly nonlinear, it was not possible to determine *a priori* the number of K^+, Cl^- and Mg^{2+} ions that were needed to produce the desired bulk concentration. Hence, several iterative equilibration runs (∼50 ns each) were required to bring the bulk ion concentration to the target value.

To produce ionic current, a uniform electric field, E, was applied normal to the DNA origami plate, inducing an electric potential difference, $V = -EL$, where L was the length of the simulation system in the direction of the applied field [54]. The application of the electric field had a minor effect on the distribution of ions within the DNA origami plate, Fig. 3.1C. The bulk ion concentration remained stationary, Fig. 3.1D.

Fig. 3.1E shows a typical distribution of the electrostatic potential in the simulation system corresponding to a 100 mV voltage difference across the DNA origami plate. The distribution is highly nonlinear within the plate. The approximate location of the DNA helices can be discerned as regions of elevated electrostatic potential, which is produced by the partial positive charge on the DNA bases; the negative charge of the DNA backbone is effectively screened by the counterions. The current of ions produced by the electric field can be readily determined by summing up ion displacements over the simulation system and the MD trajectory [54]. The ionic current appears to increase linearly with voltage and be carried predominantly (80∼85%) by potassium ions, Fig. 3.1F.

3.3 Effect of number of layers, lattice type, and nucleotide composition

To examine how the ionic conductivity of a DNA origami plate depends on the number of DNA layers, square-lattice DNA origami systems containing two (SQ2), four (SQ4), and six (SQ6) DNA layers were built and equilibrated, Fig. 3.2A; the bulk concentrations of Mg^{2+} and KCl were ∼250 mM and 1 M, respectively. The equilibrated structures were simulated under applied bias of 100, 250 and 500 mV for 48 ns each. At the same bias, systems having a larger number of layers showed a lower ionic current, Fig. 3.2B. The dependence of the current on the number of layers is, however, nonlinear: the SQ2 system appears to be more permeable to ions than the SQ4 system at doubled applied bias.

Knowing the dimensions of the simulation system (L_X, L_Y and L_Z) and the extension of the DNA origami along the direction of the applied field L_o, the conductivity of the DNA origami plate $\sigma_{o,Z}$ can be computed from a simple circuit model as

$$\sigma_{o,Z} = \frac{< L_o >< I_Z >}{V L_X L_Y - \rho_s < I_Z > (L_Z - < L_o >)}, \tag{3.1}$$

where V is the applied potential, I_Z is the average current normal to the plate and ρ_s is the resistivity of the solution.

Fig. 3.2C shows the conductivity of the SQ2, SQ4 and SQ6 plates as a function of applied potential. The conductivity of the four- and six-layer structures is approximately the same and does not depend on the applied bias. The conductivity of the SQ2 is higher and increases with the applied potential. Given that the solution resistivity (0.06 Ω m) and the cross-sectional area of the SQ2, SQ4 and SQ6 systems are approximately the same, the apparent difference in the conductivity is caused by the differential extension of the DNA origami along the direction of the applied field. Indeed, the thickness per layer of the SQ2 plate is ∼12% larger than that of the SQ4 and SQ6 systems and increases with the applied potential. The fraction of the plate's volume occupied by DNA is lower in the two layers of the SQ2 plate than in any two layers of the SQ4 or SQ6 structures, and hence the SQ2 structure has a higher conductivity. The more compact structure of the four- and six-layer plates is a consequence of their design. The unit cell of the two-layer plate contains only two Holliday junctions between the two layers, which is considerably less dense than six and ten inter-layer junctions in the four- and six-layer plates, respectively. Furthermore, staple strands in the SQ4 and SQ6 plates can bridge up to three consecutive layers.

In order to determine how the lattice type can affect ion permeation through DNA origami plates, two additional systems based on the honeycomb (HC2) [17] and hexagonal (HX2*) [19] lattices were constructed, Fig. 3.2D. Here, an asterisk was used to distinguish the simulated hexagonal lattice system from the one realized in experiment [19]. The HX2* system was built by inserting a DNA double helix into the central cavity of a honeycomb lattice. In contrast to the system realized in experiments, the central double helix was not connected to the surrounding DNA helices through Holliday junctions.

To compare the ion permeability of different DNA structures, the ionic current per unit area was plotted in Fig. 3.2E (the unit cells of the SQ2 and HC2 structures have different areas). Overall, the current density of the SQ2 plate was roughly twice as high as for the HC2 and HX2* plates at the same applied bias whereas the current densities of the HC2 and HX2* plates were comparable. Taking into account the dimensions of the plates in the direction of the applied field, the conductivity of the SQ2 plate is estimated to be about 120∼130% of the conductivity of the HC2 plate, Fig. 3.2F. The higher conductivity of the SQ2 plate primarily results from the lower density of the DNA nucleotide per unit area of the plate and a higher nearest-neighbor inter-DNA (NNiD) distance, which was defined as the average inter-helix distance. One would intuitively expect the conductivity of HX2* to be lower than that of HC2, given its more compact structure. However, my data shows that the difference in conductivity between HC2 and HX2* is not significant. As the central helix in our HX2* was not connected to the surrounding helices, the electrostatic repulsion between the

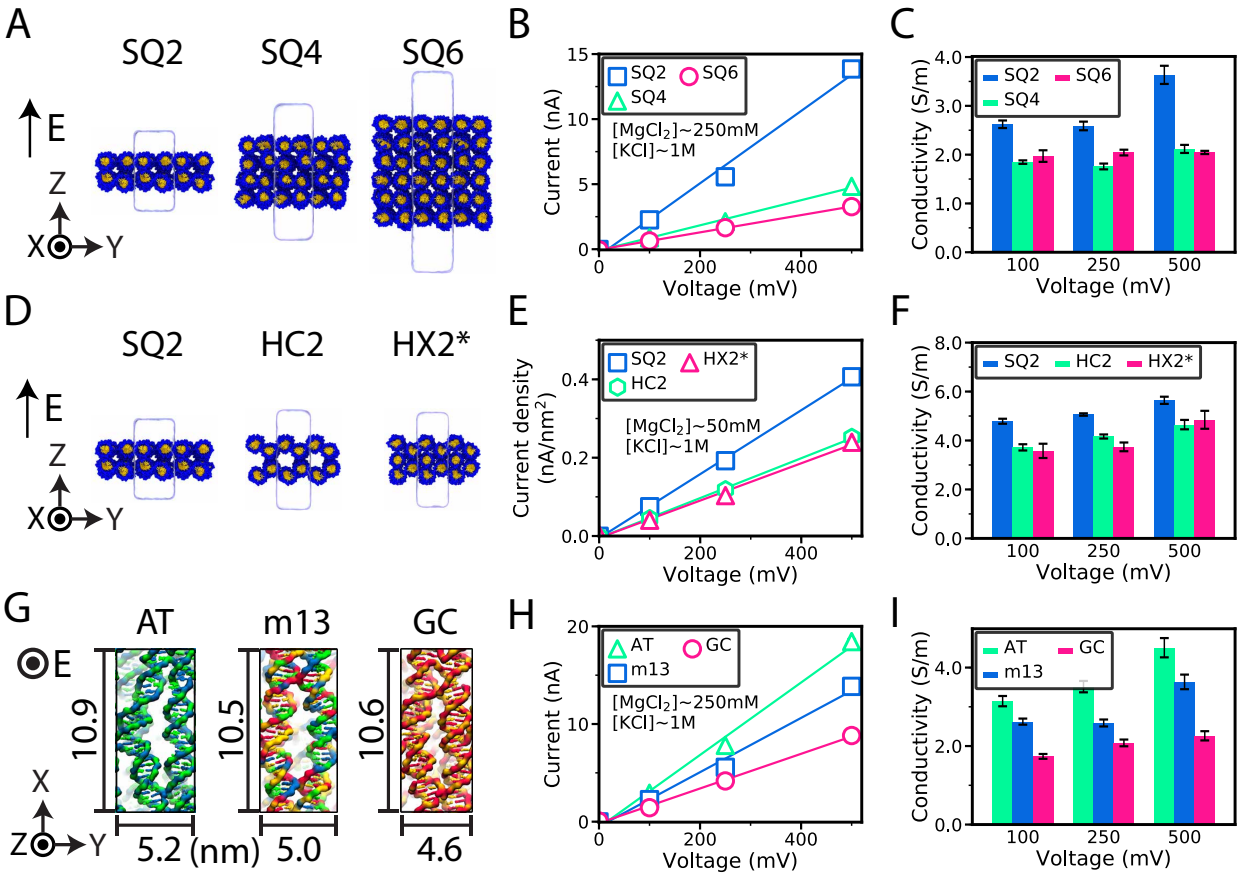

Figure 3.2: Ionic conductivity of DNA origami plates. (A) Simulation systems containing two-, four- or six-layer DNA origami plates. The backbone of DNA is shown in blue, the DNA bases are shown in yellow. The unit cell of each simulated system is shown as a semi-transparent surface. (B) Current–voltage dependence of the two-, four- and six-layer DNA origami plates. Each data point was obtained from a 48 ns trajectory. (C) Electrical conductivity of square-lattice DNA origami versus the number of DNA layers. Data in panels B and C correspond to ∼250 mM Mg^{2+}/1 M KCl bulk ion concentration. (D) Simulation systems containing units cells of the square-lattice, honeycomb and hexagonal DNA origami plates. (E) Ionic current density versus lattice type. (F) Ionic conductivity versus lattice type. Data in panels E and F correspond to ∼50 mM Mg^{2+}/1 M KCl bulk ion concentration. (G) Representative conformations of a square-lattice DNA origami plate containing 100% adenine–thymine (AT), 100% cytosine–guanine (CG) or a 45/55 % AT/CG mixture (m13) of DNA basepairs. The A, T, C and G nucleotides are shown in blue, green, red and yellow, respectively. The average dimensions of the equilibrated structures are indicated in the images. (H, I) Ionic current (panel H) and ionic conductivity (panel I) versus applied voltage for the three systems shown in panel G. The AT and CG systems contained the same number of magnesium ions; the number of Mg^{2+} ions in the m13 system was 2.5% higher than in either AT or CG system. Due to the differential affinity of Mg^{2+} ions to AT and CG basepairs the equilibrium concentrations of Mg^{2+} were 243.6±2.2 (AT), 249.4±2.2 (m13) and 209.4±2.1 (CG) mM. Data in panels B, E and H were obtained from 48 ns trajectories; the lines indicate the linear fits to the data. Error bars in panels C, F, and I show the standard error computed over five ∼10 ns fragments of the 48 ns trajectory.

central helix and the surrounding helix made the entire structure more diffuse in comparison to the HC2 structure. Thus, the NNiD distance is higher for the HX2* structure than for HC2. The larger NNiD distance of the HX2* structure compensates for the higher (than HC2) nucleotide density of HX2*.

MD simulations suggest that the conductivity of a DNA origami plate can also depend on its nucleotide content. Fig. 3.2G shows typical conformations of three SQ2 plates that differ from one another in their design only by their nucleotide content. The nucleotide content appears to affect the average distance between DNA helices within the plate as well as the distance between Holliday junctions along the helices, with the AT plate being most sparse and the CG plate most compact. The simulated ionic current, Fig. 3.2H, and the ionic conductivity, Fig. 3.2I, depend on the nucleotide content, with the AT plate being the leakiest and the CG plate being the most ion-tight. The current and conductivity of the plate made from a fragment of the m13mp18 genome (AT content of 45%) fall in between the data obtained for the AT and CG plates. The sequence dependence can be rationalized taking into account the differential affinity of Mg^{2+} towards AT and CG DNA pairs [49, 115]. The CG-rich DNA origami was found to have a higher concentration of Mg^{2+} inside the origami. The higher concentration of Mg^{2+} reduced the electrostatic repulsion between the DNA helices in the origami, resulting in more compact structures. The higher degree of expansion of the AT system makes it more permeable to ions in comparison to the GC system; the properties of the m13 system fall in between of the AT- and CG-rich systems.

3.4 Magnesium affects the structure and conductivity of DNA origami plates

The results of my MD simulations suggest that the ionic current through the same DNA construct (SQ2) under the same applied voltage drops by ∼43% when the bulk concentration of Mg^{2+} increases from 50 to 250 mM (Fig. 3.1F and Fig. 3.2B). Using an experimental setup shown in Fig. 3.3A, Elisa, a graduate student in Keyser group, systematically examined the dependence of the DNA origami conductivity on Mg^{2+} concentration. The DNA origami plates were repeatedly trapped onto the nanocapillary; the trapping events were discerned by the drop of the ionic current, Fig. 3.3A. The magnitude of the ionic current drop increased as the concentration of Mg^{2+} increased, consistent with the behavior observed in our MD simulations of the origami plates.

Repeating the trapping experiments at four different magnesium concentrations (5.5, 25, 50, and 100 mM $MgCl_2$) while keeping the concentration of KCl at 1 M, the relative change of hybrid nanocapillary-DNA origami conductance was measured. To directly compare the results of the trapping experiments using capillaries of different diameters, our experimental collaborators in the Keyser group define the relative conductance change $\Delta G = 1 - G_{\text{hybrid}}/G_0$, where G_{hybrid}/G_0 is the ratio between the conductance of the bare nanocapillary G_0 and the conductance of the hybrid DNA origami–nanocapillary structure G_{hybrid} upon

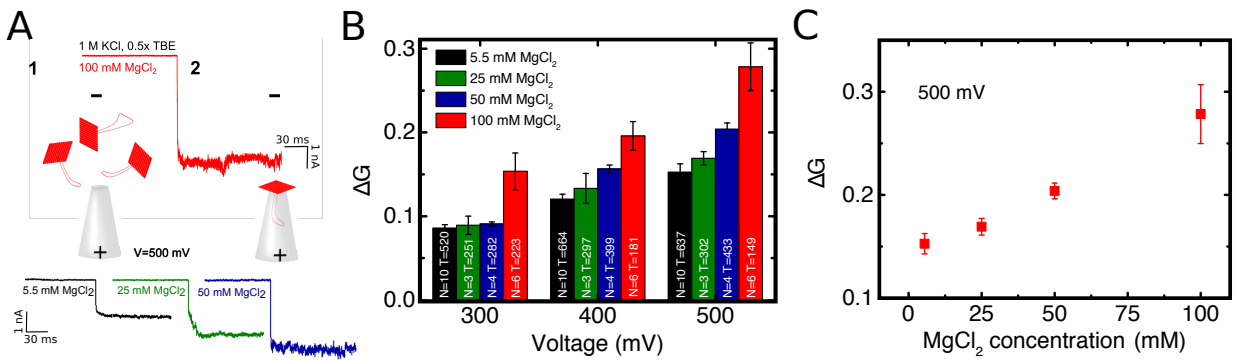

Figure 3.3: Experimental characterization of DNA origami conductivity. (A) Schematic representation of a hybrid DNA origami – quartz nanocapillary structure along with typical ionic current signatures measured at 500 mV and in 1 M KCl, 0.5× TBE (Tris/Borate/EDTA), pH≈8.3. (Top) Baseline current I_0 corresponds to ionic flow through the bare nanocapillary (part 1 of the trace). Once the DNA origami plate is trapped, the reduced ionic current level I_{hybrid} indicates the successful formation of a hybrid structure (part 2 of the trace). (Bottom) Representative examples of hybrid structure formation signatures for $MgCl_2$ concentrations of 5.5 (black), 25 (green) and 50 (blue) mM, all at 500 mV. Larger current reductions were observed at higher $MgCl_2$ concentrations. A representative trace at 100 mM $MgCl_2$ is shown in the top panel. (B) The relative conductance change $\Delta G = 1 - G_{\text{hybrid}}/G_0$ versus $MgCl_2$ concentration and applied potential. G_{hybrid}/G_0 is calculated from the ratio between the ionic current levels I_{hybrid}/I_0 in (2) and (1) as explained in the text. (N) denotes the number of experiments or nanocapillaries used and (T) the total number of repeated trappings to measure the averaged ΔG at 5.5 (black), 25 (green), 50 (blue) and 100 (red) mM $MgCl_2$ for three different applied potentials (300, 400, and 500 mV). (C) ΔG versus $MgCl_2$ concentration at a 500 mV applied potential. Error bars correspond to the standard error of the mean of ΔG.

trapping. The G_{hybrid}/G_0 can be directly inferred from measuring the ratio I_{hybrid}/I_0 between the corresponding ionic current levels I_{hybrid} and I_0, Fig. 3.3A. For each magnesium concentration, our experimental collaborators in the Keyser group tested a range of nanocapillaries (denoted by number of experiments N in Fig. 3.3B) and performed several hundred trappings (denoted by total number of trappings T in Fig. 3.3B) at applied potentials of 300, 400, and 500 mV, respectively.

From the measurements, they can conclude that there is both a voltage and $MgCl_2$ dependence of ΔG. At each $MgCl_2$ concentration, a higher voltage leads to a higher ΔG, Fig. 3.3B; the voltage dependence is more pronounced for higher $MgCl_2$ concentrations. The voltage dependence suggests that the voltage applied to trap the DNA origami structures leads to deformations as expected from the earlier measurements [112]. Fig. 3.3C shows ΔG at 500 mV as a function of the $MgCl_2$ concentration. Our experimental collaborators in the Keyser group observe that ΔG increases monotonically as $[Mg^{2+}]$ of the solution is increased. They note that the increase in the $MgCl_2$ concentration from 5.5 mM to 100 mM only leads to a 12.4% increase in the conductivity of the bulk solution from 10.5 to 11.8 S/m. However, ΔG is enhanced by a factor of 2 from ∼0.15 to ∼0.30 at 500 mV, Fig. 3.3C. This further highlights the strong interaction between the Mg^{2+} ions and the DNA origami plate.

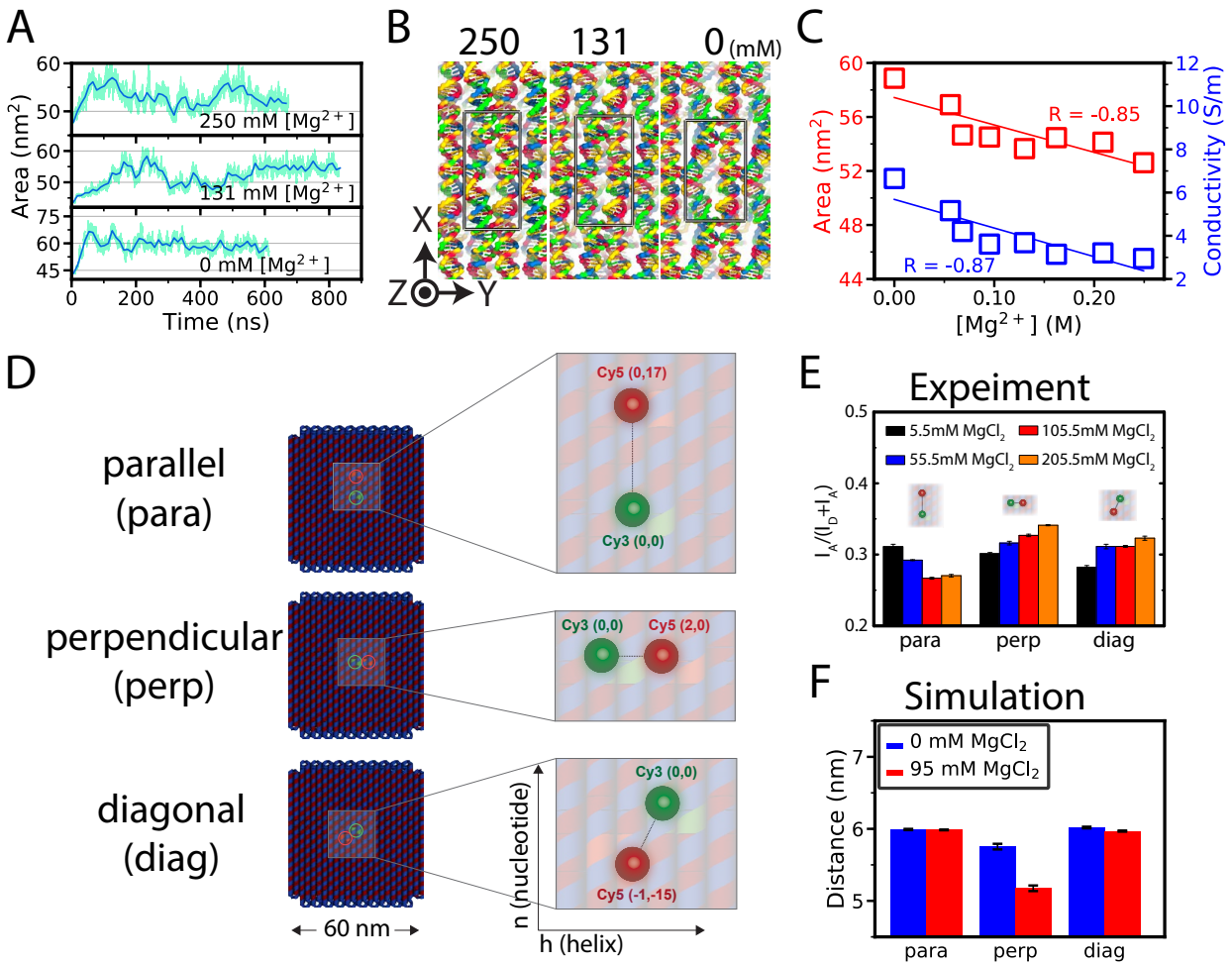

Figure 3.4: Mg^{2+} concentration regulates ionic conductivity by altering the area of DNA origami. (A) Cross-sectional area of an SQ2 plate versus simulation time for several values of bulk Mg^{2+} concentration. The area is computed within a plane normal to the direction of the ionic current (X-Y plane, Fig. 3.1). (B) Representative conformations of an SQ2 plate at several values of bulk Mg^{2+} concentration. A rectangle indicates the unit cell of the corresponding simulation system. (C) Simulated dependence of the SQ2 plate area (left) and ionic conductivity (right) on bulk concentration of Mg^{2+}. Lines are linear fits to the data. For each fit, the Pearson's correlation coefficient R is indicated in the plot. (D) Design of DNA origami plates for FRET measurements of Mg^{2+}-dependent compaction. Two fluorescently labeled staples formed a FRET pair at the center of each plate. The Cy3 donor dye (green) and the Cy5 acceptor dye (red) were aligned parallel, perpendicular and diagonal with respect to the DNA helix direction of the origami. The circles mark the location of the modified staples within the DNA origami plate. Insets specify the location of the Cy3-Cy5 pairs for each of the three designs. The DNA origami coordinates (h, n) denote the helix (h) and nucleotide (n) number relative to the Cy3 dye attached at the origin (0, 0). (E) FRET efficiency E* at a background concentration of 1 M KCl, 0.5× TBE and $MgCl_2$ concentrations of 5.5 (black), 55.5 (blue), 105.5 (red), 205.5 (orange) mM for the parallel, perpendicular and diagonal placement of the FRET pair. (F) The average distance between the estimated locations of the donor and acceptor dyes in MD simulations of the SQ2 plate at two Mg^{2+} concentrations.

MD simulations elucidated the microscopic origin of the [Mg^{2+}] dependence of the plate's conductivity. Fig. 3.4A shows the area of the SQ2 plate simulated at three different values of [Mg^{2+}] and 1 M KCl.

Although the area undergoes considerable fluctuations at a time scale of hundreds of nanoseconds, the average value decreases as $[Mg^{2+}]$ increases. Fig. 3.4B shows the representative conformations of the three systems featured in Fig. 3.4A; the dimensions of the unit cell are highlighted. Temporal fluctuations of the area were seen to become less pronounced as $[Mg^{2+}]$ was increased. Fig. 3.4C shows the simulated dependence of the area on $[Mg^{2+}]$ in the 0 to 250 mM range. For each data point, the corresponding system was simulated for more than 490 ns; the average area and $[Mg^{2+}]$ concentration were determined by averaging over the last 400 ns of each MD trajectory. The plot reveals a linear correlation between $[Mg^{2+}]$ and the area of the DNA origami plate. By setting the area of each simulation system to its average value and applying an external field, the simulations determined the dependence of the plate's conductivity on the magnesium concentration: the conductivity linearly decreases as $[Mg^{2+}]$ increases, Fig. 3.4C, in agreement with the experimental observations. Thus, increasing the concentration of Mg^{2+} ions makes the DNA origami plate more compact, decreasing its conductivity.

To independently verify the compaction of the DNA origami plates induced by Mg^{2+}, our experimental collaborators in the Keyser group performed FRET measurements on DNA origami labeled with Cy3 (donor) and Cy5 (acceptor) dyes. The fluorophore attachment sites were located in the center of the DNA origami plate and within the same plane of the plate such that the dye linkers pointed outwards from the origami. They prepared three variants of the structure having the Cy3-Cy5 pair aligned parallel, perpendicular and diagonal to the direction of the DNA helices, Fig. 3.4D. The structural integrity of the fluorescently labeled plates was confirmed by agarose (1%) gel electrophoresis. For each arrangement of the Cy3-Cy5 pair, FRET measurements were performed by gradually increasing the concentration of $MgCl_2$ in the same cuvette and collecting the emission spectra at $MgCl_2$ concentrations of 5.5, 55.5, 105.5 and 205.5 mM. This allowed them to avoid possible artifacts associated with sample variation. The apparent FRET efficiency E* was determined using a ratiometric approach, $E^* = I_A/(I_D + I_A)$, where I_A and I_D were the emission intensities of the acceptor and donor dyes, respectively, upon donor excitation. The intensities I_D and I_A were obtained by calculating the area under the emission spectra corresponding to the donor and acceptor signals. The apparent FRET efficiency was found to depend both on the orientation of the Cy3-Cy5 dyes and $MgCl_2$ concentration, Fig. 3.4E. For the perpendicular orientation, a clear increase in E* by $\sim$20% as the $MgCl_2$ concentration increased from 5.5 to 205.5 mM was observed, which our experimental collaborators in the Keyser group interpret as the reduction of the distance between the labels. A similar trend was observed for the diagonal orientation of the dyes. For labels placed along the DNA helix, increasing the $MgCl_2$ concentration from 5.5 to 205.5 mM leads to a decrease in E* by $\sim$15%.

For comparison, the estimated distance between the dye attachment sites measured from the MD tra-

jectories of the SQ2 system was plotted in Fig. 3.4F. In the experiment, the dye labels were attached near scaffold crossovers of the origami plates. My minimal models of the plates contained neither the dye molecules nor crossovers of the scaffold strand. Hence, the distance between phosphorous atoms was used to estimate the distance between the dyes. For the parallel and diagonal arrangements of the Cy3–Cy5 pair, the average distance between all pairs of phosphorus atoms that satisfied the distance restraints of the experimental design was computed, Fig. 3.4D. For the perpendicular arrangement, the average dimension of the simulation system along the Y-axis was used. The distances were averaged over the 400 ns fragments of the respective trajectories sampled every 2.4 ps. A higher separation between the dyes was observed at lower concentrations of Mg^{2+} for the perpendicular arrangement of the FRET pair, in qualitative agreement with the experiment. No statistically significant change in the FRET pair separation was determined for the parallel and diagonal arrangements of the labels.

3.5 Deformation of DNA origami plates by electric field

Being negatively charged, a DNA origami plate moves in an external electric field, loading itself on top of a nanocapillary or a solid-state nanopore [106–108, 112]. Once placed on a solid-state support, the motion of the plate is arrested, however, further deformation of the internal structure can occur under the action of the electric field.

To evaluate the nature and extent of the structural deformation, The behavior of the origami plates in MD simulations carried out without the support structure was first examined. In those simulations, a harmonic potential was applied to the center of mass of the DNA origami plate to limit the drift of the plate in the external field. Fig. 3.5 summarizes the results of my analysis. In all two-layer DNA origami structures, the distance between the layers was observed to increase with the magnitude of the electric field, Fig. 3.5A and B. We suggest that the larger deformations observed in the HX2* structure as compared to the HC2 structure were due to the missing Holliday junctions in our design, Fig. 3.5B. Such deformations were reversible. For example, by switching the electric field on and off, the distance between the layers of the SQ2 structure could be increased and reduced at a hundred nanosecond time scale, Fig. 3.5C. Analysis of the MD trajectories revealed the hydrodynamic drag of the electro-osmotic flow [116] to cause such deformation of the DNA origami plates (see below).

A different mode of deformation was observed when a DNA origami plate was put on top of a solid support, Fig. 3.6A, which is a typical situation realized in experiment. For this set of MD simulations, a $\sim$15 nm nanogap structure from amorphous SiO_2 was built and a fragment of SQ2 structure was placed

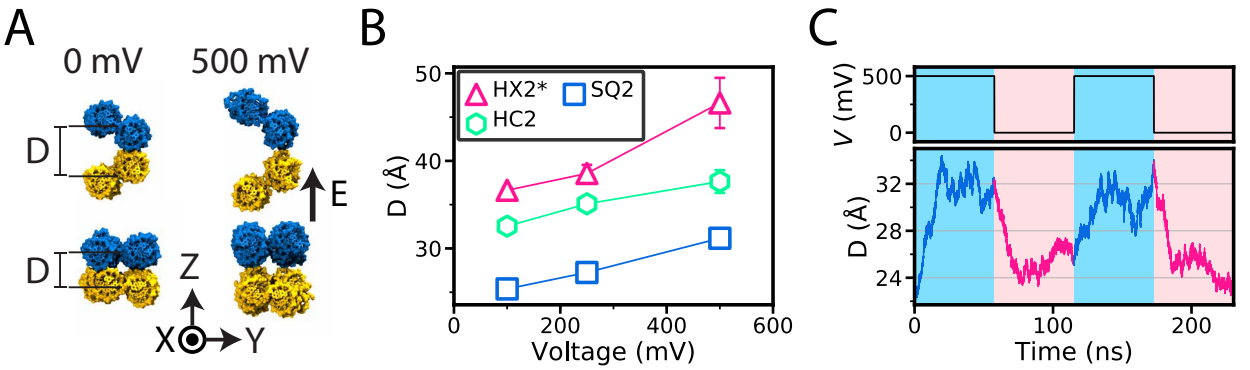

Figure 3.5: Modulation of the DNA origami structure by applied voltage. (A) Representative conformations of the SQ2 and HC2 DNA origami plates in the presence and absence of an external electric field (bias = 500 mV). The D defines the distance between the centers of mass of the scaffold strand in the upper and bottom layers of the DNA origami plate. (B) The distance between the layers of the DNA origami plates versus applied voltage. Lines are guides to the eyes. Data obtained at ∼50 M Mg^{2+}/1M KCl bulk ion concentration. (C) Reversible swelling and shrinking of the DNA origami plate by applied voltage. This set of simulations was performed at ∼250 mM Mg^{2+}/ 1 M KCl bulk ion concentration.

1 nm away from the SiO_2 structure, leaving space for the addition of Mg^{2+}-hexahydrate. In contrast to my previous setup, the origami plate was only made effectively infinite in the Y direction and was double in length of the SQ2 plate. Following ∼20 ns equilibration, the systems were subjected to applied potentials of different magnitudes.

Fig. 3.6A displays the structures observed at the end of the MD runs. The plate is observed to deform and move into the gap as the magnitude of the applied bias increased. To qualify the degree of such motion, the average distance from the origami plate's center of mass and the nearest surface of the SiO_2 structure, H, was plotted in Fig. 3.6B. The plate moved in by several Å, on average. Coincident with bending, the layers of the DNA origami structure move apart, just like in our previous simulations of bare plate system, Fig. 3.5. Under the same voltage, the layers in the bare and gap systems move apart by approximately the same degree, Fig. 3.6B. Bending of the plate increases the density of DNA nucleotides, in comparison to the density of an equilibrated SQ2 plate, Fig. 3.6C. At a 1 V bias, the DNA origami was observed to permeate through the nanogap structure.

The observed deformation of the plate structure in the hybrid system is caused by a delicate balance of the hydrodynamic drag that pushes the DNA origami away from the gap and the electrostatic force that pulls the origami into the gap. In Fig. 3.6A, the non-uniform water flux pattern was characterized by indicating the direction (arrow) and magnitude (color and line width) of the local flux using a streamplot. Fig. 3.6D compares the total flux of water through the bare and hybrid DNA origami structures. To enable direct comparison between the two systems, the figure shows the total water flux through the X-Y plane divided

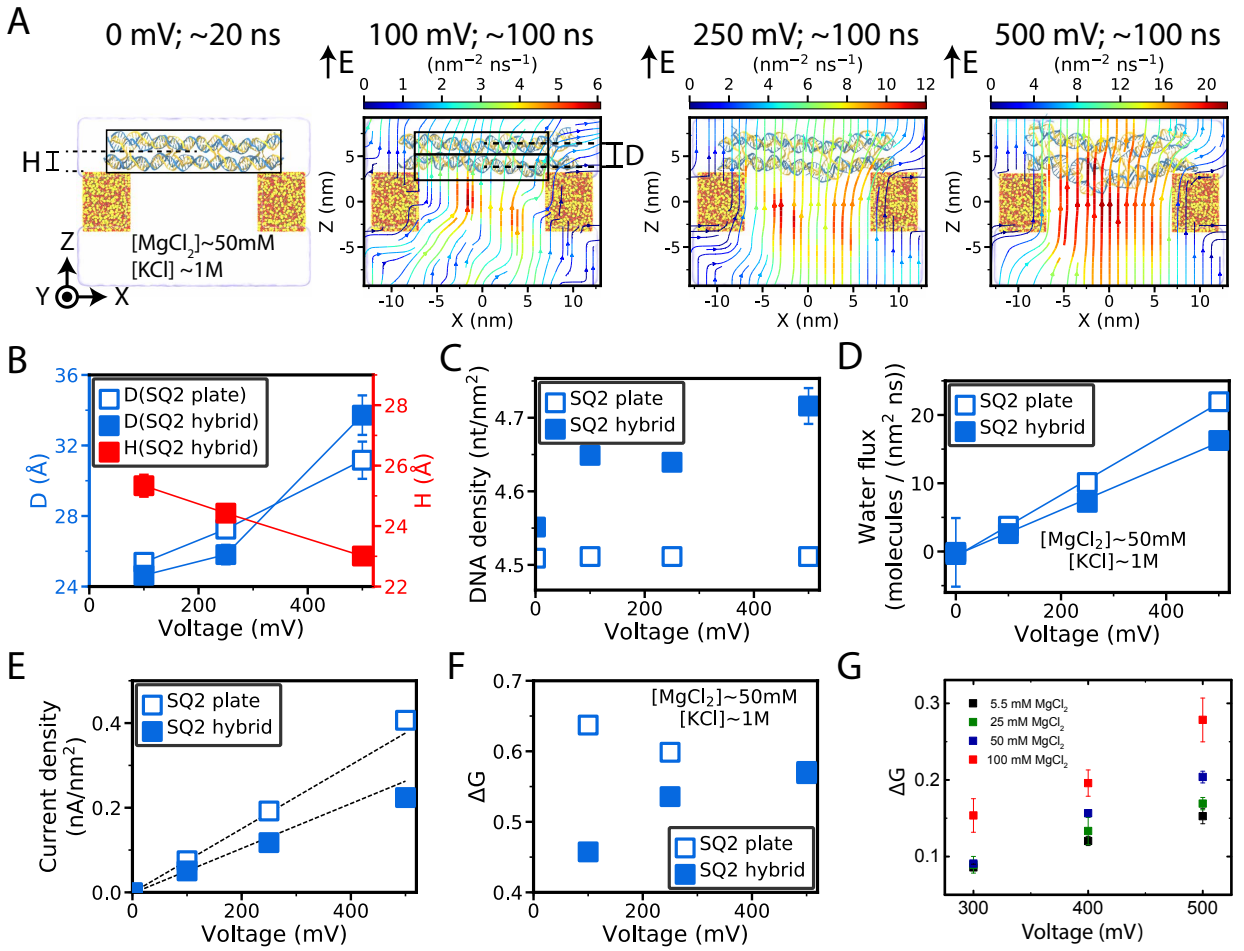

Figure 3.6: Electrical conductivity of a hybrid DNA origami / SiO_2 structure. (A) Representative conformations of a hybrid structure under applied voltage of different magnitudes. Each simulation system contained a two-layer square-lattice DNA origami, colored in blue (scaffold) and yellow (staples), placed on top of a SiO_2 nanogap, colored in yellow (Si) and red (O). Under periodic boundary conditions employed in the MD simulations, the SiO_2 structure is effectively infinite in the X-Y plane, whereas the DNA origami is effectively infinite only in the Y direction. For the systems simulated under applied potential, the magnitude of the local water flux is indicated using a colormap where the arrow heads indicate the direction of the flux lines. All systems were simulated at ~50 mM Mg^{2+}/1 M KCl bulk ion concentration. (B) The distance between the center of mass of the SQ2 plate and the top surface of SiO_2 (right) and the distance between the upper and lower layers of the SQ2 plate (left) versus applied voltage. For the hybrid structure, only the part of the DNA origami directly on top of the gap in SiO_2 was considered for calculation of D. (C) Density of the DNA origami structure on top of the SiO_2 gap versus applied voltage. The density of the SQ2 plate is shown for comparison. (D) Water flux through the hybrid and bare plate structures versus voltage. (E) Current density versus applied voltage for the hybrid and plate structures. Dashed lines are drawn from the origin through the first (100 mV) point of each dependence to emphasize the nonlinear behavior. (F) Simulated dependence of the relative conductance change ΔG on applied voltage for the hybrid and plate structures. (G) Experimental dependence of ΔG on applied voltage at several Mg^{2+} concentrations.

by the X-Y area of the system (bare origami) or the area of the gap (hybrid system). The flux is smaller in the case of the hybrid structure because of the presence of the SiO_2 structure.

Fig. 3.6E compares the $I-V$ curves of the hybrid and bare DNA origami structures normalized by the area. The $I-V$ curves are slightly nonlinear in both cases: the current increases faster than linearly in the case of the bare origami structure and slower than linearly in the case of the hybrid structure. To make the nonlinear behavior more obvious, the relative conductance blockade ΔG that was previously introduced to describe the nanocapillary measurements was plotted in Fig. 3.6F. ΔG clearly decreases in the case of a bare structure and increases in the hybrid system.

The nonlinear behavior is explained by the deformation of the origami plates. The bare system becomes more sparse as the voltage increases, Fig. 3.5, allowing more ions to pass. The hybrid system becomes more dense, additionally obstructing the passage of ions, Fig. 3.6C. For comparison, ΔG measured experimentally using the nanocapillary setup is plotted versus voltage in Fig. 3.6G. The simulated and experimental dependencies are in good qualitative agreement. Direct quantitative comparison, however, is not possible as the simulated and measured structures significantly differ from one another in terms of geometry: an infinite gap was considered in simulations whereas a long conical capillary was used in the experiment. Another factor is the presence of the guiding leash in the experiment, which could cause an additional deformation of the structure [112]. These simulations also provide an estimate of the leakage current between the DNA origami and the SiO_2 surface: within 0.5 nm of the silica surface, the ionic current was found to amount to at most 6% of the total current for the structures considered.

3.6 Anisotropic conductivity of DNA origami structures

To determine if the intrinsically anisotropic structure of a DNA origami object can cause it to have anisotropic electrical properties, The m13 SQ2 system was simulated by applying the electric field parallel and perpendicular to the DNA helices, Fig. 3.7A. Knowing the resulting ionic currents I_{X} and I_{Y}, the ionic conductivity of the SQ2 plate parallel ($\sigma_{\mathrm{o,X}}$) or perpendicular ($\sigma_{\mathrm{o,Y}}$) to the DNA helix direction can be computed using an electric circuit model that approximates the simulated system as resistors connected in parallel (please see methods in Section 3.9 and Fig. 3.9). Fig. 3.7A (Bottom) specifies the simulated directional conductivity of the plate. The DNA origami is predicted to be more conductive parallel to the DNA helices than perpendicular to them. The conductivity of the plate along the Z direction, $\sigma_{\mathrm{o,Z}}$, which is plotted in Fig. 3.2F, is similar to that of $\sigma_{\mathrm{o,Y}}$, but exhibits larger dependence on the voltage as the origami plate was free to expand in that direction.

To test the predictions of the MD simulations, Jinglin, a graduate student in Keyser group, designed a pair of cuboid-shaped DNA origami structures, Cuboid X and Y. Fig. 3.7B (Top) show the structures in

detail. Importantly, Jinglin was able to control the orientation of the cuboids on top of the nanocapillary with the help of a guiding leash attached to the different faces of the cuboids. As in the case of the DNA origami plates, the placement of Cuboid X or Y on the nanocapillary tip as a drop in the ionic current was detected until reversal of the voltage polarity ejected the cuboid structure. The trapping and ejection experiments were repeated for hundreds of times for the same nanocapillary. All experiments were carried out at 1 M KCl, 5 mM $MgCl_2$, 0.5×TBE (Tris/Borate/EDTA) and pH 8.3.

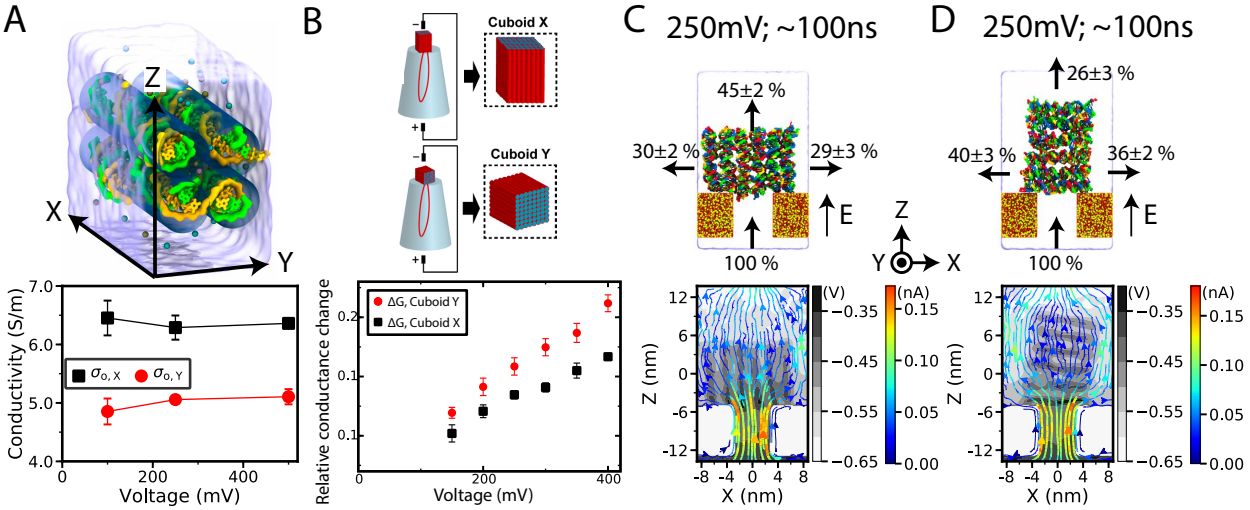

Figure 3.7: Anisotropic conductivity of DNA origami. (A) (Top) Illustration of the m13 SQ2 simulation system solvated in 1 M KCl and 50 mM $MgCl_2$. The scaffold strand (green) and the staples (yellow) are shown. The four semi-transparent blue cylinders indicate the locations of the four DNA double helices. By applying electric field in the X or Y direction and measuring the resulting ionic currents, the ionic conductivity of the plate in the X and Y directions, $\sigma_{o,X}$ and $\sigma_{o,Y}$, can be computed using a circuit model, Fig. 3.9B and C. (Bottom) Simulated ionic conductivity of the SQ2 plate parallel ($\sigma_{o,X}$) and perpendicular ($\sigma_{o,Y}$) to the DNA axis versus applied voltage. (B) (Top) Schematic of experimental measurements of the anisotropic conductivity of DNA cuboids. DNA origami cuboids are trapped on a nanocapillary in different orientations with the assistance of guiding leashes attached to different sides of the cuboids. Subject to a voltage bias, ionic current passed through Cuboid X along the DNA helices and through Cuboid Y perpendicular to the helices. (Bottom) Relative conductance change for Cuboid X and Cuboid Y systems versus applied voltage. The error bars indicate the standard error of mean computed over five independent measurements. (C, D) MD simulations of ionic current through cuboid-like structures on top of a nanogap. (Top) Typical conformations of the two cuboid-like structures at the end of MD simulations carried out under a voltage bias applied along the Z-axis. The systems shown in panels C and D differ only by the initial orientation of the DNA origami object with respect to the nanogap. The DNA origami is colored in blue (A), green (T), red (C) and yellow (G), the 5 nm SiO_2 nanogap structure is colored in yellow (Si) and red (O), water is shown as a semi-transparent surface, ions are not shown. Under periodic boundary conditions, the SiO_2 structure is effectively infinite in the X-Y plane, whereas the DNA origami is effectively infinite only in the Y direction. The numbers near black arrows indicate the average fraction of the ionic current passing through the individual faces of the cuboid-like structures. The uncertainty intervals indicate the standard error of the mean. (Bottom) The electrostatic potential map and the local current in the cuboid systems. The electrostatic potential is shown as a colormap. For clarity, the high electrostatic potential inside the SiO_2 structure is not plotted. The local current is shown as a streamplot. The arrowheads indicate the direction of the local current; the thickness and the color of the lines indicate the local current's magnitude.

For quantitative analysis, ionic current recordings for each cuboid from five nanocapillaries were chosen whose resistances ranged between 50 and 140 MΩ. For nanocapillaries of similar resistances, ΔG appears to be larger for Cuboid Y than for Cuboid X.

To directly compare the relative conductance blockades produced by Cuboids X and Y, our experimental collaborators in the Keyser group need to account for the fact that the cuboids were longer (29 nm) in one dimension (along with the DNA helices) than in the other two (both 23 nm). It was previously shown that the conductance of a DNA origami plate is determined mainly by the current that flows through the area directly above the nanopore, transverse to the plate [107]. Thus, the data can be corrected by assuming that the resistance of a DNA origami cuboid is simply proportional to its length. Scaling the resistance of Cuboid X by 23/29, our experimental collaborators in the Keyser group can arrive with an expression for the corrected relative conductance change of cuboid X, $\Delta G'_{\mathrm{X}}$, which can be directly compared to the relative conductance change of Cuboid Y, ΔG_{Y}. Fig. 3.7B (Bottom) compares the relative conductance change of Cuboid Y, ΔG_{Y}, to the relative conductance change of Cuboid X, $\Delta G'_{\mathrm{X}}$, corrected for the difference in the dimensions of the cuboids. At all voltages, $\Delta G'_{\mathrm{X}}$ is considerably smaller than ΔG_{Y}. Thus, the measurements indicate that the DNA origami structure is considerably more conductive along the DNA helix direction (Cuboid X) than normal to the DNA helices (Cuboid Y), in agreement with the predictions of the MD simulations.

MD simulations of cuboid-like structures on top of a SiO_2 nanogap demonstrate the feasibility of controlling the direction of ionic current within the DNA origami structures using their anisotropic conductivity properties, Fig. 3.7C and D. For these proof-of-principle simulations, the SQ6 origami structure was placed on top of a 5 nm SiO_2 nanogap in two orientations. Following our standard equilibration protocols, both structures were simulated at 100, 250 and 500 mV bias each. The top row of Fig. 3.7C and D details the percentage of the ionic current flowing in and out of the DNA origami structures. When the DNA helices of the structure are parallel to the electric field, most (∼90%) of the current goes through the top face of the origami cuboid. However, when the DNA helices are perpendicular to the electric field, only about half (∼50%) of the current goes through the top face of the origami cuboid. Thus, the orientation of the DNA helices clearly controls the amount of current transported normal and parallel to the nanogap surface. The bottom row of Fig. 3.7C and D details the distribution of the electrostatic potential and the local ionic currents in the cuboid-like structures. The streamlines of the current tend to avoid passing the DNA helices at a normal angle. When DNA helices are oriented parallel to the electric field, the current passes through the gaps between the DNA helices. These simulations also provide an estimate of the leakage current between the DNA origami and the SiO_2 surface: within 0.5 nm of the silica surface, the ionic current was found to

amount to at most 3% of the total current for the structures considered.

3.7 Comparison with a DNA brick plate

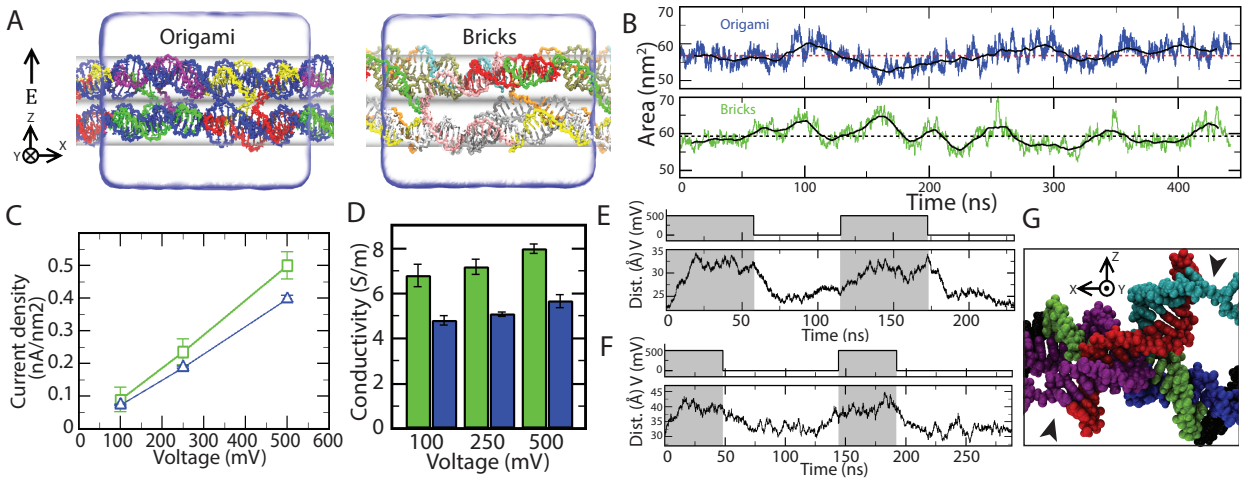

Figure 3.8: Ionic conductivity of DNA origami and DNA brick plates. (A) The DNA origami (left) [55] and DNA brick (right) systems used for simulations of ion conductivity. The scaffold strand of the DNA origami structure is shown in blue, all other strands are shown in unique colors. The blue semi-transparent surface illustrates the approximate dimension of the simulation unit cell. Each system contains 1 M KCl and 50 mM $MgCl_2$, ions are not shown for clarity. The horizontal semi-transparent cylinders are drawn to visually distinguish the top and bottom layers of the structures. In the direction of applied electric field (the Z-axis), the top and bottom layers are connected by four strands (green, purple, yellow, and red) in DNA origami and two strands (pink and orange) in DNA brick plates. Both DNA origami and DNA brick structures are effectively infinite within the X-Y plane under periodic boundary conditions; periodic images of some strands along the X direction are shown to emphasize this point. (B) The X-Y area of the DNA origami (top) and DNA brick (bottom) plates versus simulation time. The solid black lines indicate the moving average of the instantaneous X-Y area values with a moving average window of 20 ns. The dashed lines indicate the trajectory-average values of the X-Y area. (C, D) Ionic current density (panel C) and conductivity (panel D) versus transmembrane voltage of DNA origami (blue) and DNA brick (green) plates. (E, F) Reversible deformation of DNA origami (panel E) and DNA brick (panel F) plates produced by the applied electric field. Each panel, the top graph shows the duty cycle of the transmembrane bias; the bottom graph plots the average distance between the top and bottom layers of the plate. (G) A representative conformation of a DNA brick junction under a 500 mV transmembrane bias. Individual strands are shown in unique colors. The arrows indicate the locations of joint breaks in the structure. A visible twist appears in the structure with respect to the junction.

DNA brick plates can be potentially used instead of DNA origami for nanopore sensing measurements [106, 107], offering a larger design space and customization of the DNA sequence. In collaboration with Scott Michael, another graduate student in my group, we would like to know how DNA brick plates behave comparing to DNA origami plates.

To investigate the ionic conductivity of the DNA brick plates and their response to the applied electric field, we designed an effectively infinite DNA brick plate to match the dimensions of the DNA origami plate

that we have studied previously [55]. Both plates were composed of 2 layers of DNA duplexes submerged in the aqueous solution of 50 mM $MgCl_2$ and 1 M KCl, Fig. 3.8A. Similar to the DNA origami plate, the DNA brick plate was equilibrated for ∼400 ns allowing its cross section to change. Despite having the same initial dimensions, the DNA brick plate was found to have a higher cross section area than the DNA origami plate, Fig. 3.8B. The conformation closest to the average was used to start the simulations under applied electric field. The ionic current simulations were performed following a previously described method [53,67], under transmembrane bias of 100, 250 and 500 mV. Comparison of the ionic current density through the DNA brick and DNA origami plates indicates that the former is more permeable to ions, Fig. 3.8C. Consequently, the DNA brick plate has higher ionic conductivity, Fig. 3.8D.

Previously, we have shown that DNA origami plates can be reversibly swelled by the electro-osmotic flow produced by the application of the electric field [55]. To investigate the response of the DNA brick plate to an alternating electric field, the plate was simulated under a transmembrane bias that was periodically switched between 500 to 0 mV. In comparison to the response of the DNA origami plate, Fig. 3.8E, the DNA brick plate was observed to swell considerably more under a 500 mV bias, Fig. 3.8F. Upon switching the transmembrane bias off, the DNA brick plate largely recovered its structure, however, the time scale of our simulations could be too short to achieve a full recovery. Closer examination of the DNA brick structure under the applied bias revealed that the interhelical junctions, because of their single bond structure, can act as swivel points for DNA duplexes, allowing the DNA helices to move about the bond, Fig. 3.8G, which explains the larger swelling amplitude.

3.8 Conclusion

Through a combination of computer simulations and experiments, we have elucidated determinants and the microscopic mechanism of ion conductivity of DNA origami. It has already been known that the lattice type can affect the ionic conductance of the plate [113]. In accordance with the previous studies, my simulations determined the conductance of a square-lattice plate to be approximately twice that of a honeycomb one. Rather unexpectedly, both the bulk concentration of magnesium ions and the CG content of the DNA origami plate were found to affect the conductivity of DNA origami *via* the same mechanism—altering the average distance between the DNA helices in the plate. Increasing the concentration of Mg^{2+} makes the plates more compact, reducing their ability to conduct ions. Our results suggest that the leakage current through the DNA origami plates can be reduced by at least half along with the fluctuations of the current, which is expected to increase the sensitivity of ionic current measurements performed using DNA origami-based

nanopore sensors.

The structure of DNA origami plates was found to change in response to the applied electric field. Subject to the same electric field, the two-layer square-lattice plate is considerably more leaky to ions than the four- or six-layer plates because of the greater deformability of the former. Furthermore, switching on and off the electric field was found to produce reversible changes in the plate structure on a very short ($\sim$50 ns) time scale. MD simulations identified the electro-osmotic flow as the microscopic force driving the deformation of the plates. When placed on a solid-state support, the DNA origami both buckles and swells as a result of the competition between the force of the applied field driving the origami into the nanopore and the drag of the electro-osmotic flow swelling the structure. The reversible deformation of DNA origami structures in electric field may find uses in the design of nanoscale electromechanical switches.

We have also shown that the electrical conductivity of a DNA origami object can be anisotropic. Although materials science knows many examples of inorganic substances that exhibit anisotropic electrical conductivity (for example, graphite), the ability of programming the electric properties of DNA-based nanostructures has not been demonstrated, to the best of our knowledge, until now. The possibility of controlling the direction and magnitude of ionic current within a self-assembled DNA nanostructure is poised to find applications in nanofluidic electronics.

Comparing to DNA origami, a DNA brick plate is more leaky to ions than an equivalent DNA origami plate because of its lower density and larger cross-section area. Subject to external electric field, the DNA brick plate was observed to swell considerably more than the DNA origami plate and recover slower. Our work demonstrates the predictive power of the MD method in the characterization of synthetic DNA nanostructures.

3.9 Simulation and analysis methods

3.9.1 Building all-atom models of DNA origami systems

Using the caDNAno program [17], the 22-by-2 (2 layers), 8-by-4 (4 layers), 4-by-6 (6 layers) square (SQ) lattice DNA origami plates and a honeycomb (HC) lattice plate containing 14 helices arranged as 3 planar hexagons were designed. With the exception of the AT and GC SQ2 systems, for which we provided custom $(AT)_n$ and $(GC)_n$ sequences, the plates were assigned the nucleotide sequence based on the m13mp18 genome by caDNAno. Using the connectivity (.json) and the staple sequence (.csv) files, the caDNAno designs were converted to all-atom structures by the cadnano2pdb program [52]. From the all-atom structures, the 4 (SQ2 and HC2), 8 (SQ4), or 12 (SQ6) helices were extracted, forming the minimal repeat units of the

corresponding ideal lattice DNA origami designs. Under the periodic boundary conditions, the unit cells formed effectively infinite plates. The hexagonal structure (HX2*) was made by inserting a 21-bp double helix into the central pore of the HC2 structure. The additional helix was made effectively infinite under periodic boundary conditions. The AT content of the HC2, HX2*, SQ4, SQ6 plates was about 46, 48, 50 and 55%, respectively. Variation of a few percent in the AT content among the plates was expected to have a rather minor effect on the variation of the ionic current among the different designs. The SQ2 hybrid origami structure was 64-bp long and contained two unit cells of SQ2. After the all-atom model of the DNA origami structure was complete, Mg^{2+}-hexahydrates [48] were randomly placed near the structures; water and ions were added using the Solvate and Autoionize plugins of VMD. In X and Y, the dimensions of the solvation box were the same as those of the DNA origami. The initial Z dimension of the solvation box was about 2∼3 times the Z dimension of the DNA origami; the Z dimension of the system was reduced considerably during the equilibration as water entered the DNA origami structure.

3.9.2 Building all-atom models of DNA brick system

To simulate the ionic conductivity of a DNA brick structure, we used the NanoEngineer-1 software to built the minimal unit cell of a DNA brick plate, periodic within the X-Y plane. The minimal unit cell contained two DNA layers with two DNA duplexes in each layer. The DNA brick plate had the same initial dimensions, the same number of nucleotides, and the same nucleotide sequence as the DNA origami plate (SQ2). The resulting NanoEngineer design of the DNA brick plate was converted to an all-atom representation using a custom nanoengineer2pdb conversion script. The all-atom model of the DNA brick plate was merged with a pre-equilibrated volume of electrolyte solution containing 50 mM $MgCl_2$ and 1 M KCl; the solution volume was taken from the equilibrated all-atom model of the solvated DNA origami plate [55]. The final system contained ∼50,000 atoms; the electrolyte solution separated the periodic images of the plate along the Z-axis.

3.9.3 Equilibration of the all-atom models

Upon assembly, the systems were minimized using the conjugate gradient method for 9600 steps to remove steric clashes. During the minimization process, every atom of the DNA origami structure was harmonically restrained (with the spring constant $k_{\text{spring}} = 1$ kcal/(mol Å^2)) to its initial coordinates to prevent the structure from breaking. After minimization, the systems were equilibrated under the NPT condition, where the number of atoms (N), pressure (P) and temperature (T) were kept constant. The pressure was set to 1 atm using the Nosé-Hoover Langevin piston method [117, 118]. The temperature was maintained

at 295 K using a Langevin thermostat [119]. Fluctuations of the system's dimensions along the X, Y and Z axes were decoupled from one another. The systems were initially equilibrated for ∼2 ns applying harmonic restraints (k_{spring} = 1 kcal/(mol Å^2)) to every atom of the DNA origami. Next, the equilibration was continued for 10 ns applying the same-strength harmonic restraints to the atoms of the DNA bases only (excluding hydrogen atoms), allowing the DNA backbone to relax. Following that, spatial restraints were replaced by a set of harmonic potentials (k_{spring} = 1 kcal/(mol Å^2)) that confined the distances between certain atom pairs in the DNA origami (excluding hydrogen atoms, phosphate groups, atoms in the same nucleotide and pairs separated by more than 10 Å) to their initial values; each system was simulated under such restraints for ∼30 ns. Following that, the DNA origami was equilibrated without any restraints. During all stages of the equilibration process, the integrity of each Mg^{2+}-hexahydrate complex was maintained using harmonic potentials (k_{spring} = 5000 kcal/(mol Å^2)) that kept the distance between the six water molecules and the magnesium ion at 1.94 Å.

3.9.4 Adjustment of bulk ion concentration

To determine and adjust the bulk ion concentration, a system was first simulated under the NPT conditions and no restraints for 48 ns. The resulting MD trajectory was aligned to have the center of mass of the DNA origami at the origin of the system and the solution symmetrically partitioned along the Z-axis with respect to the DNA origami. The local ion concentration was computed in 1 Å bins along the Z-axis (normal to the membrane) by averaging over the X-Y plane of the MD trajectory. The 5 Å top and bottom layers (10 Å width in total) were used to measure the bulk concentration. The difference between the actual and target bulk concentrations was used to determine the number and type of ions that needed to be added to or removed from the system. Upon adjustment of the number of ions, the systems were minimized for 9600 steps and equilibrated for another 48 ns. The bulk concentration was recalculated and another adjustment to the number of ions was made, if necessary. Obtaining the target concentration within ±20 mM accuracy typically required 2∼5 iterations.

3.9.5 Construction of the hybrid system

The amorphous SiO_2 structure was obtained using a previously described annealing procedure [60]. The final structure measured 12 nm in the X direction, 5.15 nm in Y and 8 nm in Z. Under periodic boundary conditions, the SiO_2 structure represented an infinite (in the Y direction) gap, with the walls of the gap separated by ∼15 nm in the X direction. To construct a hybrid structure, the SQ2-long plate was placed across the gap 1 nm above the SiO_2 structure. Under the periodic boundary conditions, the DNA origami

plate was periodic only in the Y direction; the distance between the ends of the origami in the X direction was about ∼5.5 nm. Mg^{2+}-hexahydrate, water, K^+ and Cl^- were added as described above. As the dimension of the hybrid system was fixed in the X and Y dimensions, ∼20 ns constant area NPT equilibration was sufficient for the system to attain its equilibrium volume. In all simulations of the hybrid system, each atom of SiO_2 was harmonically restrained to its coordinates obtained at the end of the annealing procedure (with the spring constant of 20 kcal/(mol Å^2)). A DNA-specific grid-based potential was applied to reduce adhesion of DNA to SiO_2 [120, 121].

3.9.6 Calculations of the ionic conductivity

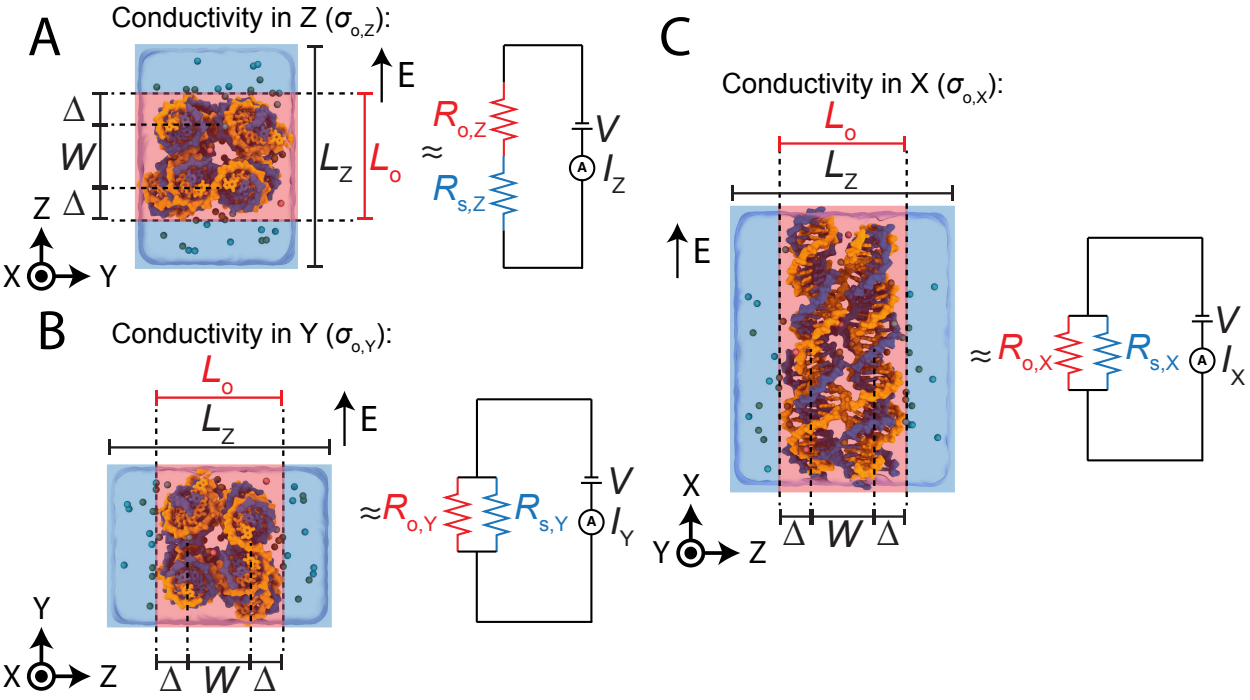

Figure 3.9: (A) Electric circuit model of the MD simulation of the DNA origami conductivity in the Z direction ($\sigma_{o,Z}$). The all-atom system containing a DNA origami plate and ionic solution is modeled as two resistors connected in series; R_o is the resistance of the origami plate and R_s is the resistance of the solution. During the applied potential simulations, the dimensions of the system L_X, L_Y and L_Z are fixed. The ionic current is determined by summing up local displacements of all charged species in the system, the applied potential $V = -L_Z E$ [67]. To compute the conductivity of the DNA origami plate, the plate's extension along the Z-axis L_o is computed as $W + 2\Delta$, where W is the average distance between the centers of mass of the top and bottom layers of the origami and $\Delta = 1.5$ nm is the extension of the ion atmosphere around a DNA helix [49]. (B, C) Electric circuit model of the MD simulation of the DNA origami conductivity in the Y ($\sigma_{o,Y}$, panel B) and X ($\sigma_{o,X}$, panel C) directions. In both cases, the systems are modeled as two resistors connected in parallel.

Fig. 3.9A illustrates the electric circuit model used to determine the conductivity of a DNA origami plate in the Z direction ($\sigma_{o,Z}$). The total resistance of the system in the Z direction

$$R_{\mathrm{t,Z}} = R_{\mathrm{o,Z}} + R_{\mathrm{s,Z}}, \tag{3.2}$$

where $R_{\mathrm{o,Z}}$ and $R_{\mathrm{s,Z}}$ are the resistances of the origami plate and solution in the Z direction, respectively. The resistance of the solution can be calculated as

$$R_{\mathrm{s,Z}} = \rho_{\mathrm{s,Z}} \frac{L_{\mathrm{s}}}{L_{\mathrm{X}} L_{\mathrm{Y}}}, \tag{3.3}$$

where $\rho_{\mathrm{s,Z}}$ is the resistivity of the solution in the Z direction, L_{X} and L_{Y} are the dimensions of the simulation system along the X and Y axes, respectively. The thickness of the solution $L_{\mathrm{s}} = L_{\mathrm{Z}} - L_{\mathrm{o}}$, where L_{Z} and L_{o} are the dimensions of the entire simulation system and of the DNA origami plate, respectively, along the Z-axis.

To determine the resistivity of the solution, we built 5.2×10.4×10.5 nm^3 (∼360 mM $MgCl_2$/1M KCl) and a 3.2×3.2×3.2 nm^3 (∼50 mM $MgCl_2$/1M KCl) systems. The systems were first equilibrated for ∼48 ns and were then subjected to the applied bias of 100, 250 or 500 mV for 9.6 ns each. The average ionic current was calculated for each system using block-averaged values sampled at 0.96 ns. The resistivity of the solution is

$$\rho_{\mathrm{s}} = \frac{V}{I} \times \frac{A}{L}, \tag{3.4}$$

where V is the bias, I is the current, L is the length of the simulation cell in the direction of the applied electric field (Z-axis in our simulations) and A is the area of the system normal to the applied field. Obtained resistivities of the two solutions did not depend on the applied bias or on the concentration of Mg^{2+}, Fig. 3.10.

To determine the conductivity of a DNA origami plate, we defined its thickness in the direction of the applied field as $L_{\mathrm{o}} = W + 2\Delta$. For square-lattice origami, W was defined as the distance between the centers of mass of the scaffold strand in the top and bottom layers of the plate. For the HC2 and HX2* plates, W was the distance between the centers of mass of the scaffold strand in the top most and bottom most helices. The extension of the ion atmosphere around DNA Δ was set to 1.5 nm, a typical value for the range of ion concentrations considered in this work [49].

The conductivity of a DNA origami plate $\sigma_{\mathrm{o,Z}} = 1/\rho_{\mathrm{o,Z}} = L_{\mathrm{o}}/(L_{\mathrm{X}} L_{\mathrm{Y}}) \times 1/(R_{\mathrm{t,Z}} - R_{\mathrm{s,Z}})$. Using Equation 3.3 for $R_{\mathrm{s,Z}}$ and V/I_{Z} for $R_{\mathrm{t,Z}}$, we obtain

$$\sigma_{\mathrm{o,Z}} = \frac{< L_{\mathrm{o}} >< I_{\mathrm{Z}} >}{V L_{\mathrm{X}} L_{\mathrm{Y}} - \rho_{\mathrm{s}} < I_{\mathrm{Z}} > (L_{\mathrm{Z}} - < L_{\mathrm{o}} >)}. \tag{3.5}$$

In the above expression, the total ionic current $< I_{\mathrm{Z}} >$ in the Z direction and the length of the DNA

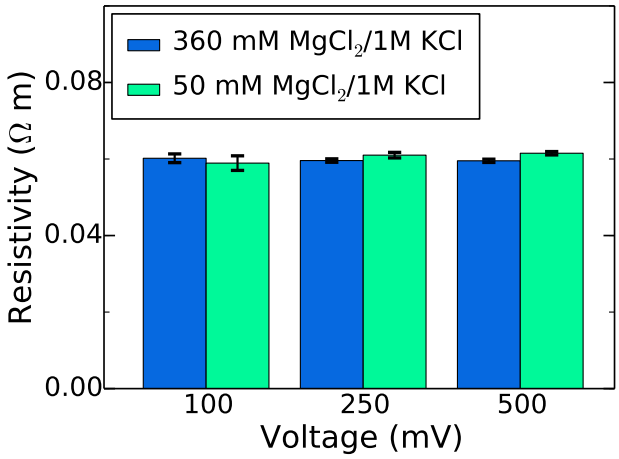

Figure 3.10: MD simulations of bulk solution resistivity. Each data point was extracted from a 9.6 ns MD trajectory sampled every 2.4 ps. The data was blocked-averaged with a block size of 0.96 ns. The error bars represent the standard error of the mean of the block-averaged data.

origami $< L_{\mathrm{o}} >$ are determined from the MD trajectory; V is the applied bias. To determine $< I_{\mathrm{Z}} >$ and $< L_{\mathrm{o}} >$, their instantaneous values $I_{\mathrm{Z}}(t)$ and $L_{\mathrm{o}}(t)$ were block-averaged from a 2.4 ps sampled trajectory using a block size of 9.6 ns. The average conductivity and the standard error were computed using the block-averaged data.

In order to calculate DNA origami conductivities in Y and X directions, $\sigma_{\mathrm{o,Y}}$ and $\sigma_{\mathrm{o,X}}$, the MD systems were modeled as resistors connected in parallel, Fig. 3.9B and C. The total resistance of each system are

$$R_{\mathrm{t,Y}} = \frac{1}{\frac{1}{R_{\mathrm{o,Y}}} + \frac{1}{R_{\mathrm{s,Y}}}} \quad \text{and} \quad R_{\mathrm{t,X}} = \frac{1}{\frac{1}{R_{\mathrm{o,X}}} + \frac{1}{R_{\mathrm{s,X}}}} \tag{3.6}$$

where $R_{\mathrm{o,Y}}$, $R_{\mathrm{o,X}}$, $R_{\mathrm{s,Y}}$ and $R_{\mathrm{s,X}}$ are the resistances of the origami plate in Y and X direction, and the resistance of the solution in Y and X direction, respectively.

Based on Equation 3.6 and the derivation above, we obtain

$$\sigma_{\mathrm{o,Y}} = \frac{< I_{\mathrm{Y}} > \rho_{\mathrm{s}} L_{\mathrm{Y}} - V L_{\mathrm{X}} (L_{\mathrm{Z}} - < L_{\mathrm{o}} >)}{L_{\mathrm{X}} L_{\mathrm{o}} V \rho_{\mathrm{s}}} \quad \text{and} \quad \sigma_{\mathrm{o,X}} = \frac{< I_{\mathrm{X}} > \rho_{\mathrm{s}} L_{\mathrm{X}} - V L_{\mathrm{Y}} (L_{\mathrm{Z}} - < L_{\mathrm{o}} >)}{L_{\mathrm{Y}} L_{\mathrm{o}} V \rho_{\mathrm{s}}} \tag{3.7}$$

Similarly, $I_{\mathrm{Y}}(t)$, $I_{\mathrm{X}}(t)$ and $L_{\mathrm{o}}(t)$ were block-averaged from a 2.4 ps sampled trajectory using a block size of 9.6 ns. The average conductivity and the standard error were computed using the block-averaged data.

Chapter 4

Biomimetic membrane-spanning DNA channels

4.1 Introduction

Membrane protein channels involved in cellular signal transductions are fascinating biological sensors with high selectivity and efficiency. Recently, it was demonstrated that DNA origami-based channels can mimic the ionic conductance and transport properties of membrane protein channels [9,109,110,122–127]. A typical DNA channel is made by arranging a few parallel DNA double helices as a polygon. The central cavity of the polygon is the transmembrane pore. The inner diameter of the DNA channel depends on the arrangement and the number of DNA double helices. To stabilize the DNA channels in a lipid bilayer membrane, the DNA channel has to be "anchored" to the lipid bilayer membrane with different hydrophobic groups, such as replacing the negative charge of DNA backbone by ethylthiolate [109], adding cholesterol [9, 125, 126] or porphyrin [110, 124], which are covalently connected to the channel. However, the structural stability and its relationship with the ionic conductance was not established.

On the other hand, until recently, most of the DNA channel designs arrange 4 or 6 parallel DNA double helices as a square [125] or hexagon [109, 110, 124, 126], giving an inner channel diameter of 1-2.5 nm. To the best of our knowledge, most previously published DNA origami channels have 6 or fewer helices in the transmembrane region, even the largest channel made with 54 DNA double helices [9]. Although the designs and functions of the self-assembled DNA structures have skyrocketed over the past decade [8, 10, 16, 128], the design space of the DNA channels is still poorly explored.

All-atom molecular dynamics (MD) simulation is currently the best way to investigate the relationship between the structural stability and the ionic conductance of the DNA channels in atomic detail. The

Reproduced with permission in part from Kerstin Göpfrich, Chen-Yu Li, Iwona Mames, Satya Prathyusha Bhamidimarri, Maria Ricci, Jejoong Yoo, Adam Mames, Alexander Ohmann, Mathias Winterhalter, Eugen Stulz, Aleksei Aksimentiev, and Ulrich F Keyser. Ion channels made from a single membrane-spanning DNA duplex. *Nano Lett.*, 16(7):4665–4669, 2016 (Copyright © 2016 American Chemical Society) and Kerstin Göpfrich, Chen-Yu Li, Maria Ricci, Satya Prathyusha Bhamidimarri, Jejoong Yoo, Bertalan Gyenes, Alexander Ohmann, Mathias Winterhalter, Aleksei Aksimentiev, and Ulrich F Keyser. Large-conductance transmembrane porin made from DNA origami. *ACS Nano*, 10(9):8207–8214, 2016 (Copyright © 2016 American Chemical Society)

predicting power of MD simulation also makes it an efficient way for the rational design of DNA channels. In 2015, Jejoong Yoo, a postdoc fellow in our group, has published the first all-atom MD study on the 6-helix channel designed by Burns *et al* [109]. In collaboration with Dr. Yoo and our experimental collaborator Dr. Keyser from the University of Cambridge, I continued to apply the all-atom MD approach to investigate the relationship between the structural stability and the ionic conductance of other channels and explore new channel designs.

4.2 MD simulations of a range of DNA channels

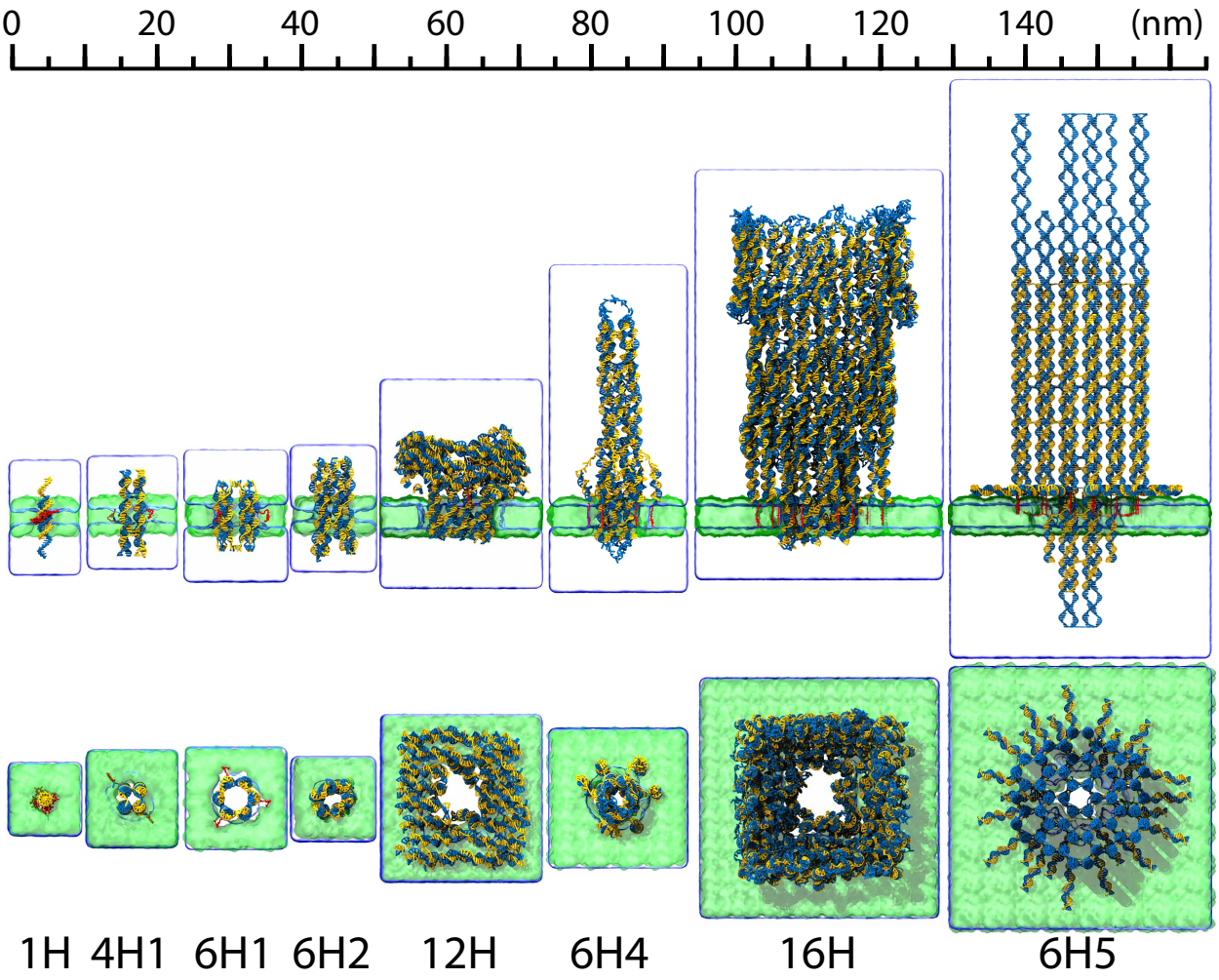

Figure 4.1: Side view (top) and top view (bottom) of the all-atom model of the DNA channels (blue and yellow) with cholesterol tags (red) embedded in a DphPC lipid membrane (green) before equilibration. The system contains magnesium ions in amount sufficient to neutralize the electrical charge of the DNA channels and 1 M KCl solution (not shown). The water and lipid molecules facing the reader were removed to show the embedded part of the channels.

Fig. 4.1 shows a representative subset of all simulated channels. For the complete list of the simulated channels, please see Table 4.1. The 1H and 16H was co-published by Göpfrich and me [122,123], in an effort to explore the design of the DNA channels. They are the smallest and largest published DNA channels so far, and will be described in Section 4.3 and 4.4. The 4H2 was the first published 4-helix channel by Göpfrich *et al* [125]. Since it looked like 4H1 with differences in the cross-over pattern, it was not explicitly shown in Fig. 4.1. The 6H1 was the simplest 6-helix channel (with only 6 DNA strands) designed by Burns *et al* [126]. The 6H2 was also designed by Burns *et al* [109], which were simulated by Dr. Yoo along with its variate 6H3 [129]. Since 6H3 looked like 6H2 with differences in the chemical modification of a few nucleotides in the transmembrane region, it was not explicitly shown in Fig. 4.1, either. The 6H2 and 6H3 were named as system I and II, respectively, in the paper [129]. The 6H5 was the first published DNA channel designed by Langecker *et al* [9]. The 12H was a large T-shaped pore (T-pore) recently published by Krishnan *et al* [127]. Although it was possible to simulate the entire T-pore, but since we were only interested in the ionic conductance and the structure at the channel-lipid interface, a truncated version of the original T-pore was simulated, which was the 12H shown in Fig. 4.1. All of the systems contain magnesium ions in amount sufficient to neutralize the electrical charge of the DNA channels and 1 M KCl solution (not shown). Please see Section 4.11 for model building and equilibration protocol.

Table 4.1: The complete list of all simulated DNA channels

Name	Number of pore-forming helices	structure size (nm)[a]	anchored by	First published by
1H	0	2.3×2.3×12.2	6 porphyrins	Co-published with Göpfrich [122]
4H1	4	5×5×13	2 cholesterols	
4H2	4	5×5×13	2 cholesterols	Göpfrich *et al* [125]
6H1	6	7×7×10	3 cholesterols	Burns *et al* [126]
6H2[c]	6	7.4×7.4×15.8	charge removal	Burns *et al* [109]
6H3[c]	6	7.4×7.4×15.8	charge removal	
6H4	6	13.4×13.4×41	6 cholesterols	
6H5	6	32.5×32.5×63.7	26 cholesterols	Langecker *et al* [9]
12H[b]	12	51×46×27	57 tocopherols	Krishnan *et al* [127]
		20.4×22×18	2 cholesterols	
16H	16	32.8×30.5×54	19 cholesterols	Co-published with Göpfrich [123]

[a] After equilibration simulation.
[b] Top: Original design. Bottom: Truncated structure for all-atom MD simulation.
[c] Simulation work done by Dr. Yoo [129].

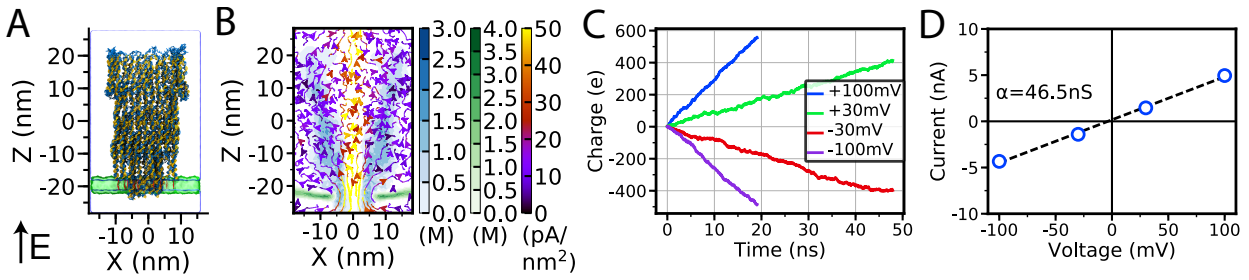

Figure 4.2: MD simulations of the 16H inserted into a DphPC lipid bilayer. (A) All-atom model of the 16H with cholesterol tags (red) embedded in a lipid membrane (green) before equilibration. The system contains magnesium ions in amount sufficient to neutralize the electrical charge of the 16H and 1 M KCl solution (not shown). Total system size: 7,963,516 atoms. Electric field, E, in direction of positive transmembrane bias as indicated. (B) Steady-state local densities of lipid chain (carbon atoms, green color scale), DNA (phosphorus atoms, blue color scale) and ion current (streamlines, purple-red-yellow color scale). The arrows indicate the direction of the local ionic current flux, and the color shows the flux' magnitude. The maps were computed from 19.2 ns long MD trajectories at a +100 mV bias sampled with a frequency of 240 ps, radially averaged about the Z-axis to improve the resolution. (C) Cumulative charge transmitted across the lipid bilayer membrane at +100 mV (blue), +30 mV (green), -30 mV (red) and -100 mV (purple) transmembrane biases. The instantaneous currents were sampled every 48 ps. The cumulative charge curves were obtained by integrating the respective instantaneous current curves versus simulation time. (D) Current-voltage characteristics. The data is block averaged with a block size of 2.88 ns. Error bars indicate the standard error of the mean, the dashed line represents a linear fit. The slope, α, is the channel's conductance.

4.3 The largest DNA channel – A DNA porin

To expand the design of the synthetic lipid membrane pores, in collaboration with Kerstin from the Keyser group, we created a larger funnel-shaped porin (16H) from DNA origami. The nominal cross section of the DNA porin is 6 nm (width of 3 DNA helices), which is wider than the cross section of large natural porins and comparable to the electrical diameter of the nuclear pore complex. To perform an all-atom MD simulation, an all-atom model including all components of the experimental system was built: the 16H itself, the DphPC lipid bilayer, ions, and water molecules, Fig. 4.2A, resulting in a system of 7,963,516 atoms. In the first 48 ns of the equilibration simulation, the 16H was restrained to its initial coordinates, allowing the membrane and the solvent to adopt an equilibrium configuration. The restraints were gradually removed over 14.4 ns. The system was subsequently simulated in the absence of restraints for another 19.2 ns. During equilibration simulations, lipid molecules rearranged around the transmembrane part of the 16H, forming a water-filled passage along the 16H's outer surface, Fig. 4.2B. Approximately 900 water molecules, or 50 per 180° segment of each DNA duplex, surrounded the 16H within a 1 nm thick rectangular slab centered at the middle plane of the membrane. The interior volume of the channel was filled with solution as well. This gives rise to an effective electrical diameter of approximately 11 nm for the 16H, making it larger than the electrical diameter proposed for the nuclear pore complex (6 nm). The equilibrium ion concentration outside the 16H was close to the target bulk values (1.1 M KCl and 20 mM $MgCl_2$); the concentration of

Mg^{2+} was found to vary considerably within the system, increasing to 0.6 M within the 16H's walls.

To evaluate its ionic conductance, the 16H was simulated at +100, +30, -30, and -100 mV transmembrane biases, reproducing the experimental voltage range. The duration of each MD simulation was 19.2 ns at ±100 mV and 48 ns at ±30 mV, which was sufficient to observe statistically significant displacement of ions within the MD trajectories [53,55,129]. The cumulative charge transmitted across the lipid bilayer over time is plotted in Fig. 4.2C. Around 80% of ions flow through the central pore, while ion flow along the outside of the channel contributes 20% to the total conductance. The I–V curve obtained from simulations, Fig. 4.2D, is ohmic and yields an average conductance of 46.5 nS. The simulated conductance is thus in very good agreement with the experimental data, taking into account the difference in the access resistance conditions and systematic overestimation of bulk electrolyte conductance in the simulation [129].

4.4 The smallest DNA channel by a single DNA duplex

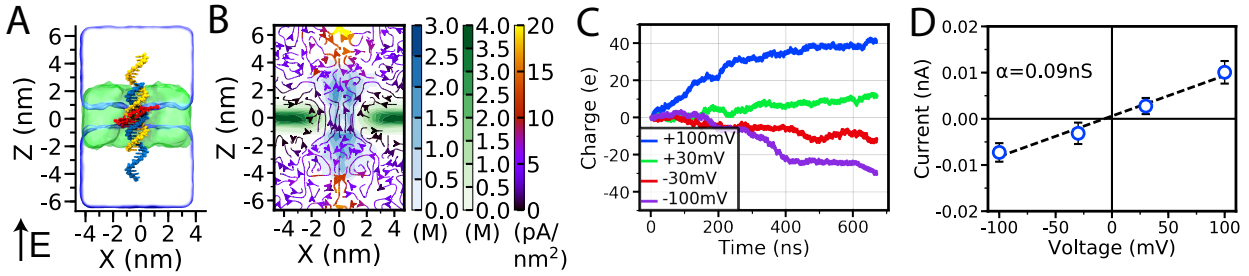

Figure 4.3: MD simulations of the 1H channel (a DNA duplex) inserted into a DphPC lipid bilayer (A) All-atom models of the duplex with hydrophobic tags (red) embedded in a lipid membrane (green) before equilibration. The system contains magnesium ions in amount sufficient to neutralize the electrical charge of the duplex and 1 M KCl solution (not shown). Total system size: 140,630 atoms. Electric field, E, in direction of positive transmembrane bias is indicated. (B) Steady-state local densities of lipid tail (carbon atoms, green), DNA (phosphorus atoms, blue) and ionic current (streamlines). The arrows indicate the direction of the local ionic current flux, the color shows the flux' magnitude. The maps were computed from a 672 ns MD trajectory at a +100 mV bias sampled with a frequency of 240 ps per frame; radially averaged about the central axis of the duplex (Z-axis) to improve the resolution. (C) Cumulative charge transmitted across the lipid bilayer at +100 mV (blue), +30 mV (green), -30 mV (red) and -100 mV (purple) transmembrane biases. The instantaneous currents were sampled every 2.4 ps. The cumulative charge curves were obtained by integrating the respective instantaneous current curves versus simulation time. (D) The simulated current-voltage characteristics. To compute the error, instantaneous ionic currents were block averaged with a block size of 9.6 ns. The error bars were computed as the standard error of the mean of the block averaged values. The dashed line represents a linear fit. The slope, α, is the channel's conductance.

From my preliminary simulation of the 4H1 channel, I found that lipid molecules around the negatively-charged DNA channel will not stay parallel to the normal of the membrane, which is the normal case for membrane protein. Instead, the surrounding lipid molecules would point the hydrophilic head group toward the DNA channel and reduce the exposure of the hydrophobic tail group to the DNA channel. As a

result, the lipid molecules around the DNA channel would form a toroidal pore. Consistent with the lipid rearrangement and formation of the toroidal pore, water and ions were found not only transport through the center of the 4H1 channel, but also the outer surface of the 4H1 channel. If that is true and not an artifact from my simulation, a single DNA duplex embedded in the lipid membrane, without an open pore, should be able to transport water and ions as well.

To verify this observation, in collaboration with Kerstin from the Keyser group, an all-atom model of the 1H embedded in a DphPC lipid bilayer submerged in 1 M aqueous solution of KCl was built analogous to the experimental conditions, Fig. 4.3A. The system was simulated by restraining the duplex to its initial coordinates in the membrane for the first 48 ns. The restraints were gradually removed over ∼15 ns, following which the 1H was simulated for ∼140 ns in the absence of any restraints. During the equilibration simulations, lipid molecules rearranged around the transmembrane part of the 1H, forming a narrow water-filled passage in its circumference, Fig. 4.3B. Approximately 100 water molecules were found on average surrounding the 1H within a 1 nm thick rectangular slab centered at the middle plane of the membrane. The ionic conductance of the 1H was determined by applying an external electric field across the lipid bilayer and measuring the instantaneous displacement of ions within the MD trajectories [53, 55, 129]. Reproducing the experimental conditions, the system was simulated at +100, +30, -30, and -100 mV transmembrane biases for ∼670 ns at each bias. Fig. 4.3C displays the cumulative charge transmitted across the 1H as a function of the simulation time at different transmembrane voltages. The slope of each curve gives the average ionic current. The plot of the average current versus transmembrane voltage, Fig. 4.3D, yields an average simulated conductances of 0.09 nS. This is in excellent quantitative agreement with the experimental conductance (0.1 nS).

Since our membrane-inserting 1H lacks a central channel, it is fundamentally different from previous DNA-based membrane pores which were composed of either four [125] or six [9, 109, 110, 124, 126] interconnected duplexes. Yet the insights gained from this study are essential for further development of this emerging class of synthetic membrane pores and settle the ongoing debate regarding the pathway of ions through DNA membrane pores [9, 124, 130]. 1Hs are expected to contribute to the total conductance of all DNA-based pores that feature an amphiphilic transmembrane domain. The total conductance of DNA pores is thus the sum of the conductance through the central pore and through the toroidal lipid pore surrounding it. The relative contributions of these two conductance pathways will depend on the pore circumference relative to its area, as well as the hydrophobicity of its exterior. In line with this argument, experiments and simulations yield lower conductances for the duplex-induced lipid channel ($\leq$ 100 pS) compared to reports of previous DNA channels (0.25-1.6 nS [9, 109, 110, 124–126]). The ionic current characteristics of the duplex-

induced toroidal pores show similarities with larger DNA pores, such as ohmic IV-behavior in the lower voltage range [9, 109, 110, 124–126], and relatively wide-spread conductance values [109, 125]. Our 1Hs are different from amphiphilic peptides that are known to destabilize lipid membranes or change bilayer thickness [131] as the induced currents can be stable and are much higher than in the latter cases. Toroidal lipid pores have been observed previously, for instance, induced by a genetically engineered α-hemolysin pore with a truncated stem [132]. Here, we provide evidence that not only peripheral but also integral membrane components can cause the reorientation of lipids and thereby formation of ion pathways lined by the lipid head groups themselves. Although our DNA duplex-induced channel and the genetically engineered α-hemolysin protein are both man-made, they provide evidence that alternative conductance pathways without a physical channel may also exist in biological systems. Indeed, it has been suggested that toroidal lipid pores, transient or stable, can be induced by amphiphilic antimicrobial peptides [133, 134], by anion channels in the TMEM16/ANO superfamily, amyloid protein aggregates [135], the HIV-1 TAT peptide [136] and due to spontaneous density fluctuations within a membrane near its phase-transition observed in experiments [137] and simulations [138].

By probing ion flux induced by a single DNA duplex in experiments and elucidating the microscopic ion pathway in MD simulations, we gain a fundamental understanding of ion conduction mechanisms across lipid membranes. Our results are of direct relevance to the ongoing debate on the physiological role of lipid channels, especially in the context of Alzheimer's disease [135] and immune response [133, 134]. Furthermore, as a duplex is stable across a wider range of conditions compared to DNA origami, it is ideally suited for applications that require specific buffers, like cell culture. Single-stranded overhangs protruding from the membrane could serve as customizable extra-membranous domains for cellular targeting and stimuli-response. Extramembranous domains could be modified to target cellular receptors or serve as metastable binding sites for signaling molecules, highlighting the level of customizability of this versatile albeit minimalistic design. Substrate-induced oligomerization will enable the creation of smaller and larger duplex-based assemblies in cellular environments. With this insightful combination of goal-oriented design, reverse-engineering, single-molecule experiments and all-atom simulations, we expect 1Hs to contribute to our understanding of ion-conduction across lipid membranes and to our ability to control it.

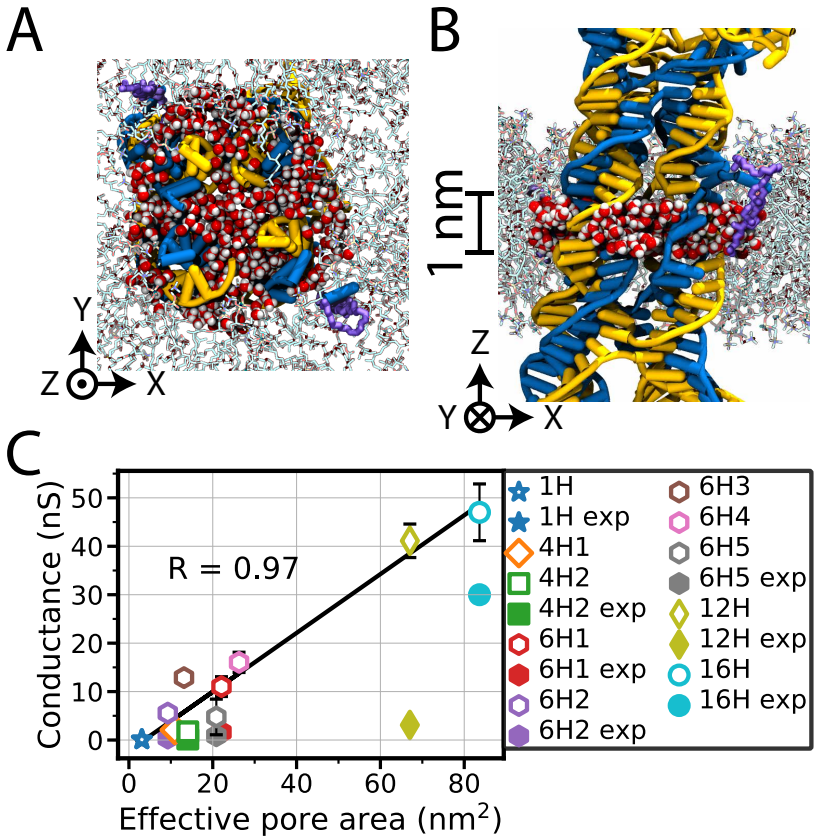

Figure 4.4: The ionic conductance of the DNA channels. (A, B) Top view (panel A) and side view (panel B) of the lipid cross-section in the 4H1 system. The 4H1 channel (blue and yellow) with hydrophobic tags (violet) embedded in a lipid membrane (C: cyan; O: red; N: blue; P: light yellow; H: not shown). A 1-nm section of water molecules (O: red; H: white) in the center of the lipid and surrounding the DNA helices were shown. The DNA and lipid molecules facing the reader were removed for clarity. (C) The ionic conductance dependence on the effective pore area. Except for 6H2 and 6H3, the ionic conductances were averaged from simulations of -100, -30, +30 and +100 mV biases. For 6H2 and 6H3, the ionic conductances were averaged from +50, +100, +200, +400 and +600 mV biases, which the data was taken from the previous study [129]. The effective pore area was defined by the number of water molecules in the 1-nm section (panel B) divided by 33.44 water molecule per nm^3. The experimental ionic conductances were also shown (filled symbols), which the effective pore area was plotted using the simulated value.

4.5 The ionic conductance of the DNA channels depends on the effective pore area

To see if all-atom MD simulation can reproduce the experimental conductance measured in other channels, all of the channels (except for 6H2 and 6H3) were simulated in -100, -30, +30 and +100 mV biases. Intuitively, the ionic conductance should be proportional to the pore size of the channels. But, after equilibration simulation, each DNA channel would depart from the idealized structure in different ways. Thus, using the pore size of the idealized pore is not a good idea. In addition, we have established that both the inside of the

channel and the surface of the channel can conduct water and ions. Using the pore area surrounded by the DNA helices does not account for the ion pathway on the outer surface of the DNA channels. An alternative way is to measure the number of water molecules in the transmembrane region of the DNA channels. Since the water molecules could be found both the inside and the outside of the channels, this method would also take the ionic pathway on the outer surface of the channels into account.

Fig. 4.4A, B show the top view (panel A) and side view (panel B) of the water molecules surrounding the DNA helices in the 4H1 system. Only the water molecules within a 1-nm slab were shown and taken into account to estimate the effective pore area. Since there are 33.44 water molecules in a 1 nm^3 volume, the effective pore area can be estimated as:

$$\text{Effective pore area } (nm^2) = \frac{\text{number of water molecules in 1-nm slab (molecules / nm)}}{33.44 \text{ (molecules / } nm^3)} \tag{4.1}$$

Fig. 4.4C shows the simulated conductance of all of the DNA channels versus the effective pore area. Except for 6H2 and 6H3, all of the simulated conductances were averaged from simulations with -100, -30, +30 and +100 mV biases. For 6H2 and 6H3, the ionic conductances were averaged from +50, +100, +200, +400 and +600 mV biases. The simulated conductance appeared to be highly correlated to the effective pore area with a Pearson's R = 0.97.

The average experimental conductances for each of the published channels were also plotted in Fig. 4.4C using the simulated effective pore area. Except for 1H and 16H, all of the simulated conductances were 2∼10 times larger than the simulated conductance. In addition to the membrane tension effect suggested by Dr. Yoo [129], this result suggested that most of the DNA channels in the experiment were less likely to be assembled on the lipid membrane as in the simulated conformation. In experiments, the DNA channels could be unfolded, deformed, tilted or even not inserted properly. In Section 4.8 and 4.9, I will describe two possible scenarios I investigated, the unfolded channel and the channel blocked by lipid molecules. Both conditions showed a significant reduction of the simulated ionic conductance.

4.6 The non-linear I–V behavior

The simulated I–V curve was found to be linear within -100∼+100 mV, Figs.4.2D and 4.3D. However, the I–V curve could become non-linear if the bias increased to 250 mV, Fig. 4.5A. The non-linear behavior also seemed to correlate with the effective pore area, Fig. 4.5B. At higher bias, the higher mobility of the water and ions increased the effective pore area. Fig. 4.5C shows an example of overlapped the pore snapshots from -250 and -100 mV. The pore in -250 mV appeared to be larger than the pore in -100 mV.

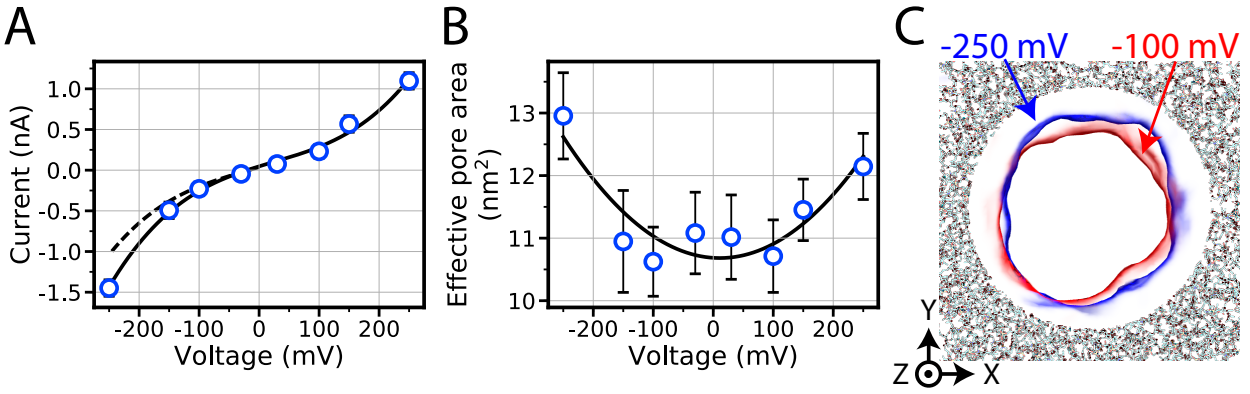

Figure 4.5: (A) The simulated I-V curve of the 4H1 channel. The solid line was the polynomial fit. The dashed line was the inverse of the upper half (voltage > 0 mV) of the solid line. The error bar as the standard error of the mean. (B) The effective pore area versus the voltage of the 4H1 channel. The solid line was the polynomial fit. The error bar as the standard error of the mean. (C) Overlapped top view snapshots of the pore in -250 (blue) and -100 (red) mV. The pores were shown as the semi-transparent molecular surface occupied by water molecules. The lipid molecules were represented the same as in Fig. 4.4A and B. The atoms of the lipid molecules which $X^2 + Y^2 > 2000$ Å^2 were hidden for clarity.

4.7 Channel aggregation could non-linearly increase ionic conductance

The experimentally measured ionic conductance are usually widespread with a few peaks [109, 125]. To see if those peaks could result from channel aggregation, two double channel systems were made by putting two 4H1 separated (4H1-4H1) and aggregated (4H1/4H1) in the lipid membrane, Fig. 4.6A. Fig. 4.6B shows the simulated ionic current per channel through the original 4H1, 4H1-4H1 and 4H1/4H1 in +250 mV bias. When the two 4H1 channel were separated (4H1-4H1), the current per channel was the same as the 4H1 alone. But, if two 4H1 channel aggregated together (4H1/4H1), the simulated current per channel became roughly twice of the current in the 4H1 alone.

To figure out why, I looked into what has changed in the conducting mechanism. Fig. 4.6C and D show the side view of the 4H1 and 4H1/4H1. Fig. 4.6E and F show the current flux through 4H1 and 4H1/4H1. The pore size in 4H1/4H1 (Fig. 4.6F) appeared to be roughly twice of the pore size in 4H1 alone (Fig. 4.6E), resulting in higher current density in the 4H1/4H1 channel. To quantitatively compare the current density, the current density in the pore (region framed by pink dashed lines) in Fig. 4.6E and F were averaged along the Z-axis, Fig. 4.6G. Both the maximum value and the width of the peak in the 4H1/4H1 were larger than in the 4H1 alone. Fig. 4.6H shows the total current through 4H1 and each 4-helix segments of the 4H1/4H1 by summing up the current density in each segment. The currents through all 4-helix segments of the 4H1/4H1 were higher than the total current of 4H1 alone. The simulation result suggested that aggregation of DNA

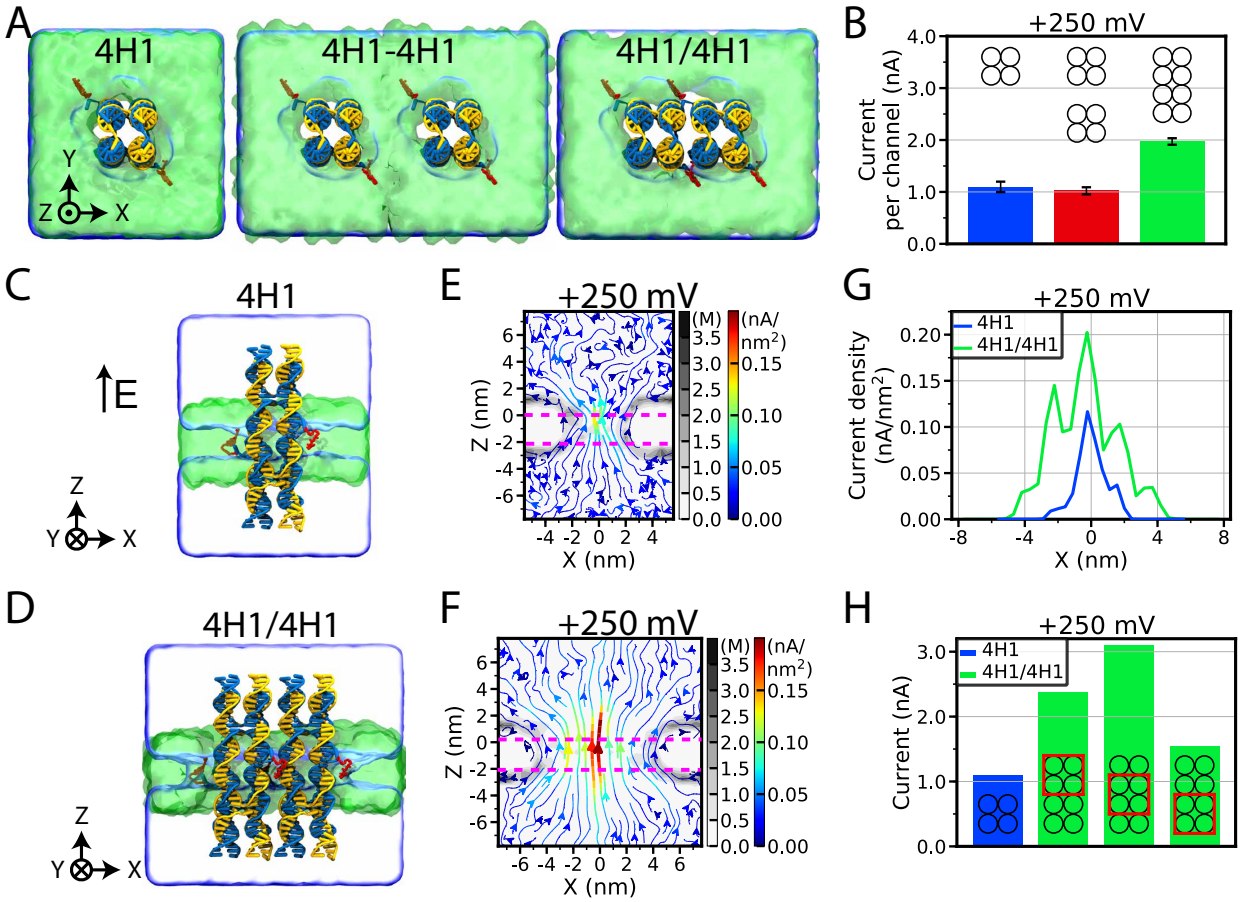

Figure 4.6: The aggregation effect on the ionic conductance of the DNA channels. (A) The top view of the systems with single 4H1, 2 separated 4H1 (4H1-4H1) and 2 aggregated 4H1 (4H1/4H1) using the same representation as in Fig. 4.1. (B) The simulated current per channel in +250mV bias. (C, D) The side view of the 4H1 (panel C) and 4H1/4H1 (panel D) system. The lipid membrane and the water molecules facing the reader have been removed for clarity. Electric field, E, in direction of positive transmembrane bias is indicated. (E, F) Steady-state local densities of lipid head group (phosphorus atoms, grayscale) and local ionic current densities in the 4H1 (panel E) and 4H1/4H1 (panel F) system in +250mV bias. The arrows indicate the direction of the local ionic current flux and the color shows the flux' magnitude. The maps were computed from the section where -2.5 nm $<$ Y $<$ 2.5 nm, containing the DNA helices (∼2.5 nm per DNA helix). The data was calculated from a ∼100 ns MD trajectory at a +250 mV bias sampled with a frequency of 240 ps per frame. (G) The current density values of the two simulations taken from -2 nm $<$ Z $<$ 0 nm (region framed by the pink dashed lines) in panel (E) and (F). (H) The ionic current through the 4H1 and each 4-helix segments of the 4H1/4H1.

channels could non-linearly increase the current and possibly produced the rare conductance peaks measured in experiments.

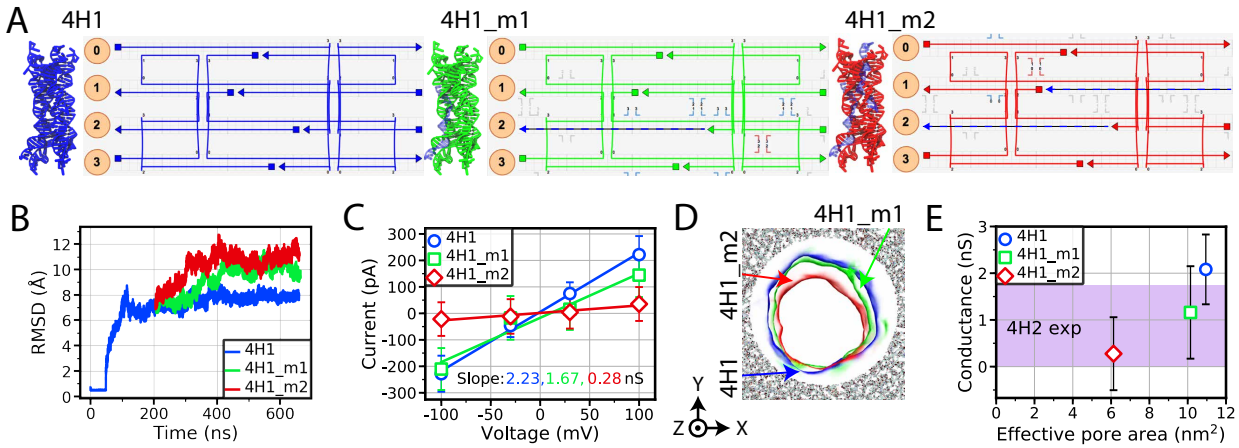

Figure 4.7: The ionic conductance dependence on the unfolding of DNA channels. (A) The equilibrated structure and the caDNAno design blueprint of the original 4H1 (left, blue), 4H1 missing 1 DNA strand (4H1_m1, center, green) and 4H1 missing 2 DNA strand (4H1_m2, right, red). The missed DNA strands in the molecular structures of 4H1_m1 and 4H1_m2 were shown transparent and blue. In the caDNAno design blueprint, the missing strands were shown as dashed blue lines. (B) The root-mean-squared-deviation (RMSD) of the three systems. The initial conformation of the 4H1_m1 and the 4H1_m2 were taken from the 4H1 after ∼200 ns equilibration simulation. (C) The simulated current-voltage characteristics of the three systems. The error bars were the standard error of the mean. The solid lines represented the linear fits. The slope of the fit were the conductances of the three systems. (D) Overlapped top view snapshots of the pore after equilibration simulation in 4H1 (blue), 4H1_m1 (green) and 4H1_m2 (red). The pores were shown as the semi-transparent molecular surface occupied by water molecules. The lipid molecules were represented the same as in Fig. 4.4A and B. The atoms of the lipid molecules which $X^2 + Y^2 > 1800$ Å^2 were hidden for clarity. (E) The ionic conductance versus the effective pore area. The purple shaded area was the range of the experimental conductance of 4H2 [125].

4.8 Channel unfolding could decrease the ionic conductance

As we saw in Section 4.5, the simulated ionic conductances were 2∼10 times higher than the experimental conductances for most of the DNA channels. The inconsistency of the ionic conductance could result from the differences between the simulated condition and the experimental condition, including differences in the channel conformation, differences in the structure of the lipid membrane, and differences in the orientation and conformation of the channel-membrane assembly. Since it is not practical to study all possibilities, I focus on two different scenarios, channel unfolding, and channel blocking by a lipid molecule. They will be described in current and Section 4.9.

To investigate the effect of channel unfolding on the ionic conductance, two variants of the 4H1 channel were built by removing 1 DNA strand (4H1_m1) and 2 DNA strands (4H1_m2), Fig. 4.7A. Since my previous simulation of 4H2 has shown that cross-overs at the termini of the channel stabilize the channel structure and it is computationally expensive and nearly impossible to sample all possible conformations of an unstable channel, only DNA strands that do not participate in the cross-over formation were removed. The initial

conformations of the 4H1_m1 and 4H1_m2 were taken from the 4H1 which has been equilibrated for ∼200 ns. Fig. 4.7B shows the root-mean-squared-deviation (RMSD) of the three systems comparing to the idealized structure of the 4H1 channel. Removing those non-cross-over-forming DNA strands had only minor impact on the overall structure of the channel.

After equilibration, the 4H1_m1 and 4H1_m2 were simulated under applied bias -100, -30, +30 and +100 mV. Fig. 4.7C shows the simulated I–V curve of the 4H1_m1 and 4H1_m2 compared to original 4H1. The ionic conductance of 4H1 decreased as more DNA strands were removed. Since both removed DNA strands were partially embedded in the lipid membrane (center of the channel were embedded in the membrane, Fig. 4.7A), the decrease could result from shrinking of the toroidal pore. Fig. 4.7D shows the overlapped snapshots of the pores in the three systems. The 4H1_m1 did have a smaller pore than 4H1 and pore of the 4H1_m2 was the smallest among the three. Indeed, the average effective pore area decreased by the removal of DNA strands, Fig. 4.7E, which was consistent with the decreasing ionic conductance. The effective pore area was calculated using the same method as described in Section 4.5. For comparison, Fig. 4.7E also shows the range of experimental conductance of 4H2 [125]. The ionic conductance of the 4H1_m1 was within the range of the experimental conductance. Furthermore, the ionic the 4H1_m2 was even close to the average experimental conductance. Thus, the simulation result verified that channel unfolding could be one of the reasons for the inconsistency between the simulated and experimental ionic conductance.

4.9 A blocked channel could have lower the ionic conductance

When the DNA channels were assembled with the lipid membrane in MD simulation, all of the lipid molecules within the channel were removed (Section 4.11). However, this may not mimic the experimental scenario. It is possible that some of the lipid molecules were trapped inside the DNA channel during the insertion process and blocking the channel. To see how lipid molecules could block the DNA channel and reduce the measured ionic conductance, a 4H1 variant was simulated by placing a lipid molecule in the center of the channel. Fig. 4.8A shows the side view of the 4H1 system using the representation as in Fig. 4.1 and the chicken wire representation which the interior of the channel is visible. Fig. 4.8B shows the zoomed-in snapshots of the original 4H1 channel (w/o lipid) and the 4H1 channel with a lipid molecule inside the channel (w/ lipid) using the chicken wire representation.

To simulate the ionic conductance and see whether the lipid molecule inside the 4H1 channel could be flush out, the 4H1 channel with a lipid was simulated with ±250 mV biases. Since the lipid molecule is electrically neutral, the only driving force to push the lipid molecule out of the channel would be the electro-

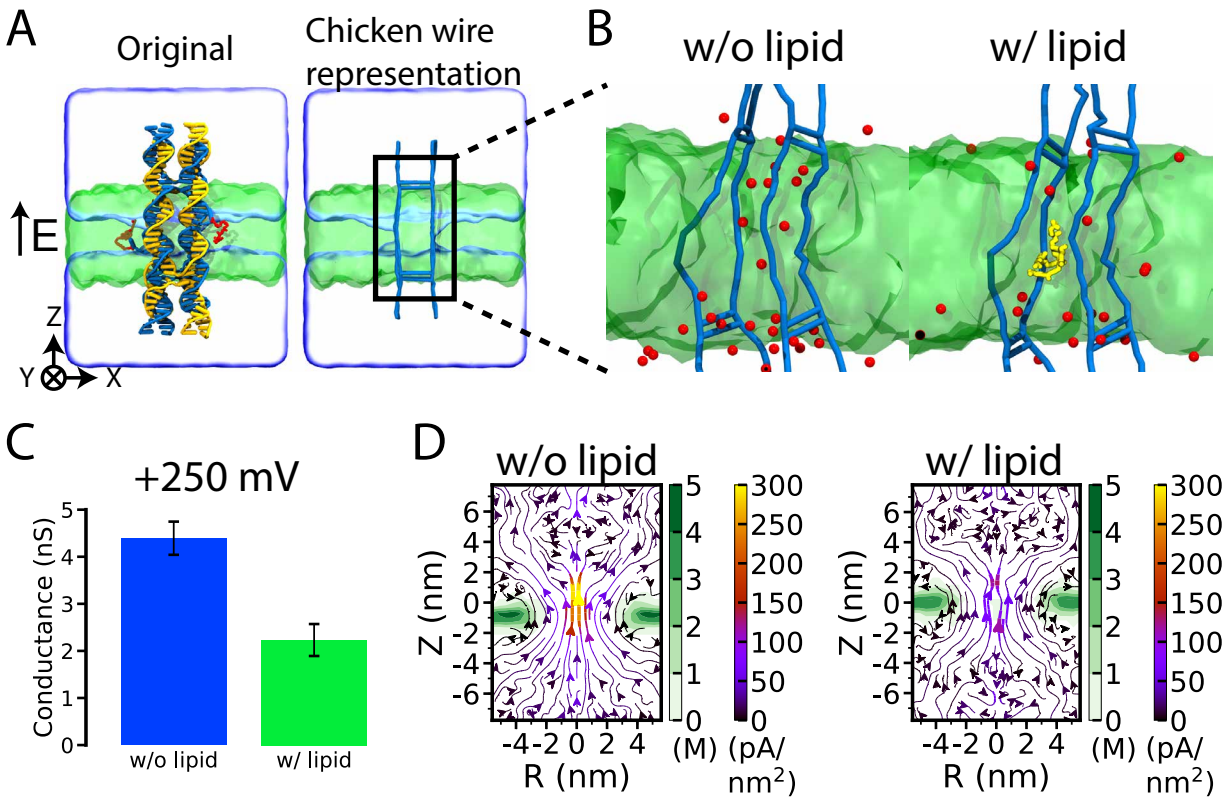

Figure 4.8: The MD simulation of a lipid molecule blocking the 4H1 channel. (A) The side view of the 4H1 system using the same representation as in Fig. 4.1 (left) and using the chicken wire representation to show the channel (right). In the chicken wire representation, DNA helices and the cross-over between the DNA helices were shown as vertical rods and horizontal rods, respectively. The single-stranded DNA overhangs on the termini of the channel were not shown. Electric field, E, in direction of positive transmembrane bias is indicated. (B) Zoomed-in snapshots of the two systems: the original 4H1 without a lipid in the channel (w/o lipid) and the 4H1 with a lipid (w/ lipid, yellow) which was placed in the center of the channel at the beginning of the simulation. The red spheres are the K^+ ion. For clarity, only 10% of the K^+ ion are shown. (C) The simulated conductances of the two systems in +250 mV bias. The error bars are the standard error of the mean. (D) Steady-state local densities of lipid tail (carbon atoms, green) and ionic current (streamlines). The arrows indicate the direction of the local ionic current flux, and the color shows the flux' magnitude. The maps were computed from a ∼100 ns MD trajectory at a +250 mV bias sampled with a frequency of 240 ps per frame; radially averaged about the central axis of the duplex (Z-axis) to improve the resolution.

osmosis (see Section 3.5). Within 100 ns of MD simulation with applied bias, the lipid molecule was still trapped inside the channel. The ionic conductance of the 4H1 channel blocked by a lipid molecule was about half of the conductance of a "clean" 4H1 channel, Fig. 4.8C. Fig. 4.8D shows the local current density of comparing the two simulations. Comparing the left and right plot of Fig. 4.8D, the lipid trapped in the channel was shown to block the ionic transport pathway and reduce the current density in the center of the channel, resulting in a lower ionic conductance. Therefore, the simulation result suggested that the DNA channels in the experiments could possibly have lipid molecules trapped inside, which resulted in a lower

ionic conductance comparing to the simulated value.

4.10 Conclusion

In conclusion, all-atom MD simulation was applied to investigate the relationship between the structural stability and the ionic conductance of a range of DNA channels. In collaboration with Keyser group from University of Cambridge, we developed the largest synthetic membrane pore using DNA origami so far. To verify the lipid rearrangement around the DNA channel predicted in my MD simulation, we designed the smallest DNA channel – a DNA duplex without an open pore. The DNA duplex was found to assembled on the lipid membrane, forming a toroidal pore and conduct water and ions. Those observations confirmed my prediction on the lipid rearrangement. The simulated ionic conductance for other DNA channels was found to be about 2∼10 times higher than the experimental conductance, but they were consistent with the effective pore area observed in the simulation. The I–V curves of the DNA channels were ohmic within ±100 mV, but non-linear I–V curve could be observed at higher biases (±250 mV). My MD simulation suggested that channel aggregation would non-linearly increase the ionic conductance, which could explain the widespread conductance measured in experiments. There are several factors which could explain the different conductances obtained in simulation and experiment. My MD simulations suggested that both channel unfolding and channel blocked a lipid molecule could result in lower ionic conductance, reproducing the experimental values.

4.11 Simulation and analysis methods

4.11.1 Assembly of the simulation systems

The caDNAno designs of all DNA channels except for 6H1 were converted to idealized all-atom structures using a previously described method [52]. The structure of the 6H1 was made with NanoEngineer-1 following the design on the paper [126]. Then, the 6H1 structure was converted to all-atom coordinates by a custom script written by me. To describe the cholesterol and porphyrin groups covalently attached to DNA, chemical models of both attachments, including all atoms of the linkers, were created; force field parameters were obtained using the CHARMM General Force Field (CGenFF) webserver. Matching the experimental design of the DNA duplex channel, porphyrin groups were added to DNA via custom patches in the conformation suggested by the previous structural model (http://www.southampton.ac.uk/∼stulz/gallery.php). For all other channels, cholesterol groups were added to termini of select DNA strands; the cholesterol groups were

initially placed to point away from the channel and usually orient normal to the plane of the lipid bilayer.

Before inserting into the lipid membrane, the structures of the 16H, 12H, 6H4 and 4H1 were simulated using the all-atom MD method for 1 ns in vacuum under a network of elastic restraints which allowed the structure to globally relax its conformation, Table 4.2 [66]. The DPhPC lipid membranes were prepared by replicating a small patch of a pre-equilibrated lipid bilayer. After merging the channel structure with the DPhPC lipid membrane, DPhPC molecules located either within 3 Å of the channel or inside the channel were removed. Mg^{2+}-hexahydrates [48] were randomly placed near the channels in the amount required to exactly compensate the electrical charge of the latter. Following that, water and 1 M KCl were added using the Solvate and Autoionize plugins of VMD.

4.11.2 Equilibration of the all-atom models

Table 4.2: The list of DNA channel simulations

Name	Atoms	Equilibration (ns)			Electric field simulation (mV; ns)							
		Position	ENM	Free[a]	-250	-150	-100	-30	30	100	150	250
1H	1.4×10^5	48	14.4	137.6	0	0	768	768	768	768	0	0
4H1[b]	2.4×10^5	48	14.4	144	96	96	144	384	384	144	0	0
4H1-4H1[b]	4.0×10^5	48	14.4	361.9	96	0	0	0	0	0	0	96
4H1/4H1[b]	3.2×10^5	48	14.4	144	96	0	0	0	0	0	0	96
4H1_m1[b]	2.4×10^5	48	14.4	601	0	0	96	96	96	96	0	0
4H1_m2[b]	2.4×10^5	48	14.4	601	0	0	96	96	96	96	0	0
4H1 w/ lipid[b]	2.4×10^5	48	14.4	192	0	0	0	0	0	0	0	96
4H2	2.4×10^5	209.3	14.4	91.2	96	0	96	96	96	96	0	96
6H1	3.1×10^5	48	14.4	19.2	0	0	38.4	96	96	38.4	0	0
6H4[b]	1.8×10^6	48	14.4	19.2	0	0	38.4	96	96	38.4	0	0
6H5[c]	1.2×10^7	48	14.4	38.4	0	0	19.2	41.3	41.3	19.2	0	0
12H[b]	1.5×10^6	48	14.4	19.2	0	0	38.4	96	96	38.4	0	0
16H[b,c]	8.0×10^6	48	14.4	19.2	0	0	19.2	48	48	19.2	0	0

[a] Unconstrained simulation.
[b] Before position-constrained simulation, the structure of those channels were relaxed with ENRG MD [66].
[c] The position-constrained simulation were only performed on the 11-nm slab containing the lipid membrane.

Upon assembly, the channel systems were minimized using the conjugate gradient method for 1200 steps to remove steric clashes. During the minimization process, all non-hydrogen atoms of the channel were harmonically restrained (with the spring constant $k_{\text{spring}} = 1$ kcal/(mol Å^2)) to its initial coordinates. After minimization, the channel systems were equilibrated under the NPT condition, where the number of atoms (N), pressure (P) and temperature (T) were kept constant. The pressure was set to 1 atm using the Nosé-Hoover Langevin piston method [117, 118]. The temperature was maintained at 295 K using a Langevin thermostat [119]. The ratios of the system's dimensions along the X- and Y-axis were constrained while the

Z-axis was decoupled.

For systems with atom number $< 5\times10^6$, the equilibration was performed using the following protocol:

In the first step of the equilibration protocol, the channel systems were simulated for 48 ns (209.3 ns for 4H2) with all non-hydrogen atoms of the channel harmonically restrained (with the spring constant $k_{\text{spring}} = 1$ kcal/(mol Å^2)) to its initial coordinates, allowing the lipid and water to equilibrate around the channel, Equilibration with "Position" constraints in Table 4.2.

In the second step, spatial restraints were replaced by a network of harmonic restraints that maintained distances between atomic pairs at their initial values; such elastic restraints excluded hydrogen atoms, phosphate groups, atoms in the same nucleotide and pairs separated by more than 8 Å. The channel systems were simulated under such elastic restraints for 14.4 ns; the spring constants of the restraints were decreased from 0.5 to 0.1 and then to 0.01 kcal/(mol Å^2) every 4.8 ns, Equilibration with "ENM" constraints in Table 4.2.

In the last step, the channel systems were simulated without any restraints for the time listed in "Free" Equilibration Table 4.2.

The 4H1-4H1, 4H1/4H1 were built by taking the initial structure of two 4H1 and putting them side-by-side after removing some (4H1-4H1) or all (4H1/4H1) lipid molecules between the 2 channels. Following that, the two systems were equilibrated using the three-step protocol. The 4H1_m1 and 4H1_m2 were built by using the equilibrated 4H1 and removing the corresponding DNA strands. After removal of the DNA strands, the two systems were equilibrated without any restraints for 457 ns. The 4H1 w/ lipid was made by adding a lipid molecule to the equilibrated 4H1. After adding the lipid molecule, the system was equilibrated without any restraints for 48 ns.

To equilibrate the systems with atom number $> 5\times10^6$ (6H5 and 16H), we first cut away an 11-nm slab of the initial all-atom model containing the lipid membrane (5 nm thick) and the adjacent 6 nm-thick cross-section of the solvated funnel. The resulting system was energy-minimized for 1200 steps and equilibrated for 48 ns allowing the lipid bilayer and the solvent to adopt equilibrium conformation around the DNA structure; the non-hydrogen atoms of DNA were restrained to maintain their initial coordinates during this equilibration simulation. Following that, the equilibrated lipid bilayer and the surrounding solvent were combined with the full-length channel structure; the resulting system was equilibrated for 14.4 ns under a network of harmonic restraints. The harmonic restraints were gradually released following the same schedule as in the case of the equilibration for smaller systems. Following that, the channels were simulated in the absence of any restraints for the time listed in "Free" Equilibration Table 4.2.

For systems having atoms $< 10^6$, the systems' coordinates were recorded every 2.4 ps. For systems with $10^6 <$ atoms $< 5\times10^6$, the systems' coordinates were recorded every 19.2 ps. For systems with atoms $>$

5×10^6, the systems' coordinates were recorded every 48 ps.

Chapter 5

Rapid lipid scrambling by artificial DNA scramblases

5.1 Introduction

The two leaflets of a mammalian cell's plasma membrane are made up from chemically distinct cocktails of phospholipids [139]: choline-containing phosphatidylcholine (PC) and sphingomyelin (Sph) are predominantly found at the outer (exoplasmic) leaflet, whereas the inner (cytosolic) leaflet contains mostly aminophospholipids phosphatidylethanolamine (PE) and phosphatidylserin (PS) [140–143]. Maintaining such an asymmetric partitioning of phospholipids is critically important to the cell's health. Loss of the asymmetry can trigger irregulated apoptosis [144] and could lead to the development of the Alzheimer's disease [145]. Three groups of enzymes—flippases, floppases and scramblases [140, 141]— can move lipids from one leaflet to the other. A flippase actively transports PE and PS lipids from outer to inner leaflets whereas a floppase actively moves PC and Sph in the opposite direction. Both groups of enzymes use energy of ATP hydrolysis to maintain the asymmetric distributions of lipids. Although phospholipids can spontaneously move from one leaflet to the other, the rate of such uncatalyzed transbilayer transport is very low in comparison to the rate of the active transport.

In some critical events including cell activation, blood coagulation and apoptosis, the asymmetric partitioning of lipids must be rapidly dismantled. At the onset of such processes, a group of enzymes—scramblases—are activated to passively and non-specifically transport the phospholipids down their concentration gradients [146–148]. Experimentally, the scrambling rate can be measured using a fluorescence quenching assay [149–152]. The highest enhancement of the lipid scrambling rate in human cells was measured in platelets, 7.8×10^{-2} s^{-1}, about two orders of magnitude faster than uncatalyzed scrambling rate of 1.8×10^{-3} s^{-1} [153]. Defects in the enzyme-catalyzed scrambling of membrane phospholipids in blood cells could hinder thrombin formation and lead to Scott syndrome [154]. In mammals, enzyme-catalyzed exposure of PS lipid to the outer leaflet signals initiation of apoptosis which plays a role in the immune response or removal of dead cells [155]. Impaired lipid scrambling has been shown to weaken the immune system and evoke the autoimmune response by exposing self-antigen [155]. Thus, development of methods

to repair and/or control lipid scrambling activity in cell membranes is of considerable medical interest.

Membrane-spanning DNA nanostructures have emerged as synthetic mimics of biological membrane channels [9, 109, 110, 122–127]. The first lipid membrane-spanning DNA channel [9] was built using the DNA origami method [8], which combines a long (tens of thousands of nucleotides) DNA strand with a collection of short strands to form a prescribed three-dimensional (3D) structure *via* self-assembly. To date, several origami-based large DNA channels [123,127] and considerably smaller, tile-like DNA pores [109,110, 122, 124–126] have been shown to insert into lipid bilayer membranes and transport water and inorganic ions in response to a transmembrane bias of electrical potential. Larger-diameter DNA channels have been shown to transport organic molecules [126, 127] including double-stranded DNA [9, 127]. Critical to stabilizing insertion of a DNA channel into a lipid membrane was the decoration of the DNA structures with hydrophobic anchors [9,110,122–127] or the removal of the negative charge of the DNA backbone [109]. Recently, we have shown that the smallest DNA channel can be built by decorating a single DNA duplex with six porphyrin groups, which, upon insertion into a lipid membrane, promote the formation of a toroidal water-filled pore surrounding the duplex. [122].

In this chapter, I show that such toroidal pores can act as scramblases, facilitating rapid mixing of lipids from leaflets. For our study, we have chosen a DNA nanostructure consisting of four interconnected DNA duplexes, two of which contain covalently linked cholesterol groups.

5.2 All-atom MD simulation of lipid scrambling facilitated by a DNA nanostructure

Following a previously described method [122,123,129], we built all-atom models of the DNA nanostructures embedded in the DPhPE lipid bilayer membrane and solvated in 1M KCl. The entire system was equilibrated for ∼230 ns using the molecular dynamics (MD) method having the DNA nanostructure restrained to its initial idealized conformation, which allowed the lipids and water to adopt an equilibrium configuration where the head group of the lipid molecules surrounded the DNA nanostructure, forming a toroidal pore, Fig. 5.1A; Please refer to the method section (Section 5.5) for the details of equilibration. The system was then simulated without any constraint for ∼2 μ; Fig. 5.1B shows the final configuration of the system. Comparison of the initial and the final configurations, Fig. 5.1A and B , reveals that several lipids have completely translocated from one leaflet to the other through the toroidal pore (indicates by red circles in Fig. 5.1B).

To gauge the magnitude of such spontaneous transleaflet transport, we computed the Z coordinate of each lipid's phosphorous atoms and its radial distance from the center of the DNA nanostructure, R, as a function

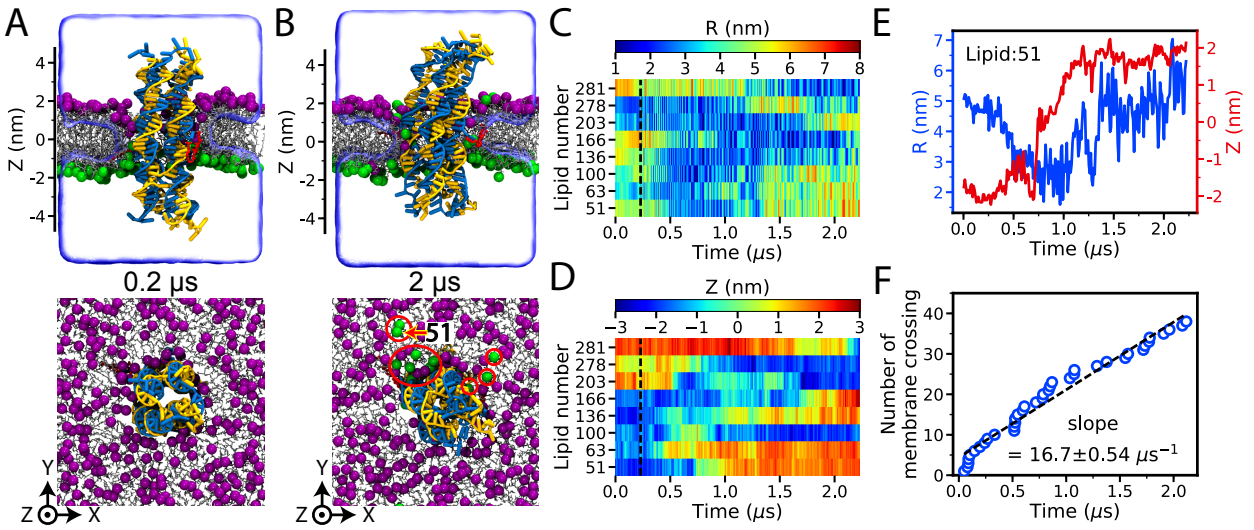

Figure 5.1: All-atom MD simulation of lipid scrambling induced by a DNA nanostructure. (A,B) Microscopic configuration of the simulated system at the beginning (panel A) and the end (panel B) of free equilibration simulation. (Top) Cut-away view of the simulated system, showing a DNA nanostructure (blue and yellow) embedded in a DphPE lipid membrane (gray) via cholesterol tags (red). The head groups of the DphPE molecules found in the upper and lower leaflets of the bilayer at 0.2 μs are highlighted using purple and green spheres, respectively. The semi-transparent molecular surface illustrates the volume occupied by 1 M KCl electrolyte, revealing a toroidal water-filled pore surrounding the nanostructure. (Bottom) Top-view of the simulated system; the electrolyte solution is not shown for clarity. The DphPE head groups that reside at 0.2 μs in the lower leaflet of the bilayer are highlighted using red circles. (C, D) The radial distance from the center of the nanostructure R (panel C) and the Z coordinate (panel D) of the phosphorus atoms of several lipids during the simulation. The radial distance was computed relative to the center of mass of the DNA nanostructure; Z=0 was defined to be at the center of mass of the lipid membrane. The black dashed lines (at 0.23 μs) indicate the beginning of free equilibration. Data shown were sampled every 0.24 ns. (E) R and Z traces of one lipid molecule (number 51, see panel B) undergoing a complete passage from the lower to the upper leaflets of the bilayer. The data shown was sampled at 0.24 ns and averaged in 9.6 ns blocks. (F) The cumulative number of membrane crossings versus simulation time. A linear fit (black line) yields the average crossing rate of 16.7±0.54 lipids per μs; the error indicates the estimated standard deviation of the non-linear least squares fit.

of the simulations time. In Fig. 5.1C and D, we plot Z and R dependences (shown as heat map) for only those lipids that were found to move from one leaflet to the other ($\max Z(t) > 1.75$ nm and $\min Z(t) < -1.75$ nm) and by at least 6 nm toward or away from the nanostructure ($\max R(t) - \min R(t) > 6$ nm).

Fig. 5.1E shows an example of one such translocation, where a lipid molecule is seen to move from the bottom leaflet ($Z > -1.75$ nm) to the top one ($Z > 1.75$ nm), approaching the DNA nanostructure ($R < 3$ nm) during the translocation process. Defining a membrane crossing event as such where the phosphorus atom of a lipid molecule changes its Z coordinate from < -1.75 nm to > 1.75 nm or *vice versa*, we plot in Fig. 5.1F the cumulative number of membrane crossings *versus* the simulation time. A linear fit to the cumulative number of crossing events plot yields the average scrambling rate of 16.7 lipids per μs. Similar spontaneous scrambling of lipids was observed in a repeat 2 μs simulation of the same DNA

nanostructure embedded in a DPhPC lipid bilayer membrane.

5.3 Coarse-grained BD simulation of lipid scrambling

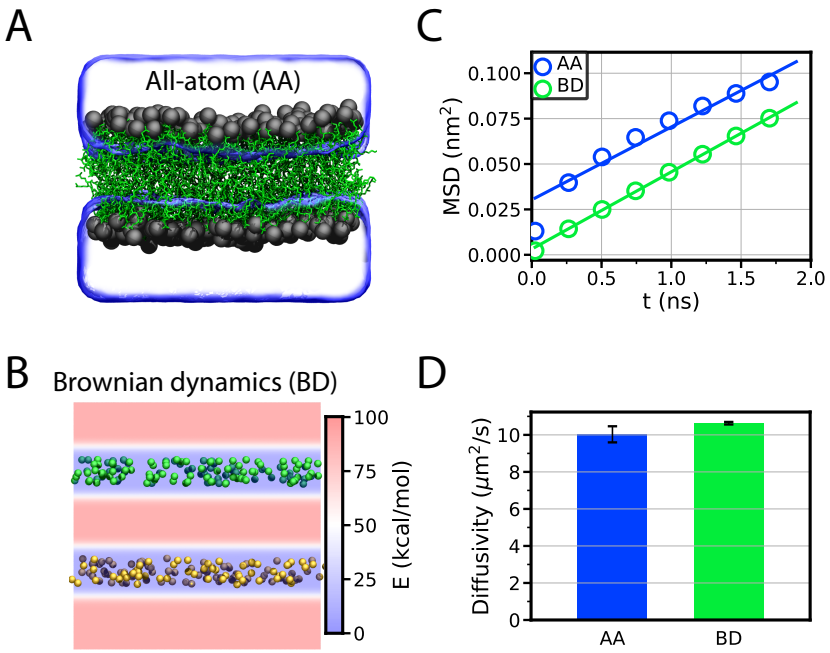

Figure 5.2: Time scale comparison for the all-atom MD and BD approaches. (A) All-atom model of a planar DPhPC lipid bilayer. The head and tail parts of the lipids are colored in black and green, respectively. The electrolyte solution (1 M KCl and 50 mM $MgCl_2$) is shown using a semi-transparent molecular surface, ions are not explicitly shown. (B) BD model of a planar lipid bilayer system. The green and yellow spheres represent the phosphorus atoms of the lipid bilayer membrane in the upper and lower leaflet, respectively. The color map illustrates a cross section of the potential energy grid that mimics the presence of the water-lipid interface. (C) Mean squared displacement (MSD) of the phosphorus atoms (AA) and beads (BB) versus intervals. (D) The 2-dimensional diffusivity in AA and BD simulation. The error bars are the standard deviation between 4 quarters of the original trajectories.

To accurately determine the lipid scrambling rate and its dependence on the pore-to-lipid ratio, we built a coarse-grained, Brownian dynamics (BD) representation of the toroidal pore surrounding a DNA nanostructure. In the BD simulation, the lipid phosphorus atoms were modeled as point-like particles (beads). All other atoms including the DNA nanostructure, lipid tail, and electrolyte solution were modeled implicitly. The beads interacted with each other through a simple repulsive potential with a 10 Å cutoff, Fig. 5.4 in Method Section 5.5. The diffusivity of each bead depended on its distance from the central axis of the pore to mimic slowing due to interactions with the DNA nanostructure, Fig. 5.5 in Method Section 5.5. A 3D grid-specified potential designed to mimic the lipid-accessible surface observed in our all-atom simulations was applied to confine the diffusion of the beads (please see Method Section 5.5 and Fig. 5.6). Using the

grid-specified potential, the steady-state local concentration of the lipid phosphorus atoms in all-atom MD simulation was reproduced with the BD beads.

To compare the timescale between the all-atom MD simulation and the Brownian dynamics simulation, a planar lipid bilayer without any DNA nanostructure or pore was simulated in both approach for ∼100 ns, Fig. 5.2. Fig. 5.2A and B are the illustrations of the planar lipid bilayer system in the all-atom MD simulation (Fig. 5.2A) and the Brownian dynamics (Fig. 5.2B) simulation. Fig. 5.2C showed the average planar mean squared displacements for each phosphorus atom or BD bead, which were then used for the calculation of the 2-dimensional diffusivity (Fig. 5.2D), as described previously [89,156]. The 2-dimensional diffusivity in the all-atom MD simulation and the Brownian dynamics simulation were consistent, suggesting the timescales between the two approach were comparable.

Fig. 5.3A illustrates the distribution of the lipid head groups at the beginning after 48 μs of BD simulation. After 48 μs, a significant portion of the beads migrated from one leaflet to the other, through the toroidal pore. Fig. 5.3B shows the Z coordinate of two representative beads in BD simulations of the system containing a lipid patch $L = 24$ nm on one side. Using the same definition of a crossing event as in the all-atom MD simulations ($\max Z(t) > 1.75$ nm and $\min Z(t) < -1.75$ nm), one can identify five crossing events in Fig. 5.3B. Defining the time interval between two crossing events as τ and taking all lipid head groups into account, we obtain a normalized probability of observing a crossing event, Fig. 5.3C, which can be fitted by the following exponential distribution $\mathrm{e}^{(-t/\tau_\circ)}/\tau_\circ$, yielding the average crossing rate, $1/\tau_\circ$, of 23 ± 1 $\mu\mathrm{s}^{-1}$. Thus, the average crossing rate observed in BD simulation is similar to that observed in all-atom simulations.

In experiment, the scrambling rate is measured using a fluorescence phospholipids quenching assay. In the assay, fluorescent 1-Oleoyl-2-[12-[(7-nitro-2,1,3-benzoxadiazol-4-yl)amino]dodecanoyl]-sn-glycero-3-phosphocholine (NBD-PC) or corresponding NBD-PE and NBD-PS derivatives are introduced to both leaflets of the membrane of the sample cells or liposomes. The dithionite anion ($[S_2O_4]^{2-}$, usually in the form of $Na_2S_2O_4$) is then added to quench the fluorescence of NBD-modified lipids in the outer leaflet of the membrane. If the scramblases are present and activated, the NBD-modified lipids from the inner leaflet would move to the outer leaflet where they would be quenched by dithionite. The measured decay of fluorescence, $F(t)/F(0)$, is then approximated by a sum of two exponential functions [153,157]:

$$\frac{F(t)}{F(0)} = Ae^{-k_1 t} + (1-A)e^{-k_2 t} \tag{5.1}$$

where A and $1-A$ are the molar fractions of the populations whose fluorescence intensity decay with rates

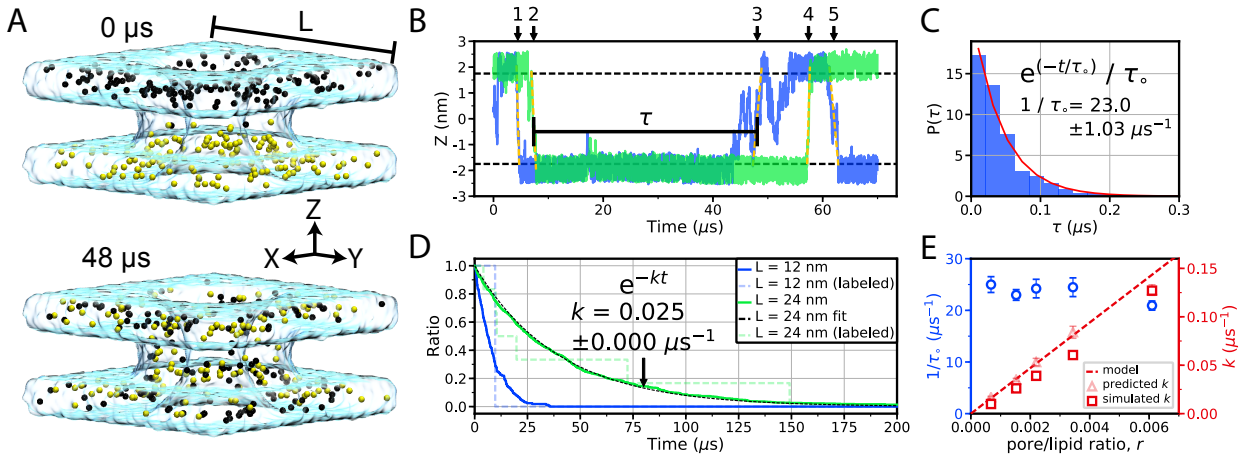

Figure 5.3: Brownian dynamics simulation of lipid scrambling. (A) Snapshots illustrating the distribution of lipid head groups at the beginning (0 μs) and after 48 μs of Brownian dynamics simulation. Black and yellow spheres represent lipid head groups initially located in the upper and lower leaflets of the bilayer, respectively. The cyan semi-transparent surface schematically illustrates the volume accessible to lipid head groups during the simulation; L denotes the size of the lipid patch. The size of the lipid patch L in the system featured here is 12 nm. (B) Z coordinates of two representative lipid head groups. The horizontal lines (at $Z = \pm 1.75$ nm) indicate the approximate boundaries of the upper and lower leaflets. To count as a crossing event, a head group must move from the upper ($Z > 1.75$ nm) to the lower ($Z < -1.75$ nm) leaflets or *vice versa*. The traces feature five such events; τ defines the interval between two consecutive crossing events. The head group trajectories were sampled every 24 ns. (C) Normalized probability of observing a crossing event within time interval τ. A fit to an exponential distribution (red line) yields the average crossing rate $1/\tau_\circ = 23 \pm 1 \mu s^{-1}$. The data was obtained from a 500 μs trajectory of the $L = 24$ nm system sampled every 24 ns. (D) The fraction of lipid head group remaining in the upper leaflets of the bilayer *versus* time elapsed from the beginning of the simulation. Data are shown for two systems differing by the size of the lipid patch. Lipids reentering the leaflet were not included in the fraction calculation. The black dashed line shows an exponential fits to the curves; the fitting parameter k is the scrambling rate. The dashed lines plot the same quantity for randomly chosen lipids that would be labeled with a dye at experimental conditions (the experimental labeling efficiency is one out of 100). (E) The simulated crossing rate (left axis) and the scrambling rate (right axis) versus pore-to-lipid ratio. The data derive from BD simulations of systems of different lipid patch size (L = 12, 16, 20, 24 and 36 nm). Scrambling rate extracted directly from the simulation is plotted using squares. The dashed line plots $k = r / < \tau_\circ >$ curve; transparent triangles indicate $k = r / \tau_\circ$, where $1/ < \tau_\circ >$ and $1/\tau_\circ$ are system size-averaged and system size-specific lipid crossing rates, respectively. The error bars indicate standard deviation.

k_1 and k_2, respectively. It is common to assume A to be the molal fraction of the fluorescently labeled lipids in the inner leaflet and interpret k_1 as the rate of lipid transport from the inner to the outer leaflet and k_2 as the rate of dithionite quenching of the fluorescently labeled lipids in the outer leaflet. Malvezzi *et al* argued that both rate constants are complex functions of the rates of scrambling and of dithionite reduction, and therefore do not represent distinct physical processes [158]. When scramblases are fully activated, the entire process is limited by the quenching reaction and the fluorescence decay is well-described by a single exponential function [158].

To determine the rate of lipid scrambling from BD simulations, we assumed quenching to occur instanta-

neously and reduced Eq. 5.1 to a single exponential function $F(t)/F(0) = e^{-kt}$. Thus, once a bead diffuses from one leaflet to the other, it becomes "quenched" immediately and, hence, we can obtain $F(t)/F(0)$ by plotting the number of beads that have never ventured to the other leaflet as a function of simulation time, Fig. 5.3D. Fitting the curve to the above expression yields the scrambling rate k. As expected, the scrambling rate depends on the system size: faster scrambling is observed for a smaller lipid-patch system, Fig. 5.3D. In experiment, fluorescently labeled lipids constitute 1∼3% of all lipids. We could mimic such selective labeling by randomly choosing 1% of all beads (1 and 6 beads for L = 12 and 24 nm system, respectively) to represent the NBD-modified lipids. The number of labeled lipids remaining in their original membrane leaflet decreased in pronounced discrete steps, Fig. 5.3D, however, when average over all possible realizations of the 1% labeling, the decay curve yielded the same average scrambling rate as when all lipid trajectories were used for the analysis.

Table 5.1: The BD simulation of different lipid patch sizes

L (nm)	Area (nm^2) per pore	r
12	144	0.0030
16	256	0.0017
20	400	0.0011
24	576	0.0008
36	1296	0.0003

To elucidate the dependence of the lipid crossing and scrambling rates on the pore density, we repeated our BD simulation for a range of lipid patch sizes (L = 12, 16, 20, 24 and 36 nm, Table 5.1)) containing the same toroidal pore. The lipid crossing rate, Fig. 5.3E, does not exhibit a strong dependence on the lipid patch size, which we characterize using the pore-to-lipid ratio r computed using the average number of lipids in one of the leaflets of the membrane. The scrambling rate, Fig. 5.3E, decreases with r. Surprisingly, a simple mathematic expression $k = r/ < \tau_\circ >$, where $1/ < \tau_\circ >$ is the system-size averaged crossing rate, can reproduce the simulated scrambling rate rather well. Thus, for the range of systems studied using the BD approach, lipid diffusion toward the toroidal pore does not appear to be the rate limiting factor.

Previous analysis of *in vitro* scrambling experiments determined the rate of lipid crossing at 0 mM Ca^{2+} at ∼400 lipids per second and that at saturating Ca^{2+} concentrations to exceed 10^4 lipids per second [158]. The liposomes used in those *in vitro* experiments each contained approximately 10^6 lipid molecules and 5 copies of the TMEM16 scramblase, yielding the maximum average crossing rate per scramblase of $2{\times}10^3$. In contrast, we found the lipid crossing rate produced by a DNA nanostructure to be in the range of 1.9–2.6×10^7 lipids per second, about 3 orders of magnitude higher than the rate of the TMEM16 scramblase.

5.4 Conclusion

In summary, we have shown that a synthetic DNA nanostructure can reproduce biological function of a scramblase protein by inducing mixing of lipids that reside on opposite leaflets of a biological membrane. In comparison to a biological scramblase, our synthetic scramblase mixes lipids much more rapidly, accelerating lipid exchange between the leaflets by at least three orders of magnitude. By adding an activation mechanism and ability to target plasma membranes of specific cell types, our present design of the DNA scramblase can be made suitable for biometical applications. On demand, target cell-specific lipid scrambling can aid patients suffering from deficient lipid scrambling or be used to trigger apoptosis of intruder cells, including cells carrying cancer specific plasma membrane antigens. Disturbance of lipid homeostasis by synthetic DNA nanostructures opens up a yet to explored direction for designing drugs and therapeutics for variety of health conditions, which differs substantially from previously suggested potential applications of DNA nanostructures as membrane-punching antimicrobial agents that release transmembrane fluxes of ions and nutrients [159].

5.5 Simulation and analysis methods

5.5.1 AA MD simulation

Assembly of the simulation systems. The caDNAno designs of the DNA nanostructure were converted to idealized all-atom structures using a previously described method [52]. To describe the cholesterol groups covalently attached to DNA, chemical models of the attachments, including all atoms of the linkers, were created; force field parameters were obtained using the CHARMM General Force Field (CGenFF) web-server. Following the design of the DNA nanostructure, cholesterol groups were added to termini of select DNA strands; the cholesterol groups were initially placed in the opposite directions relative to the DNA nanostructure.

Before inserting into the lipid membrane, the DNA nanostructure structure was simulated using the all-atom MD method for 1 ns in vacuum under a network of elastic restraints which allowed the structure to globally relax its conformation [66]. The DPhPE lipid membranes were prepared by replicating a small patch of a pre-equilibrated lipid bilayer. After merging the DNA nanostructure with the DPhPE lipid membrane, DPhPE molecules located either within 3 Å of the nanostructure or inside the nanostructure were removed. Following that, water and 1 M KCl were added using the Solvate and Autoionize plugins of VMD.

Simulation of the all-atom models. Upon assembly, the entire system was minimized using the conjugate gradient method for 1200 steps to remove steric clashes. During the minimization process, all non-hydrogen atoms of the DNA nanostructure were harmonically restrained (with the spring constant $k_{\text{spring}} = 1$ kcal/(mol Å^2)) to its initial coordinates. After minimization, the DNA nanostructure system was equilibrated under the NPT condition, where the number of atoms (N), pressure (P) and temperature (T) were kept constant. The pressure was set to 1 atm using the Nosé-Hoover Langevin piston method [117,118]. The temperature was maintained at 295 K using a Langevin thermostat [119]. The ratio of the system's dimensions along the X- and Y-axis were constrained while the Z-axis was decoupled. In the first step of the equilibration protocol, the DNA nanostructure was simulated for 205 ns with all non-hydrogen atoms of the DNA nanostructure harmonically restrained (with the spring constant $k_{\text{spring}} = 1$ kcal/(mol Å^2)) to its initial coordinates, allowing the lipid and water to equilibrate around the DNA nanostructure. Then, the spring constants of the restraints were decreased to 0.5 and then to 0.1 kcal/(mol Å^2) every 4.8 ns. In the second step, spatial restraints were replaced by a network of harmonic restraints that maintained distances between atomic pairs at their initial values; such elastic restraints excluded hydrogen atoms, phosphate groups, atoms in the same nucleotide and pairs separated by more than 8 Å. The DNA nanostructure system was simulated under such elastic restraints for 14.4 ns; the spring constants of the restraints were decreased from 0.5 to 0.1 and then to 0.01 kcal/(mol Å^2) every 4.8 ns. During all equilibration simulations of the DNA nanostructure system, the system's coordinates were recorded every 2.4 ps.

Production simulations were then performed on the Anton2 supercomputer using equivalent MD simulation parameters as described above for NAMD, except the Nosé Hoover thermostat and the Martyna-Tobias-Klein barostat were employed. The system's coordinates were recorded every 240 ps.

5.5.2 BD simulation

General BD methods Since MD is computationally expensive, the motion of lipid headgroups was modeled using Brownian dynamics (BD) simulation. BD achieves computational economy while keeping molecular-level detail by modeling the solute using simplified point-like particles and the solvent implicitly through interaction potentials [23, 160–168]. We used an in-house developed GPU-accelerated BD software package called Atomic Resolution Brownian Dynamics (ARBD) to perform the BD simulations. Beads representing lipid headgroups (specifically, phosphorus atoms) diffused through a 3D grid-specified potential designed to mimic the lipid-accessible surface observed in our all-atom simulations. The beads interacted through a simple repulsive potential with a 10 Å cutoff, see Fig. 5.4.

Each timestep of the simulation, the force on each bead was determined from the system configuration,

Figure 5.4: The potential energy between BD beads as a function of inter-bead distance.

followed by an update of the coordinates using the following formula:

$$\vec{r}_i(t+\delta t) = \vec{r}_i(t) + \frac{D(r_i)\delta t}{k_{\mathrm{B}}T}\vec{F}_i + \vec{\nabla}D(r_i)\delta t + \sqrt{2D(r_i)\delta t}\vec{w} \tag{5.2}$$

where $\vec{r}(t)$ is the position at time t, $D(r)$ is the location-dependent diffusivity, $\vec{F}$ is the deterministic force, δt is the timestep, $k_{\mathrm{B}}T$ is the thermal energy, $\vec{w}$ is a 3D vector with elements selected randomly from a standard normal distribution, and the subscript i indicates terms corresponding to particle i. In all BD simulations with the toroidal pore, the timestep was 200 fs and the diffusivity of each bead depended on its distance from the central axis of the pore to mimic slowing due to interactions with the DNA nanostructure, see Fig. 5.5. The trajectory was recorded at 2.4 ns per frame.

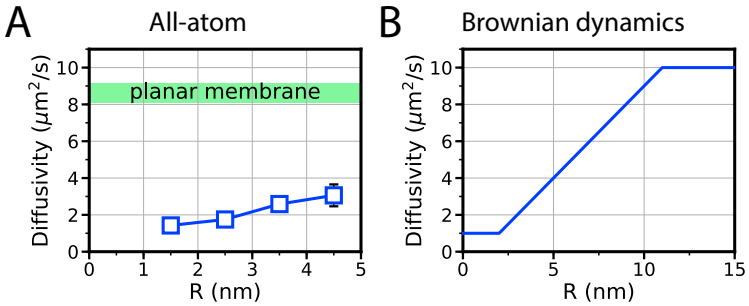

Figure 5.5: Local diffusivity of lipid head groups as a function of the distance to the central axis of the DNA nanostructure R derived from the analysis of the all-atom MD simulation (panel A) and defined in BD simulations of the toroidal pore (panel B). In panel A, the error bars indicate standard deviation evaluated by bootstrapping the MD trajectory into four equal-length parts. The green area indicates the range of lipid diffusivity values observed in the simulations of a planar DPhPC bilayer system. The membrane patch simulated using the all-atom MD method is too small for the lipids to attain diffusive properties of a free bilayer system. (B) The functional form of local diffusivity assumed in BD simulations of the toroidal pore system.

In the BD simulation of a planar lipid membrane (Fig. 5.2B), the timestep was 2 fs and the trajectory was recorded at 2.4 ps per frame.

Creation of the potential grid. The potential grid was created using the gridData module in Python. The following steps show how to create the potential grid for the L = 12 nm system. For all other systems, simply change the grid dimensions in X and Y direction to the corresponding L.

Step 1: To make a 12 nm × 12 nm × 10 nm grid, a 3-dimensional grid with (12 + 2 × padding) × (12 + 2 × padding) × (10 + 2 × padding) was first created. The padding is used as the buffer zone to avoid numerical error which occurs at the boundary in convolution. The padding was set to 1 nm our protocol. With a resolution of 0.1 nm, the range of X, Y and Z are -7 $\leq$ X $<$ 7, -7 $\leq$ Y $<$ 7 and -6 $\leq$ Z $<$ 6 with a minimal step of 0.1 nm. Each grid point can take a value, which represents the potential energy at the given coordinate. In order to mimic the bilayer membrane, all of the grid points in -2.2 $<$ Z $<$ -1.8 and 1.8 $<$ Z $<$ 2.2 were set to be 100 and all other grid points were set to be 0, Fig. 5.6A. Although the bilayer membrane has a higher potential energy now, the differences in the potential energy will be reversed later.

Step 2: The toroidal shape of the pore was made by the catenoid function in the cylindrical coordinates:

$$\rho = c \times \cosh\frac{\mathrm{Z}}{c} \tag{5.3}$$

where $\rho = \sqrt{\mathrm{X}^2 + \mathrm{Y}^2}$ and c was set to 2 . All grid points with 2.25 $<$ ρ - $c \times \cosh\frac{\mathrm{Z}}{c}$ $<$ 2.75 and -1.8 $<$ Z $<$ 1.8 were set to 100, Fig. 5.6B.

Step 3: To remove the high potential energy in the pore, all grid points with ρ - $c \times \cosh\frac{\mathrm{Z}}{c}$ $<$ 2.25 were set to 0, Fig. 5.6C. Now, we have a pore in the lipid bilayer membrane.

Step 4: To increase the thickness of the pore, the grid was convolved with a spherical function with radius 0.9 nm using the scipy.signal.fftconvolve function in Python, Fig. 5.6D.

Step 5: To reverse the potential energy difference, all grid points with values larger than 1 were set to 0 and all grid points with values less than 1 were set 100. Then, the grid was convolved with a Gaussian function (μ = 1.1, σ = 0.2) to smooth the boundary between the low and high potential energy region, Fig. 5.6E.

Step 6: To remove the numerical error in the convolution, the grid was trimmed by removing the padding which was added initially, Fig. 5.6F.

Initialization of the BD simulation. The initial coordinates X and Y of each bead were randomly generated using a homogeneous distribution within the range of the system dimension L. The initial coordinates Z was set to be either 2 or -2 nm with equal probability. The number of beads was set to satisfy 0.878 nm^2

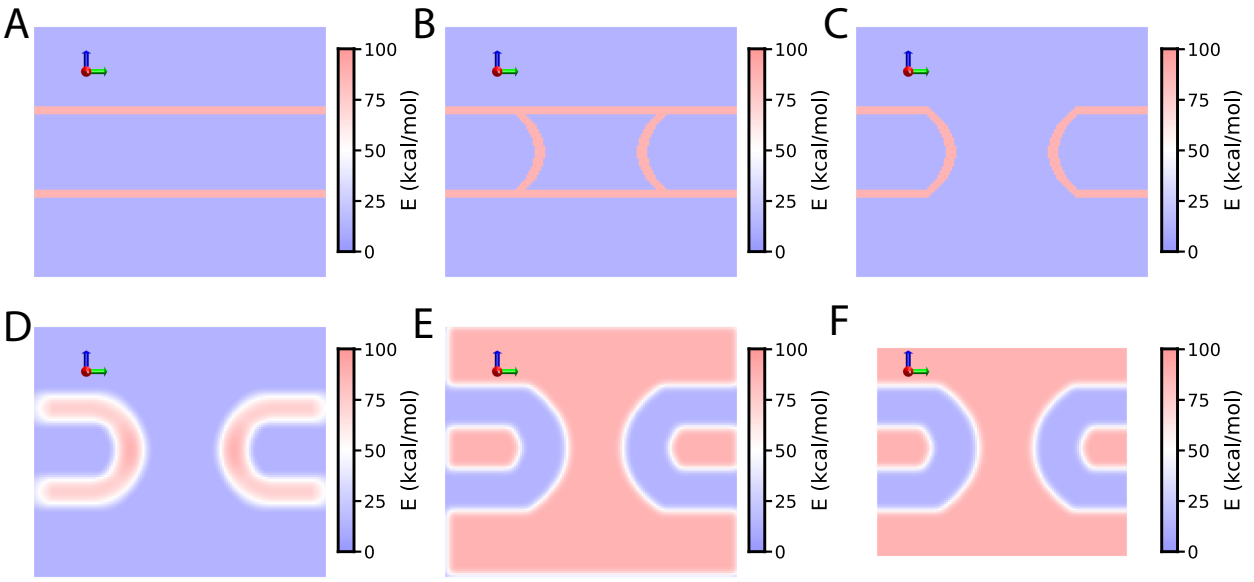

Figure 5.6: Generation of the 3D grid-based potential for BD simulation of the toroidal pore. The sequence of images illustrate the six steps of the potential generation procedure. Each image shows the same cross section of the 3D potential map; the plane of the cross section passes normal to the membrane through the central axis of the toroidal pore.

area per bead.

5.5.3 Calculations of the lipid diffusivity

The lipid diffusivity was calculated using the protocol described previously [89, 169]. The diffusivity can be calculated from the Einstein relation on the Brownian motion:

$$2d_f D = \lim_{t\to\infty} \frac{1}{t} < (r(t) - r(0))^2 > \tag{5.4}$$

where d_f is the number of translational degrees of freedom and $r(t)$ is the position of the molecule at time t. Although the phosphorus atoms of the lipid were confined on a surface and did not satisfy the free diffusion requirement, since I only needed to validate the BD simulation with the AA simulation and did not need a quantitatively accurate calculation of the diffusivity, this approach was applied.

In practice, the trajectories were first aligned so that the center of the pore or the planar lipid membrane was located at the origin. Then, the trajectories of the phosphorus atoms in the lipid molecule (AA) or beads (BD) were extracted and cut into 20 ns segments. For position-dependent diffusivity, each segment was categorized into groups based on the average radial distance from the origin with a bin size of 1 nm. For the diffusivity of the planar lipid membrane (Fig. 5.2), all segments were in the same group. Next, the mean square displacements d^2 averaged over all molecules N for each group were calculated [170]:

$$d^2(t) = \frac{1}{N}\frac{\Delta t}{T-t}\sum_{i=1}^{N}\sum_{t_0=0}^{T-t-1}|r(t_0) - r(t_0+t)|^2 \tag{5.5}$$

The first sum runs over the N molecules and the second sum runs over all time frames smaller than $T-t$, where T is the sampling time (20 ns), t_0 is the time of the first frame in the trajectory segment and Δt is the time between two frames. A linear least-squares fit of the mean-square displacement d^2 as a function of t was performed for each group. For planar 2-dimensional diffusivity (Fig. 5.2), the $r(t)$ only considered the X and Y coordinate of each atom and the diffusivity was given by 1/4 of the slope of the fitting line. For 3-dimensional diffusivity, the X, Y and Z coordinate of each atom were taken into account and the diffusivity was 1/6 of the slope.

References

[1] Robin Holliday. A mechanism for gene conversion in fungi. *Genet. Res.*, 5(02):282–304, July 1964.

[2] Michael R. Lieber, Yunmei Ma, Ulrich Pannicke, and Klaus Schwarz. Mechanism and regulation of human non-homologous DNA end-joining. *Nat. Rev. Mol. Cell Biol.*, 4(9):712–720, 2003.

[3] Nadrian C. Seeman. Nanomaterials based on DNA. *Annu. Rev. Biochem*, 79:65–87, 2010.

[4] J. H. Chen and N. C. Seeman. Synthesis from DNA of a molecule with the connectivity of a cube. *Nature*, 350(6319):631–3, 1991.

[5] Yonggang Ke, Jaswinder Sharma, Minghui Liu, Kasper Jahn, Yan Liu, and Hao Yan. Scaffolded DNA origami of a DNA tetrahedron molecular container. *Nano Lett.*, 9(6):2445–7, June 2009.

[6] William M. Shih, Joel D. Quispe, and Gerald F. Joyce. A 1.7-kilobase single-stranded DNA that folds into a nanoscale octahedron. *Nature*, 427(6975):618–21, 2004.

[7] Paul W. K. Rothemund, Axel Ekani-Nkodo, Nick Papadakis, Ashish Kumar, Deborah Kuchnir Fygenson, and Erik Winfree. Design and characterization of programmable DNA nanotubes. *J. Am. Chem. Soc.*, 126(50):16344–52, 2004.

[8] P. W. K. Rothemund. Folding DNA to create nanoscale shapes and patterns. *Nature*, 440(7082):297–302, 2006.

[9] Martin Langecker, Vera Arnaut, Thomas G. Martin, Jonathan List, Stephan Renner, Michael Mayer, Hendrik Dietz, and Friedrich C. Simmel. Synthetic lipid membrane channels formed by designed DNA nanostructures. *Science*, 338(6109):932–6, November 2012.

[10] Y. Ke, L. L. Ong, W. M. Shih, and P. Yin. Three-dimensional structures self-assembled from DNA bricks. *Science*, 338(6111):1177–1183, November 2012.

[11] Dongran Han, Suchetan Pal, Yang Yang, Shuoxing Jiang, Jeanette Nangreave, Yan Liu, and Hao Yan. DNA gridiron nanostructures based on four-arm junctions. *Science*, 339(6126):1412–1415, 2013.

[12] Jean-Philippe J. Sobczak, Thomas G. Martin, Thomas Gerling, and Hendrik Dietz. Rapid folding of DNA into nanoscale shapes at constant temperature. *Science*, 338(6113):1458–61, December 2012.

[13] Ryosuke Iinuma, Yonggang Ke, Ralf Jungmann, Thomas Schlichthaerle, Johannes B. Woehrstein, and Peng Yin. Polyhedra self-assembled from DNA tripods and characterized with 3D DNA-PAINT. *Science*, 344(6179):65–9, April 2014.

[14] Hendrik Dietz, Shawn M. Douglas, and William M. Shih. Folding DNA into twisted and curved nanoscale shapes. *Science*, 325(5941):725–30, 2009.

[15] Xiao-Chen C. Bai, Thomas G. Martin, Sjors H. W. Scheres, and Hendrik Dietz. Cryo-EM structure of a 3D DNA-origami object. *Proc. Natl. Acad. Sci. U. S. A.*, 109(49):20012–7, December 2012.

[16] Thomas Gerling, Klaus F. Wagenbauer, Andrea M. Neuner, and Hendrik Dietz. Dynamic DNA devices and assemblies formed by shape-complementary, nonbase pairing 3D components. *Science*, 347(6229):1446–1452, 2015.

[17] Shawn M. Douglas, Hendrik Dietz, Tim Liedl, Björn Högberg, Franziska Graf, and William M. Shih. Self-assembly of DNA into nanoscale three-dimensional shapes. *Nature*, 459(7245):414–8, 2009.

[18] Yonggang Ke, Shawn M. Douglas, Minghui Liu, Jaswinder Sharma, Anchi Cheng, Albert Leung, Yan Liu, William M. Shih, and Hao Yan. Multilayer DNA origami packed on a square lattice. *J. Am. Chem. Soc.*, 131(43):15903–8, 2009.

[19] Yonggang Ke, Niels V. Voigt, Kurt V. Gothelf, and William M. Shih. Multilayer DNA origami packed on hexagonal and hybrid lattices. *J. Am. Chem. Soc.*, 134(3):1770–4, 2012.

[20] Yonggang Ke, Luvena L. Ong, Wei Sun, Jie Song, Mingdong Dong, William M. Shih, and Peng Yin. Dna brick crystals with prescribed depths. *Nat. Chem.*, 6(11):994–1002, 2014.

[21] Reza M. Zadegan, Mette D. E. Jepsen, Karen E. Thomsen, Anders H. Okholm, David H. Schaffert, Ebbe S. Andersen, Victoria Birkedal, and Jørgen Kjems. Construction of a 4 zeptoliters switchable 3D DNA box origami. *ACS Nano*, 6(11):10050–10053, 2012.

[22] Do-Nyun Kim, Fabian Kilchherr, Hendrik Dietz, and Mark Bathe. Quantitative prediction of 3D solution shape and flexibility of nucleic acid nanostructures. *Nucleic Acids Res.*, December 2011.

[23] Christopher Maffeo, Thuy T. M. Ngo, Taekjip Ha, and Aleksei Aksimentiev. A coarse-grained model of unstructured single-stranded DNA derived from atomistic simulation and single-molecule experiment. *J. Chem. Theory Comput.*, 10:2891–2896, 2014.

[24] Erik Benson, Abdulmelik Mohammed, Johan Gardell, Sergej Masich, Eugen Czeizler, Pekka Orponen, and Björn Högberg. DNA rendering of polyhedral meshes at the nanoscale. *Nature*, 523(7561):441–444, 2015.

[25] Sean Williams, Kyle Lund, Chenxiang Lin, Peter Wonka, Stuart Lindsay, and Hao Yan. Tiamat: A three-dimensional editing tool for complex DNA structures. In Ashish Goel, Friedrich C. Simmel, and Petr Sosík, editors, *DNA Computing*, volume 5347 of *Lecture Notes in Computer Science*, pages 90–101. Springer Berlin Heidelberg, 2009.

[26] Carlos Ernesto Castro, Fabian Kilchherr, Do-Nyun Kim, Enrique Lin Shiao, Tobias Wauer, Philipp Wortmann, Mark Bathe, and Hendrik Dietz. A primer to scaffolded DNA origami. *Nat. Methods*, 8(3):221–229, March 2011.

[27] K. J. Bathe. *Finite Element Procedures*. Prentice-Hall International Series in. Prentice Hall, 1996.

[28] Steven B. Smith, Yujia Cui, and Carlos Bustamante. Overstretching B-DNA: the elastic response of individual double-stranded and single-stranded DNA molecules. *Science*, 271(5250):795–799, 1996.

[29] Bernard R. Brooks, Dušanka Janežič, and Martin Karplus. Harmonic analysis of large systems. I. Methodology. *J. Comput. Chem.*, 16(12):1522–1542, 1995.

[30] Mark Bathe. A finite element framework for computation of protein normal modes and mechanical response. *Proteins: Struct., Funct., Bioinf.*, 70(4):1595–1609, 2008.

[31] Marissa G. Saunders and Gregory A. Voth. Coarse-graining methods for computational biology. *Annu. Rev. Biophys.*, 42:73–93, January 2013.

[32] Davit A. Potoyan, Alexey Savelyev, and Garegin A. Papoian. Recent successes in coarse-grained modeling of DNA. *WIREs Comput Mol Sci*, 3(1):69–83, January 2013.

[33] Jonathan P. K. Doye, Thomas E. Ouldridge, Ard A. Louis, Flavio Romano, Petr Šulc, Christian Matek, Benedict E. K. Snodin, Lorenzo Rovigatti, John S. Schreck, Ryan M. Harrison, and William P. J. Smith. Coarse-graining DNA for simulations of DNA nanotechnology. *Phys. Chem. Chem. Phys.*, 15(47):20395–20414, December 2013.

[34] Daniel M. Hinckley, Gordon S. Freeman, Jonathan K. Whitmer, and Juan J de Pablo. An experimentally-informed coarse-grained 3-site-per-nucleotide model of DNA: Structure, thermodynamics, and dynamics of hybridization. *J. Chem. Phys.*, 139(14):144903, October 2013.

[35] Petr Šulc, Flavio Romano, Thomas E. Ouldridge, Lorenzo Rovigatti, Jonathan P. K. Doye, and Ard A. Louis. Sequence-dependent thermodynamics of a coarse-grained DNA model. *J. Chem. Phys.*, 137(13):135101, October 2012.

[36] Pablo M. De Biase, Carlos J. F. Solano, Suren Markosyan, Luke Czapla, and Sergei Yu Noskov. BROMOC-D: Brownian dynamics/Monte-Carlo program suite to study ion and DNA permeation in nanopores. *J. Chem. Theory Comput.*, 8(7):2540–2551, July 2012.

[37] Alexey Savelyev and Garegin A. Papoian. Chemically accurate coarse graining of double-stranded DNA. *Proc. Natl. Acad. Sci. U. S. A.*, 107(47):20340–20345, November 2010.

[38] Yi He, Maciej Maciejczyk, Stanisław Ołdziej, Harold A. Scheraga, and Adam Liwo. Mean-field interactions between nucleic-acid-base dipoles can drive the formation of a double helix. *Phys. Rev. Lett.*, 110(9):098101, February 2013.

[39] Chia Wei Hsu, Maria Fyta, Greg Lakatos, Simone Melchionna, and Efthimios Kaxiras. *Ab initio* determination of coarse-grained interactions in double-stranded DNA. *J. Chem. Phys.*, 137(10):105102, September 2012.

[40] Alex Morriss-Andrews, Joerg Rottler, and Steven S. Plotkin. A systematically coarse-grained model for DNA and its predictions for persistence length, stacking, twist, and chirality. *J. Chem. Phys.*, 132(3):035105, January 2010.

[41] Pablo D. Dans, Ari Zeida, Matías R. Machado, and Sergio Pantano. A coarse grained model for atomic-detailed DNA simulations with explicit electrostatics. *J. Chem. Theory Comput.*, 6(5):1711–1725, May 2010.

[42] Maciej Maciejczyk, Aleksandar Spasic, Adam Liwo, and Harold A. Scheraga. Coarse-grained model of nucleic acid bases. *J. Comput. Chem.*, 31(8):1644–1655, June 2010.

[43] Srinivasa M. Gopal, Shayantani Mukherjee, Yi-Ming Cheng, and Michael Feig. PRIMO/PRIMONA: a coarse-grained model for proteins and nucleic acids that preserves near-atomistic accuracy. *Proteins: Struct., Funct., Bioinf.*, 78(5):1266–1281, April 2010.

[44] Robert C. DeMille, Thomas E. Cheatham, and Valeria Molinero. A coarse-grained model of DNA with explicit solvation by water and ions. *J. Phys. Chem. B*, 115(1):132–142, January 2011.

[45] Thomas E. Ouldridge, Ard A. Louis, and Jonathan P. K. Doye. Structural, mechanical, and thermodynamic properties of a coarse-grained DNA model. *J. Chem. Phys.*, 134(8):085101, February 2011.

[46] M. P. Allen and D. J. Tildesley. *Computer Simulation of Liquids*. Oxford University Press, New York, 1987.

[47] L. Verlet. Computer 'experiments' on classical fluids: I. Thermodynamical properties of Lennard-Jones molecules. *Physical Review*, 159:98–103, 1967.

[48] Jejoong Yoo and Aleksei Aksimentiev. Improved parametrization of Li^+, Na^+, K^+, and Mg^{2+} ions for all-atom molecular dynamics simulations of nucleic acid systems. *J. Phys. Chem. Lett.*, 3(1):45–50, 2012.

[49] Jejoong Yoo and Aleksei Aksimentiev. Competitive binding of cations to duplex DNA revealed through molecular dynamics simulations. *J. Phys. Chem. B*, 116(43):12946–12954, 2012.

[50] Jejoong Yoo and Aleksei Aksimentiev. Improved parameterization of amine–carboxylate and amine–phosphate interactions for molecular dynamics simulations using the CHARMM and AMBER force fields. *J. Chem. Theory Comput.*, 12(1):430–443, 2016.

[51] Jejoong Yoo and Aleksei Aksimentiev. The structure and intermolecular forces of DNA condensates. *Nucleic Acids Res.*, 44:2036–2046, 2016.

[52] Jejoong Yoo and Aleksei Aksimentiev. In situ structure and dynamics of DNA origami determined through molecular dynamics simulations. *Proc. Natl. Acad. Sci. U. S. A.*, 110(50):20099–20104, 2013.

[53] Aleksei Aksimentiev. Deciphering ionic current signatures of DNA transport through a nanopore. *Nanoscale*, 2:468–483, 2010.

[54] Aleksij Aksimentiev and Klaus Schulten. Imaging α-hemolysin with molecular dynamics: Ionic conductance, osmotic permeability and the electrostatic potential map. *Biophys. J.*, 88:3745–3761, 2005.

[55] Chen-Yu Li, Elisa A. Hemmig, Jinglin Kong, Jejoong Yoo, Silvia Hernández-Ainsa, Ulrich F. Keyser, and Aleksei Aksimentiev. Ionic conductivity, structural deformation and programmable anistropy of DNA origami in electric field. *ACS Nano*, 9(2):1420–1433, 2015.

[56] James C. Phillips, Rosemary Braun, Wei Wang, James Gumbart, Emad Tajkhorshid, Elizabeth Villa, Christophe Chipot, Robert D. Skeel, Laxmikant Kale, and Klaus Schulten. Scalable molecular dynamics with NAMD. *J. Comput. Chem.*, 26:1781–1802, 2005.

[57] A. D. MacKerell, Jr., D. Bashford, M. Bellott, R. L. Dunbrack, Jr., J. Evanseck, M. J. Field, S. Fischer, J. Gao, H. Guo, S. Ha, D. Joseph, L. Kuchnir, K. Kuczera, F. T. K. Lau, C. Mattos, S. Michnick, T. Ngo, D. T. Nguyen, B. Prodhom, I. W. E. Reiher, B. Roux, M. Schlenkrich, J. Smith, R. Stote, J. Straub, M. Watanabe, J. Wiorkiewicz-Kuczera, D. Yin, and M. Karplus. All-atom empirical potential for molecular modeling and dynamics studies of proteins. *J. Phys. Chem. B*, 102:3586–3616, 1998.

[58] Joseph B. Lim and Jeffery B. Klauda. Lipid chain branching at the iso- and anteiso-positions in complex chlamydia membranes: a molecular dynamics study. *Biochim. Biophys. Acta*, 1808(1):323–31, 1 2011.

[59] Kenno Vanommeslaeghe, Elizabeth Hatcher, Chayan Acharya, Sibsankar Kundu, Shijun Zhong, Jihyun Shim, Eva Darian, Olgun Guvench, Pedro Lopes, Igor Vorobyov, and Alexander D. MacKerell, Jr. CHARMM general force field: A force field for drug-like molecules compatible with the CHARMM all-atom additive biological force fields. *J. Comput. Chem.*, 31(4):671–690, 2010.

[60] Eduardo R. Cruz-Chu, Aleksei Aksimentiev, and Klaus Schulten. Water-silica force field for simulating nanodevices. *J. Phys. Chem. B*, 110:21497–21508, 2006.

[61] Shuichi Miyamoto and Peter A. Kollman. SETTLE: An analytical version of the SHAKE and RATTLE algorithm for rigid water molecules. *J. Comput. Chem.*, 13(8):952–962, 1992.

[62] Hans C. Andersen. RATTLE: A "velocity" version of the SHAKE algorithm for molecular dynamics calculations. *J. Comput. Phys.*, 52(1):24–34, 1983.

[63] Paul F. Batcho, David A. Case, and Tamar Schlick. Optimized particle-mesh Ewald/multiple-time step integration for molecular dynamics simulations. *J. Chem. Phys.*, 115(9):4003–4018, 2001.

[64] R. D. Skeel, David J. Hardy, and James C. Phillips. Correcting mesh-based force calculations to conserve both energy and momentum in molecular dynamics simulations. *J. Comput. Phys.*, 225(1):1–5, 2007.

[65] Scott Michael Slone, Chen-Yu Li, Jejoong Yoo, and Aleksei Aksimentiev. Molecular mechanics of DNA bricks: *in situ* structure, mechanical properties and ionic conductivity. *New J. Phys.*, 18(5):055012, 2016.

[66] Christopher Maffeo, Jejoong Yoo, and Aleksei Aksimentiev. De novo prediction of DNA origami structures through atomistic molecular dynamics simulation. *Nucleic Acids Res.*, 44(7):3013–3019, 2016.

[67] Aleksij Aksimentiev, Jiunn Benjamin Heng, Gregory Timp, and Klaus Schulten. Microscopic kinetics of DNA translocation through synthetic nanopores. *Biophys. J.*, 87:2086–2097, 2004.

[68] J. D. Hunter. Matplotlib: A 2d graphics environment. *Comput. Sci. Eng.*, 9(3):90–95, 2007.

[69] Cees Dekker. Solid-state nanopores. *Nat. Nanotech.*, 2:209–215, 2007.

[70] J. J. Kasianowicz, J. W. F. Robertson, E. R. Chan, J. E. Reiner, and V. M. Stanford. Nanoscopic porous sensors. *Annu. Rev. Anal. Chem.*, 1:737–766, 2008.

[71] S. Howorka and Zuzanna S. Siwy. Nanopore analytics: Sensing of single molecules. *Chem. Soc. Rev.*, 38(8):2360–2384, 2009.

[72] Meni Wanunu. Nanopores: A journey towards DNA sequencing. *Phys. Life Rev.*, 9(2):125–158, 2012.

[73] J. J. Kasianowicz, E. Brandin, D. Branton, and D. W. Deamer. Characterization of individual polynucleotide molecules using a membrane channel. *Proc. Natl. Acad. Sci. U. S. A.*, 93:13770–13773, 1996.

[74] Jiali Li, Derek Stein, Ciaran McMullan, Daniel Branton, Michael J. Aziz, and Jene A. Golovchenko. Ion-beam sculpting at nanometre length scales. *Nature*, 412(6843):166–169, 2001.

[75] W. A. Vercoutere, S. Winters-Hilt, V. S. DeGuzman, D. Deamer, S. E. Ridino, J. T. Rodgers, H. E. Olsen, A. Marziali, and M. Akeson. Discrimination among individual Watson-Crick base pairs at the termini of single DNA hairpin molecules. *Nucleic Acids Res.*, 31:1311–1318, 2003.

[76] James Clarke, Hai-Chen Wu, Lakmal Jayasinghe, Alpesh Patel, Stuart Reid, and Hagan Bayley. Continuous base identification for single-molecule nanopore DNA sequencing. *Nat. Nanotech.*, 4(4):265–270, 2009.

[77] Gary M. Skinner, Michiel van den Hout, Onno Broekmans, Cees Dekker, and Nynke H. Dekker. Distinguishing single- and double-stranded nucleic acid molecules using solid-state nanopores. *Nano Lett.*, 9(8):2953–2960, 2009.

[78] Meni Wanunu, Swati Bhattacharya, Yun Xie, Yitzhak Tor, Aleksei Aksimentiev, and Marija Drndic. Nanopore analysis of individual RNA/antibiotic complexes. *ACS Nano*, 5(12):9345–9353, 2011.

[79] E. A. Manrao, Ian M. Derrington, Mikhail Pavlenok, Michael Niederweis, and Jens H. Gundlach. Nucleotide discrimination with DNA immobilized in the MspA nanopore. *PLoS One*, 6(10):e25723, 2011.

[80] Kimberly Venta, Gabriel Shemer, Matthew Puster, Julio A. Rodriguez-Manzo, Adrian Balan, Jacob K. Rosenstein, Ken Shepard, and Marija Drndic. Differentiation of short, single-stranded DNA homopolymers in solid-state nanopores. *ACS Nano*, 7:4629–4636, 2013.

[81] Ulrich F. Keyser. Controlling molecular transport through nanopores. *J. R. Soc. Interf.*, 8(63):1369–1378, 2011.

[82] Ruoshan Wei, Volker Gatterdam, Ralph Wieneke, Robert Tampe, and Ulrich Rant. Stochastic sensing of proteins with receptor-modified solid-state nanopores. *Nat. Nanotech.*, 7:257–263, 2012.

[83] E. C. Yusko, P. Prangkio, D. Sept, R. C. Rollings, J. Li, and M. Mayer. Single particle characterization of aβ oligomers in solution. *ACS Nano*, 6:5909–5919, 2012.

[84] J. M. Scholtz L. Movileanu, J.P. Schmittschmitt and H. Bayley. Interactions of peptides with a protein pore. *Biophys. J.*, 89:1030–1045, 2005.

[85] Meni Wanunu and Amit Meller. Chemically modified solid-state nanopores. *Nano Lett.*, 7(6):1580–1585, 2007.

[86] Xu Hou, Wei Guo, and Lei Jiang. Biomimetic smart nanopores and nanochannels. *Chem. Soc. Rev.*, 40:2385–2401, 2011.

[87] A. R. Hall, A. Scott, D. Rotem, K. K. Mehta, H. Bayley, and Cees Dekker. Hybrid pore formation by directed insertion of α-haemolysin into solid-state nanopores. *Nat. Nanotech.*, 5(12):874–877, 2010.

[88] E. C. Yusko, J. M. Johnson, S. Majd, P. Prangkio, R. C. Rollings, J. Li, J. Yang, and M. Mayer. Controlling protein translocation through nanopores with bio-inspired fluid walls. *Nat. Nanotech.*, 6:253–260, 2011.

[89] Bala M. Venkatesan, James Polans, Jeffrey Comer, Supriya Sridhar, David Wendell, Aleksei Aksimentiev, and Rashid Bashir. Lipid bilayer coated Al_2O_3 nanopore sensors: Towards a hybrid biological solid-state nanopore. *Biomed Microdevices*, 13(4):671–682, 2011.

[90] Silvia Hernández-Ainsa, Christoph Muus, Nicholas A. W. Bell, Lorenz J. Steinbock, Vivek V. Thacker, and Ulrich F. Keyser. Lipid-coated nanocapillaries for DNA sensing. *Analyst*, 138:104–106, 2013.

[91] Andre V. Pinheiro, Dongran Han, William M. Shih, and Hao Yan. Challenges and opportunities for structural DNA nanotechnology. *Nat. Nanotech.*, 6(12):763–72, December 2011.

[92] Thomas Tørring, Niels V. Voigt, Jeanette Nangreave, Hao Yan, and Kurt V. Gothelf. DNA origami: a quantum leap for self-assembly of complex structures. *Chem. Soc. Rev.*, 40:5636–5646, 2011.

[93] Ebbe S. Andersen, Mingdong Dong, Morten M. Nielsen, Kasper Jahn, Ramesh Subramani, Wael Mamdouh, Monika M. Golas, Bjoern Sander, Holger Stark, Cristiano L. P. Oliveira, Jan Skov Pedersen, Victoria Birkedal, Flemming Besenbacher, Kurt V. Gothelf, and Jorgen Kjems. Self-assembly of a nanoscale DNA box with a controllable lid. *Nature*, 459(7243):73–6, 2009.

[94] Niels V. Voigt, Thomas Tørring, Alexandru Rotaru, Mikkel F. Jacobsen, Jens B. Ravnsbæk, Ramesh Subramani, Wael Mamdouh, Jørgen Kjems, Andriy Mokhir, Flemming Besenbacher, and Kurt Vesterager Gothelf. Single-molecule chemical reactions on DNA origami. *Nat. Nanotech.*, 5(3):200–203, 2010.

[95] G. P. Acuna, F. M. Möller, P. Holzmeister, S. Beater, B. Lalkens, and P. Tinnefeld. Fluorescence enhancement at docking sites of DNA-directed self-assembled nanoantennas. *Science*, 338(6106):506–10, October 2012.

[96] Jinglin Fu, Minghui Liu, Yan Liu, Neal W. Woodbury, and Hao Yan. Interenzyme substrate diffusion for an enzyme cascade organized on spatially addressable DNA nanostructures. *J. Am. Chem. Soc.*, 134(12):5516–5519, 2012.

[97] Anton Kuzyk, Robert Schreiber, Zhiyuan Fan, Günther Pardatscher, Eva-Maria M. Roller, Alexander Högele, Friedrich C. Simmel, Alexander O. Govorov, and Tim Liedl. DNA-based self-assembly of chiral plasmonic nanostructures with tailored optical response. *Nature*, 483(7389):311–4, March 2012.

[98] Maria Tintoré, Isaac Gállego, Brendan Manning, Ramon Eritja, and Carme Fàbrega. DNA origami as a DNA repair nanosensor at the single-molecule level. *Angew. Chem. Int. Ed.*, 52(30):7747–7750, 2013.

[99] Masayuki Endo and Hiroshi Sugiyama. Single-molecule imaging of dynamic motions of biomolecules in DNA origami nanostructures using high-speed atomic force microscopy. *Acc. Chem. Res.*, 47(6):1645–1653, 2014.

[100] Zhen-Gang Wang and Baoquan Ding. Engineering DNA self-assemblies as templates for functional nanostructures. *Acc. Chem. Res.*, 47(6):1654–1662, 2014.

[101] Roman Tsukanov, Toma E. Tomov, Miran Liber, Yaron Berger, and Eyal Nir. Developing DNA nanotechnology using single-molecule fluorescence. *Acc. Chem. Res.*, 47(6):1789–1798, 2014.

[102] Vivek V. Thacker, Lars O. Herrmann, Daniel O. Sigle, Tao Zhang, Tim Liedl, Jeremy J. Baumberg, and Ulrich F. Keyser. DNA origami based assembly of gold nanoparticle dimers for surface-enhanced Raman scattering. *Nat. Commun.*, 5, March 2014.

[103] Silvia Hernández-Ainsa and Ulrich F. Keyser. DNA origami nanopores: an emerging tool in biomedicine. *Nanomedicine (London, U. K.)*, 8(10):1551–1554, September 2013.

[104] Nicholas A. W. Bell and Ulrich F. Keyser. Nanopores formed by DNA origami: A review. *FEBS Lett.*, 588(19):3564–3570, September 2014.

[105] Silvia Hernández-Ainsa and Ulrich F. Keyser. DNA origami nanopores: Developments, challenges and perspectives. *Nanoscale*, 2014.

[106] Nicholas A. W. Bell, Christian. R. Engst, Marc Ablay, Giorgio Divitini, Caterina Ducati, Tim Liedl, and Ulrich F. Keyser. DNA origami nanopores. *Nano Lett.*, 12(1):512–517, 2012.

[107] Ruoshan Wei, Thomas G. Martin, Ulrich Rant, and Hendrik Dietz. DNA origami gatekeepers for solid-state nanopores. *Angew. Chem. Int. Ed.*, 51(20):4864–7, May 2012.

[108] Silvia Hernández-Ainsa, Nicholas A. W. Bell, Vivek V. Thacker, Kerstin Göpfrich, Karolis Misiunas, Maria Eugenia Fuentes-Perez, Fernando Moreno-Herrero, and Ulrich F. Keyser. DNA origami nanopores for controlling DNA translocation. *ACS Nano*, 7(7):6024–6030, 2013.

[109] Jonathan R. Burns, Eugen Stulz, and Stefan Howorka. Self-assembled DNA nanopores that span lipid bilayers. *Nano Lett.*, 13(6):2351–2356, 2013.

[110] Jonathan R. Burns, Kerstin Göpfrich, James W. Wood, Vivek V. Thacker, Eugen Stulz, Ulrich F. Keyser, and Stefan Howorka. Lipid-bilayer-spanning DNA nanopores with a bifunctional porphyrin anchor. *Angew. Chem. Int. Ed.*, 52(46):12069–12072, 2013.

[111] Nicholas A. W. Bell, Vivek V. Thacker, Silvia Hernández-Ainsa, Maria E. Fuentes-Perez, Fernando Moreno-Herrero, Tim Liedl, and Ulrich F. Keyser. Multiplexed ionic current sensing with glass nanopores. *Lab Chip*, 13:1859–1862, 2013.

[112] Silvia Hernández-Ainsa, Karolis Misiunas, Vivek V. Thacker, Elisa A. Hemmig, and Ulrich F. Keyser. Voltage-dependent properties of DNA origami nanopores. *Nano Lett.*, 14(3):1270–1274, 2014.

[113] Calin Plesa, Adithya N. Ananth, Veikko Linko, Coen Gülcher, Allard J. Katan, Hendrik Dietz, and Cees Dekker. Ionic permeability and mechanical properties of DNA origami nanoplates on solid-state nanopores. *ACS Nano*, 8(1):35–43, 2014.

[114] Shawn M. Douglas, Adam H. Marblestone, Surat Teerapittayanon, Alejandro Vazquez, George M. Church, and William M. Shih. Rapid prototyping of 3D DNA-origami shapes with caDNAno. *Nucleic Acids Res.*, 37(15):5001–6, August 2009.

[115] Weifeng Li, Lars Nordenskiöld, Ruhong Zhou, and Yuguang Mu. Conformation-dependent DNA attraction. *Nanoscale*, 6:7085–7092, 2014.

[116] Binquan Luan and Aleksei Aksimentiev. Electro-osmotic screening of the DNA charge in a nanopore. *Phys. Rev. E*, 78:021912, 2008.

[117] Glenn J. Martyna, Douglas J. Tobias, and Michael L. Klein. Constant pressure molecular dynamics algorithms. *J. Chem. Phys.*, 101(5):4177–4189, 1994.

[118] S. E. Feller, Y. H. Zhang, R. W. Pastor, and B. R. Brooks. Constant pressure molecular dynamics simulation — the Langevin piston method. *J. Chem. Phys.*, 103(11):4613–4621, 1995.

[119] Axel T. Brünger. *X-PLOR, Version 3.1: A System for X-ray Crystallography and NMR*. The Howard Hughes Medical Institute and Department of Molecular Biophysics and Biochemistry, Yale University, 1992.

[120] David B. Wells, Volha Abramkina, and Aleksei Aksimentiev. Exploring transmembrane transport through α-hemolysin with grid-steered molecular dynamics. *J. Chem. Phys.*, 127:125101, 2007.

[121] Maxim Belkin, Christopher Maffeo, David B. Wells, and Aleksei Aksimentiev. Stretching and controlled motion of single-stranded DNA in locally heated solid-state nanopores. *ACS Nano*, 7(8):6816–6824, 2013.

[122] Kerstin Göpfrich, Chen-Yu Li, Iwona Mames, Satya Prathyusha Bhamidimarri, Maria Ricci, Jejoong Yoo, Adam Mames, Alexander Ohmann, Mathias Winterhalter, Eugen Stulz, Aleksei Aksimentiev, and Ulrich F Keyser. Ion channels made from a single membrane-spanning DNA duplex. *Nano Lett.*, 16(7):4665–4669, 2016.

[123] Kerstin Göpfrich, Chen-Yu Li, Maria Ricci, Satya Prathyusha Bhamidimarri, Jejoong Yoo, Bertalan Gyenes, Alexander Ohmann, Mathias Winterhalter, Aleksei Aksimentiev, and Ulrich F Keyser. Large-conductance transmembrane porin made from DNA origami. *ACS Nano*, 10(9):8207–8214, 2016.

[124] Astrid Seifert, Kerstin Göpfrich, Jonathan R. Burns, Niels Fertig, Ulrich F. Keyser, and Stefan Howorka. Bilayer-spanning DNA nanopores with voltage-switching between open and closed state. *ACS Nano*, 9(2):1117–26, 2 2015.

[125] Kerstin Göpfrich, Thomas Zettl, Anna E. C. Meijering, Silvia Hernández-Ainsa, Samet Kocabey, Tim Liedl, and Ulrich F. Keyser. DNA-tile structures induce ionic currents through lipid membranes. *Nano Lett.*, 15(5):3134–3138, 2015.

[126] Jonathan R. Burns, Astrid Seifert, Niels Fertig, and Stefan Howorka. A biomimetic DNA-based channel for the ligand-controlled transport of charged molecular cargo across a biological membrane. *Nat. Nanotech.*, 11:152–156, 2016.

[127] Swati Krishnan, Daniela Ziegler, Vera Arnaut, Thomas G. Martin, Korbinian Kapsner, Katharina Henneberg, Andreas R. Bausch, Hendrik Dietz, and Friedrich C. Simmel. Molecular transport through large-diameter DNA nanopores. *Nat. Commun.*, 7(12787), 2016.

[128] Dongran Han, Suchetan Pal, Jeanette Nangreave, Zhengtao Deng, Yan Liu, and Hao Yan. DNA origami with complex curvatures in three-dimensional space. *Science*, 332(6027):342–6, 2011.

[129] Jejoong Yoo and Aleksei Aksimentiev. Molecular dynamics of membrane-spanning DNA channels: Conductance mechanism, electro-osmotic transport and mechanical gating. *J. Phys. Chem. Lett.*, 6:4680–4687, 11 2015.

[130] Vishal Maingi, Mickaël Lelimousin, Stefan Howorka, and Mark S. P. Sansom. Gating-like motions and wall porosity in a dna nanopore scaffold revealed by molecular simulations. *ACS Nano*, 9(11):11209–11217, 2015.

[131] Olaf S. Andersen and Roger E. Koeppe. Bilayer thickness and membrane protein function: An energetic perspective. *Annu. Rev. Biophys. Biomol. Struct.*, 36(1):107–130, 2007.

[132] David Stoddart, Mariam Ayub, Lajos Höfler, Pinky Raychaudhuri, Jochen W. Klingelhoefer, Giovanni Maglia, Andrew Heron, , and Hagan Bayley. Functional truncated membrane pores. *Proc. Natl. Acad. Sci. U. S. A.*, 111(7):2425–2430, 2014.

[133] Steve J. Ludtke, Ke He, William T. Heller, Thad A. Harroun, Lin Yang, and Huey W. Huang. Membrane pores induced by magainin. *Biochemistry*, 35(43):13723–13728, 1996.

[134] Katsumi Matsuzaki, Osamu Murase, Nobutaka Fujii, and Koichiro Miyajima. An antimicrobial peptide, magainin 2, induced rapid flip-flop of phospholipids coupled with pore formation and peptide translocation. *Biochemistry*, 35(35):11361–11368, 1996.

[135] Angelo Demuro, Martin Smith, and Ian Parker. Single-channel ca^{2+} imaging implicates aβ1–42 amyloid pores in alzheimer's disease pathology. *J. Cell Biol.*, 195(3):515–524, 2011.

[136] Henry D. Herce and Angel E. Garcia. Molecular dynamics simulations suggest a mechanism for translocation of the hiv-1 tat peptide across lipid membranes. *Proc. Natl. Acad. Sci. U. S. A.*, 104(52):20805–20810, 2007.

[137] Lars D. Mosgaard and Thomas Heimburg. Lipid ion channels and the role of proteins. *Acc. Chem. Res.*, 46(12):2966–2976, 2013.

[138] W. F. Drew Bennett, Nicolas Sapay, and D. Peter Tieleman. Atomistic simulations of pore formation and closure in lipid bilayers. *Biophys. J.*, 106(1):210–219, 2014.

[139] Mark S. Bretscher. Asymmetrical lipid bilayer structure for biological membranes. *Nat. New Biol.*, 236(61):11–12, 1972.

[140] Santosh Kumar Sahu, Sathyanarayana N. Gummadi, N. Manoj, and Gopala Krishna Aradhyam. Phospholipid scramblases: An overview. *Arch. Biochem. Biophys.*, 462(1):103–114, 2007.

[141] Philippe F. Devaux, Andreas Herrmann, Nina Ohlwein, and Michael M. Kozlov. How lipid flippases can modulate membrane structure. *Biochim. Biophys. Acta*, 1778(7–8):1591–1600, 2008.

[142] Edouard M. Bevers and Patrick L. Williamson. Phospholipid scramblase: An update. *FEBS Lett.*, 584(13):2724–2730, 2010.

[143] John S. Allhusen and John C. Conboy. The ins and outs of lipid flip-flop. *Acc. Chem. Res.*, 50(1):58–65, 2017.

[144] Alessandra Castegna, Christopher M. Lauderback, Hafiz Mohmmad-Abdul, and D.Allan Butterfield. Modulation of phospholipid asymmetry in synaptosomal membranes by the lipid peroxidation products, 4-hydroxynonenal and acrolein: Implications for alzheimer's disease. *Brain Res.*, 1004(1–2):193–197, 2004.

[145] Hafiz Mohmmad Abdul and D. Allan Butterfield. Protection against amyloid beta-peptide (1–42)-induced loss of phospholipid asymmetry in synaptosomal membranes by tricyclodecan-9-xanthogenate (d609) and ferulic acid ethyl ester: Implications for alzheimer's disease. *Biochim. Biophys. Acta*, 1741(1–2):140–148, 2005.

[146] Alain Zachowski. Phospholipids in animal eukaryotic membranes: Transverse asymmetry and movement. *Biochem. J.*, 294(1):1–14, 1993.

[147] Edouard M. Severs, Paul Comfurius, Dave W.C. Dekkers, Marjan Harmsma, and Robert F.A. Zwaal. Transmembrane phospholipid distribution in blood cells: Control mechanisms and pathophysiological significance. *Biol. Chem.*, 379(8–9):973–986, 1998.

[148] Thomas Pomorski, Joost C. M. Holthuis, Andreas Herrmann, and Gerrit van Meer. Tracking down lipid flippases and their biological functions. *J. Cell Sci.*, 117(6):805–813, 2004.

[149] Jonathan C. McIntyre and Richard G. Sleight. Fluorescence assay for phospholipid membrane asymmetry. *Biochemistry*, 30(51):11819–11827, 1991.

[150] Thomas Pomorski, Andreas Herrmann, Alain Zachowski, Philippe F. Devaux, and Peter Müllery. Rapid determination of the transbilayer distribution of nbd-phospholipids in erythrocyte membranes with dithionite. *Mol. Membr. Biol.*, 11(1):39–44, 1994.

[151] Hermann J. Gruber and Hansgeorg Schindler. External surface and lamellarity of lipid vesicles: A practice-oriented set of assay methods. *Biochim. Biophys. Acta Biomembr.*, 1189(2):212–224, 1994.

[152] Curtis Balch, Randal Morris, Elwood Brooks, and Richard G. Sleight. The use of n-(7-nitrobenz-2-oxa-1,3-diazole-4-yl)-labeled lipids in determining transmembrane lipid distribution. *Chem. Phys. Lipids*, 70(2):205–212, 1994.

[153] Patrick Williamson, Edouard M. Bevers, Edgar F. Smeets, Paul Comfurius, Robert A. Schlegel, and Robert F. A. Zwaal. Continuous analysis of the mechanism of activated transbilayer lipid movement in platelets. *Biochemistry*, 34(33):10448–10455, 1995.

[154] Robert F.A Zwaal, Paul Comfurius, and Edouard M Bevers. Scott syndrome, a bleeding disorder caused by defective scrambling of membrane phospholipids. *Biochim. Biophys. Acta*, 1636(2–3):119–128, 2004.

[155] Kodi S. Ravichandran and Ulrike Lorenz. Engulfment of apoptotic cells: signals for a good meal. *Nat. Rev. Immunol.*, 7(12):964–974, 2007.

[156] Haiguang Liu and Yong Duan. Effects of posttranslational modifications on the structure and dynamics of histone H3 n-terminal peptide. *Biophys. J.*, 94(12):4579–85, 6 2008.

[157] Hiroyuki Nakao, Keisuke Ikeda, Yasushi Ishihama, and Minoru Nakano. Membrane-spanning sequences in endoplasmic reticulum proteins promote phospholipid flip-flop. *Biophys. J.*, 110(12):2689–2697, 2016.

[158] Mattia Malvezzi, Madhavan Chalat, Radmila Janjusevic, Alessandra Picollo, Hiroyuki Terashima, Anant K. Menon, and Alessio Accardi. Ca^{2+}-dependent phospholipid scrambling by a reconstituted TMEM16 ion channel. *Nat. Commun.*, 4(2367), 2013.

[159] Jonathan R. Burns, Noura Al-Juffali, Sam M. Janes, and Stefan Howorka. Membrane-spanning DNA nanopores with cytotoxic effect. *Angew. Chem. Int. Ed.*, 53(46):12466–12470, 2014.

[160] Rogan Carr, Jeffrey Comer, Mark D. Ginsberg, and Aleksei Aksimentiev. Atoms-to-microns model for small solute transport through sticky nanochannels. *Lab Chip*, 11(22):3766–3773, 2011.

[161] Rogan Carr, Jeffrey Comer, Mark D. Ginsberg, and Aleksei Aksimentiev. Microscopic perspective on the adsorption isotherm of a heterogeneous surface. *J. Phys. Chem. Lett.*, 2:1804–1807, 2011.

[162] David B. Wells, Maxim Belkin, Jeffrey Comer, and Aleksei Aksimentiev. Assessing graphene nanopores for sequencing DNA. *Nano Lett.*, 12(8):4117–4123, 2012.

[163] Jeffrey Comer and Aleksei Aksimentiev. Predicting the DNA sequence dependence of nanopore ion current using atomic-resolution Brownian dynamics. *J. Phys. Chem. C*, 116(5):3376–3393, 2012.

[164] Winston Timp, Jeffrey Comer, and Aleksei Aksimentiev. DNA base-calling from a nanopore using a Viterbi algorithm. *Biophys. J.*, 102:L37–L39, 2012.

[165] Jeffrey Comer and Aleksei Aksimentiev. DNA sequence-dependent ionic currents in ultra-small solid-state nanopores. *Nanoscale*, 8:9600–9613, 2016.

[166] Christopher Maffeo. *Quantitative all-atom and coarse-grained molecular dynamics simulation studies of DNA*. Ph. D. thesis, University of Illinois, Urbana, 2014.

[167] S. Yu. Noskov, W. Im, and B. Roux. Ion permeation through the α-hemolysin channel: Theoretical studies based on Brownian Dynamics and Poisson-Nernst-Plank electrodiffusion theory. *Biophys. J.*, 87:2299–2309, 2004.

[168] Pablo M. De Biase, Suren Markosyan, and Sergei Noskov. BROMOC suite: Monte Carlo/Brownian Dynamics suite for studies of ion permeation and DNA transport in biological and artificial pores with effective potentials. *J. Comput. Chem.*, 36:264–271, 2015.

[169] Shirley W. I. Siu, Robert Vácha, Pavel Jungwirth, and Rainer A. Böckmann. Biomolecular simulations of membranes: Physical properties from different force fields. *J. Chem. Phys.*, 128(12):125103, 2008.

[170] Rainer A. Böckmann, Agnieszka Hac, Thomas Heimburg, and Helmut Grubmüller. Effect of sodium chloride on a lipid bilayer. *Biophys. J.*, 85(3):1647–1655, 2003.